INSTITUTE OF SPACE AND ASTRONAUTICAL SCIENCE
YOSHINODAI, CHUO, SAGAMIHARA, KANAGAWA 252-5210

ISAS RESEARCH NOTE

ISAS RN 865

Hard X-ray Investigations of Particle Acceleration in Solar Flares

Shi-nosuke Ishikawa[1, 2]

January 2012

1 : University of Tokyo
2 : ISAS/JAXA

Hard X-ray Investigations of Particle Acceleration in Solar Flares

Shin-nosuke Ishikawa

Reproduced from the thesis submitted to
the University of Tokyo for
the Degree of Doctor of Science (Physics)
December 17, 2010

Abstract

The detailed properties of the energy release processes in solar flares, as well as the mechanisms that accelerates particles, are currently not well understood. Accelerated electrons emit hard X-rays (HXRs) by the bremsstrahlung process, therefore HXR observations provide important information about the energy release process in solar flares. Past solar HXR observations such as *Yohkoh*/Hard X-ray Telescope revealed the spatial structure of particle acceleration in solar flares, including two HXR sources at the footpoint of the flare loop and a coronal source above the loop top. In 2002, the *RHESSI* satellite, providing imaging spectroscopy from 3 keV up to ∼10 MeV, started to observe solar flares. Simultaneous wide-range HXR imaging and spectroscopy of solar flares can be done for the first time by *RHESSI*.

We did a statistical survey of imaging of HXR bremsstrahlung sources above 150 keV from electrons accelerated to relativistic energies. Images in the energy range from 150 keV to 450 keV integrated over the total duration of the impulsive phase of the flare are derived. The statistics are good enough for 21 events out of the 26 *RHESSI* γ-ray flares, and we successfully obtained images. The flux ratio of the footpoint sources is found to be similar at 50 keV and above 150 keV, indicating that relativistic electrons are present in both footpoints of the flare loop.

We searched for the best example of a coronal above-the-loop-top source in the *RHESSI* database, and investigated the spectral and spatial structure of the above-the-loop-top source relative to the footpoint source. The best event found shows a coronal source in the 35-100 keV range that is significantly above the thermal flare loop top, similar as seen in the Masuda flare. The chromospheric emissions for this

limb flare shows a single footpoint, with the second footpoint occulted. The large intensity of the above-the-loop-top source and the absence of thermal emission in the above-the-loop-top region suggests that the electrons within above-the-loop-top source are purely non-thermal. Photon indices of the above-the-loop-top and the footpoint sources are 5.3±0.3 and 3.6±0.4, respectively. These difference of indices 1.5 ± 0.5 suggests that these emission are from the same components of electrons through thin- and thick-target bremsstrahlung. Assuming that all the electrons are accelerated at the above-the-loop-top region, the instantaneous number of electrons above 30 keV is $N_{inst} \sim 7 \times 10^{35}$. An electron loss rate by collision above 30 keV at the footpoint is calculated to be $\mathcal{N}_f \sim 2 \times 10^{34}$ electrons/s. If the energy deposition rate is assumed to be similar in the occulted footpoint, the time τ to empty out the above-the-loop-top source by precipitation to the footpoints is ∼17 s. This is similar to the decay time scale of the above-the-loop-top sources of ∼20 s derived from the light curve. Our observations are therefore consistent with the model in which all electrons are accelerated in the above-the-loop-top region and the accelerated electrons precipitate into the footpoints.

To improve the dynamic range for future observations, grazing-incidence HXR focusing optics are a promising new technology for future solar observations. A new sounding rocket mission, the Focusing Optics X-ray Solar Imager (*FOXSI*, to be launched in March, 2012), will test out grazing-incidence HXR focusing optics combined with position-sensitive focal plane detectors for solar observations. In the target energy range of 5-15 keV, the angular resolution of optics is expected to be ∼12 arcseconds with the focal length of 2 m. *FOXSI* will achieve superior sensitivity; two orders of magnitude better than that of the *RHESSI* satellite. For *FOXSI*, we have designed and fabricated a Double-sided Silicon Strip Detector with a pitch of 75 μm, which corresponds to 8 arcsec at the focal length of 2 m. The detector was successfully operated in the laboratory and an energy resolution of 430 eV at a 14 keV line was achieved. We also successfully demonstrated fine-pitch imaging successfully by obtaining a shadow image, hence the implementation of scientific requirements was confirmed. To improve the detector efficiency for the second launch of *FOXSI* (*FOXSI* 2), we developed prototype cadmium telluride detectors with the double-

sided strip configuration with a strip pitch of 400 μm. The detector was successfully operated, and the concept was successfully demonstrated.

Contents

List of Figures

List of Tables

Chapter 1

Introduction

The Sun affects the life and culture of human beings. The Sun was worshiped as an important god in many myths all over the world, including Apollo in Twelve Olympians, Ra in ancient Egyptian religion, and Amaterasu in Japanese mythology. This indicates that human beings of an early date intuitively recognized that our lives strongly depend on the presence of the Sun. Even today, although it is the 21st century, the century of science and technology, we still cannot live without the benefits from the Sun.

In addition, the Sun is one of the most notable astrophysical objects to research. Most of the high-energy particles in the solar system are accelerated in the Sun, and these particles affect space and terrestrial environments. In particular, the relationship of the solar corona to accelerated particles is of interest. The "coronal heating problem" is the question of why the solar corona has such a high temperature of $\sim$MK in comparison to the temperature of the surface of the Sun of $\sim$6000 K (Withbroe & Noyes 1977). This problem is still unsolved. Studies of solar particle accelerations provide insight into the coronal heating problem.

Most of the high-energy particles are accelerated in solar flares. Although it is well accepted that solar flares are caused by release of magnetic energy in the corona, the acceleration mechanism is not yet known in detail. Magnetic reconnection (details in Section 2.3) could be the central mechanism to release energy in flares. However, further observations are required to establish a complete picture of solar flares and

particle acceleration.

Release of energy stored in magnetic fields by magnetic reconnection might be the mechanism of various explosive phenomena in the universe. Examples are as follows: A stellar superflare of the RS Canum Venaticorum binary (a binary with late-type stars) II Pegasi, which emitted a hard X-ray flux of 10^5 times larger than the largest solar flare ever observed in the peak duration, was observed by the *Swift* Satellite (Osten et al. 2007). An X-ray flare from a protostar in the R Coronae Australis molecular cloud was observed by the *ASCA* satellite (Koyama et al. 1996). Fast flares from possible magnetar SWIFT J195509.6+261406 were observed by multi-wavelength observations (Stefanescu et al. 2008).

Also particle acceleration is a global astrophysical phenomena, with or without magnetic reconnection, and accelerations in solar flares are possibly related to high-energy phenomena in other astrophysical objects. Possible acceleration sites in the universe includes supernova remnants, pulsars, jets from active galactic nuclei, clusters of galaxies, and the termination shock in the solar system. Cosmic ray particles are accelerated to very high energies up to >EeV; the source is unknown.

The most important reason to study particle accelerations in the Sun among various astrophysical objects is the close distance from us. Compared to other objects, intense fluxes can be detected from the Sun, and it is possible to observe intrinsically fainter events. In addition, the Sun is the only object producing particle acceleration in which it is possible to provide fine spatially resolved observations. These enable us to obtain significantly detailed data of high-energy activities, and a detailed picture of acceleration is revealed only by the Sun. The results from research on particle acceleration in the Sun provides important information on physical processes of accelerations in other astrophysical objects.

In the last couple of decades, the understanding of solar flares progressed significantly due to hard X-ray (HXR) observations using satellites. The hard X-ray telescope (HXT) onboard the *Yohkoh* satellite (operated in 1991-2001) was a successful Japanese HXR imager. One of the major results was the detection of the HXR source from above the flare loop top, which is often referred to as "the Masuda flare" (Masuda et al. 1994). In 2002, the Reuven Ramaty High-energy Solar Spec-

troscopic Imager (*RHESSI*) satellite (with imaging spectroscopy from 3 keV up to ∼10 MeV) started to observe solar flares (details in Chapter 3). A review of previous observations is also described in Chapter 2.

In this thesis, we study particle accelerations in solar flares through HXR observations by *RHESSI* with two topics; a statistical imaging study of HXR bremsstrahlung sources above 150 keV from relativistically accelerated electrons (Chapter 4), and the best example of a coronal above-the-loop-top source in the *RHESSI* database, which is similar to the Masuda flare (Chapter 5 and 6). Descriptions of future missions for further observations (Chapter 7), and development of fine-pitch semiconductor detectors for these missions (Chapter 8) are discussed.

Chapter 2

Solar Flares

2.1 Overview of Solar Flares

2.1.1 Basic Properties of Solar Flares

A solar flare is an explosive release of energy in the Sun's atmosphere that emits strong radiation and particles (review by Benz 2008). The upper atmosphere in which flares occur is called the corona. The corona has a high temperature of ∼MK, in contrast to the solar surface of the photosphere with a temperature of ∼6000 K. Solar flares were first discovered by Carrington and Hodgson as brightenings in white light (Carrington 1859; Hodgson 1859). Flares normally occur near sunspots, and the regions with many flaring activities are referred to as active regions of the Sun. Sunspots are known to have strong magnetic fields (∼1000 G), and the energy source of solar flares is magnetic energy. However, the process of converting magnetic energies to kinetic energies is still not well understood (see Section 2.3).

The origin of strong magnetic fields of the Sun is thought to be the process of amplifying magnetic fields through gas motions, called the dynamo mechanism. Numbers of sunspots and activities in the solar atmosphere have an ∼11 year periodicity, referred to as the solar cycle.

During solar flares, multiwavelength radiation is emitted from radio to γ-ray, and the duration varies from a few minutes up to hours. Typical time profiles of

multiwavelength emissions during solar flares are shown in Fig. 2.1. As shown in Fig. 2.1, solar flares have two phases; the impulsive phase with fast rising radio and HXR emissions, and the gradual phase with slower rise and decay of Hα and soft X-ray (SXR) emissions. Figure 2.2 is an example of a multiwavelength spectrum of a typical flare that occurred in December 6, 2006. While SXRs are emitted by thermal plasmas through the bremsstrahlung process, HXRs are originated by accelerated particles (see Section 2.2 for details).

Solar flares release enormous energies from 10^{28}-10^{32} erg, which could be one of the most energetic explosive phenomena in the present-day solar system. High temperature plasmas such as $\sim$10-50 MK (10-50 times higher than the ordinary corona), and accelerated high-energy particles from $\sim$10 keV up to $\sim$ GeV which deviate from Maxwellian distributions accompany solar flares ("non-thermal" distributions). Some flares are accompanied by large scale plasma motions, such as coronal mass ejections (CMEs).

2.1.2 Flare Statistics and Scalings

Basically, sizes of flares are classified by 1-8 Å SXR peak fluxes measured by the solar monitoring satellite *GOES*. The *GOES* class is described by the combination of a prefix alphabet with one or two significant figures of a flux. The prefixes are X, M, C, B, or A, indicating the order of magnitude of a *GOES* flux. For example, an X-class flare has a flux of 10^{-4} W/m^2, and preceding classes have a flux one order of magnitude smaller than that of previous one.

Total energies of solar flares are distributed over more than ten orders of magnitude, and flares are also classified by their total released energies. "Regular" or "large flares" have total energies of $E \sim 10^{30}$-10^{33} erg, with plasma temperatures of $T \sim$8-40 K (Aschwanden 2005). Smaller flares with $E \sim 10^{27}$-10^{30} erg and $T \sim$2-8 K are called microflares. Flares smaller than microflares, referred to as "nanoflares" with $E \sim 10^{27}$-10^{30} erg and $T \sim$2-8 K are also observed in extreme ultraviolet (EUV). Although large flares and microflares are observed in active regions, nanoflares are only observed outside of active regions so far (nanoflares are also described in Chapter 7).

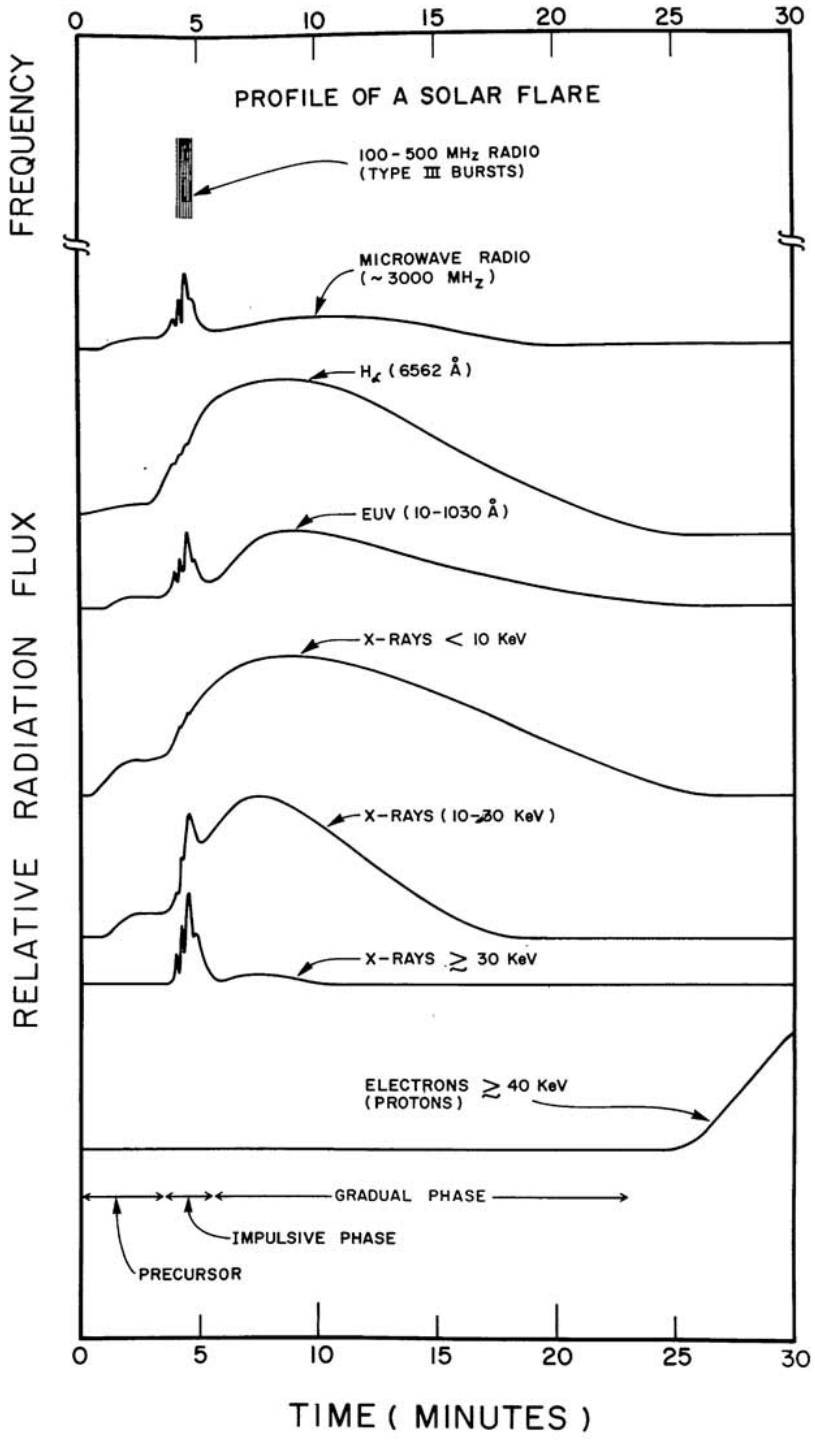

Figure 2.1 Schematic time profiles of multiwavelength radiations emitted during typical solar flares (Kane 1974).

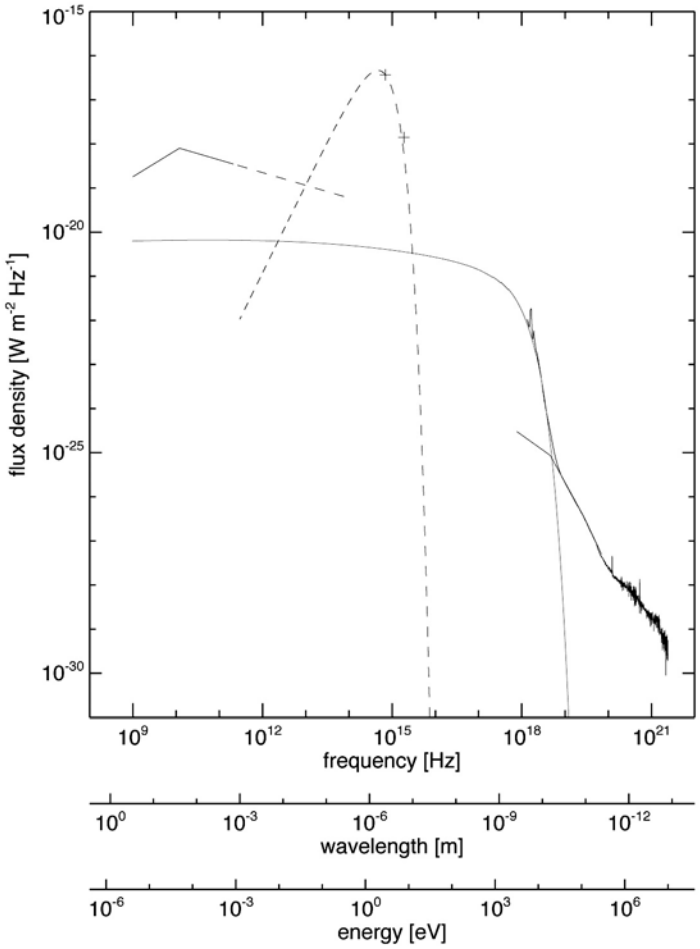

Figure 2.2 Multiwavelength spectrum of the December 6, 2006 flare. Instruments are as follows: Microwave: The Nobeyama radioheliograph (Nakajima et al. 1994). White light: *Hinode* (Kosugi et al. 2007). Ultraviolet: *TRACE* (Handy et al. 1999). X-ray and γ-ray: *RHESSI*. The spectrum is fit by gyrosynchrotron (microwaves, solid line), black body (optical, dashed curve), thermal and non-thermal bremsstrahlung (UV up to γ-rays, red and blue curve) models.

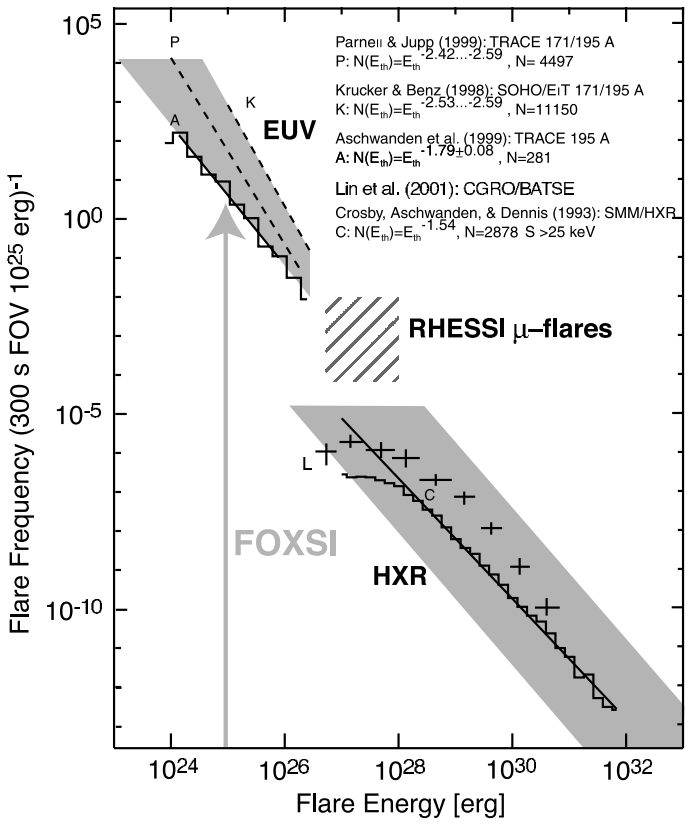

Figure 2.3 Frequency distribution of solar flares.

The occurrence frequency of flares depend on their energy contents. The frequency distribution follows this formula:

$$\frac{dN}{dE} \propto E^{-\alpha}, \tag{2.1}$$

where the constant α is measured to be 1.5-1.8 by *Yohkoh*, *TRACE*, *SOHO*, and *RHESSI* (Crosby et al. 1993; Shimizu et al. 1995; Aschwanden et al. 2000; Benz & Krucker 2002; Christe et al. 2008). Figure 2.3 shows the occurrence frequency distribution. Solar flares including microflares and nanoflares may contribute the heating of the corona (Parker 1988). In paticular, smaller events may play a significant role due to its high frequency, even though a released energy of each event is small (Hudson 1991; Hannah et al. 2008).

2.2 Hard X-Ray Emission

2.2.1 Spectra

HXR imaging and spectroscopy observations of solar flares are provided by the *Yohkoh*/HXT and the *RHESSI* satellite. Although HXT onboard *Yohkoh* (Kosugi et al. 1991, 1992) had a good spatial resolution of ∼5 arcseconds, HXT has only four energy bands for spectroscopy; 14-23, 23-33, 33-53, and 53-93 keV. On the other hand, *RHESSI* has a good energy resolution of ∼1 keV and a wide energy range from ∼3 keV up to ∼10 MeV with a spatial resolution down to 2.3 arcseconds (details in Chapter 3).

Spectra of HXRs are often well-represented by one or more power-laws, and HXRs are thought to be emitted by accelerated electrons of non-thermal power-law distributions. A flux f in power-law distribution is represented by $f \propto E^{-\gamma}$ where E is energy and γ is a constant, called "a photon index". A spectrum with large γ is called a soft spectrum, and a spectrum with small γ is called a hard spectrum. Indices of HXR emissions in solar flares distribute from 2 to 6. Accelerated electrons emit HXRs by the bremsstrahlung process as they travel and lose their energy in the solar corona. HXRs represent properties of non-thermal particles, and HXR observations provide a powerful probe to the mechanism of solar flares. A relation between accelerated high-energy electrons and HXR radiations is likely to be represented by the thick- or thin-target model (Brown 1971), depending on the ambient gas density. While the thick-target model assumes that the density is sufficiently high to lose all energy in the time scale of an observation, the thin-target model assumes that a time scale of energy loss is much larger than that of an observation. Power-law indices of HXR fluxes will be $\gamma = \delta - 1$ or $\delta + 1/2$ for thick and thin target models, where δ is a power-law index of accelerated non-thermal electrons (Koch&Motz 1959; Lin 1974; Hudson et al. 1978).

2.2.2 Time profiles

HXR radiation is impulsively emitted during the rise time of SXRs. By comparing thermal SXRs and non-thermal HXRs, it is known that the time derivative of thermal SXR emissions have similar time profiles to non-thermal HXRs, which is referred to as the Neupert effect (Neupert 1968; Veronig et al. 2005). The Neupert effect indicates that the thermal plasma picks up the energy from the non-thermal electrons. Although the Neupert effect is seen in many events such as shown in Fig. 2.4, deviations are reported in some events (e.g., Warmuth et al. 2009).

By measuring the time evolution of photon indices of HXRs during flares, it is revealed that spectra evolve as soft-hard-soft (spectral indices evolve as large-small-large) in rise-peak-decay phases (Grigis & Benz 2004).

2.2.3 Spatial Structures

HXR imaging observations reveal the spatial structure of particle acceleration in solar flares, including where flare-accelerated energetic electrons are stopped by the high density of the chromosphere (flare footpoints) and where flare-heated plasmas fill magnetic loops. Thermal SXRs represent magnetic flare loops filled with thermal plasma.

In addition to footpoints, a coronal HXR source above the flare loop top was observed by *Yohkoh*/HXT. This event is well known as the Masuda flare (Masuda et al. 1994, Fig. 2.5). This above-the-loop-top source suggests that electrons are accelerated in this region (e.g., Krucker et al. 2010, also see the discussion in Chapter 6), and the origin of solar flares is magnetic reconnection (see the next Section).

HXR radiation from footpoint sources is likely to be produced by the thick target due to the higher density of chromosphere, and the coronal above-the-loop-top source might be represented by the thin target model due to the low density of the corona.

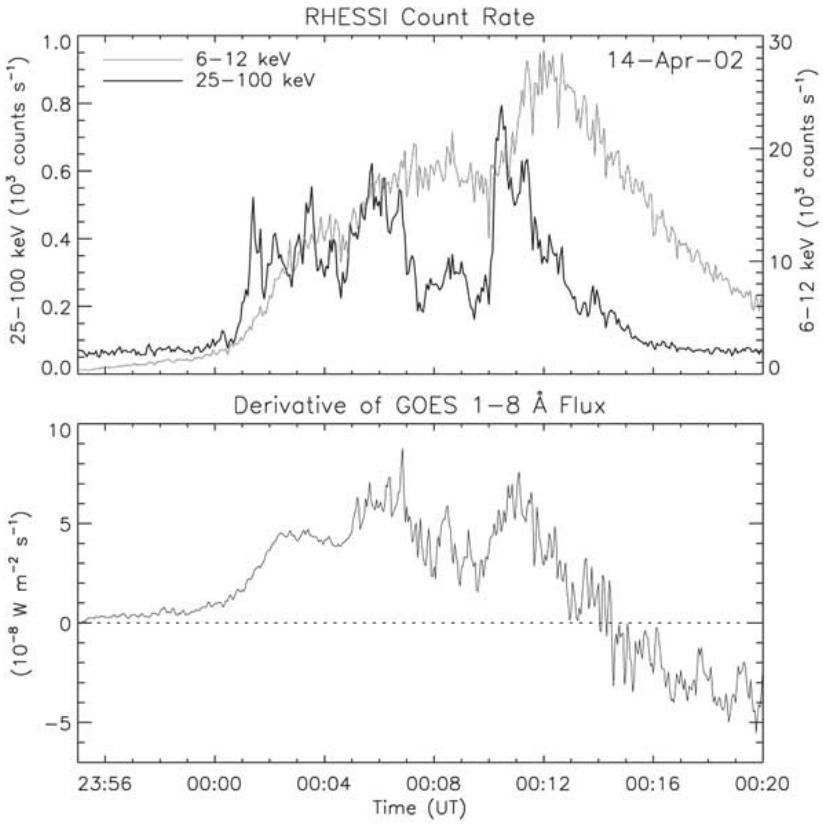

Figure 2.4 Example light curve of the *RHESSI* HXR and the derivative of the *GOES* SXR of the 2002 April 14 flare, in which the Neupert effect is represented (Veronig et al. 2005).

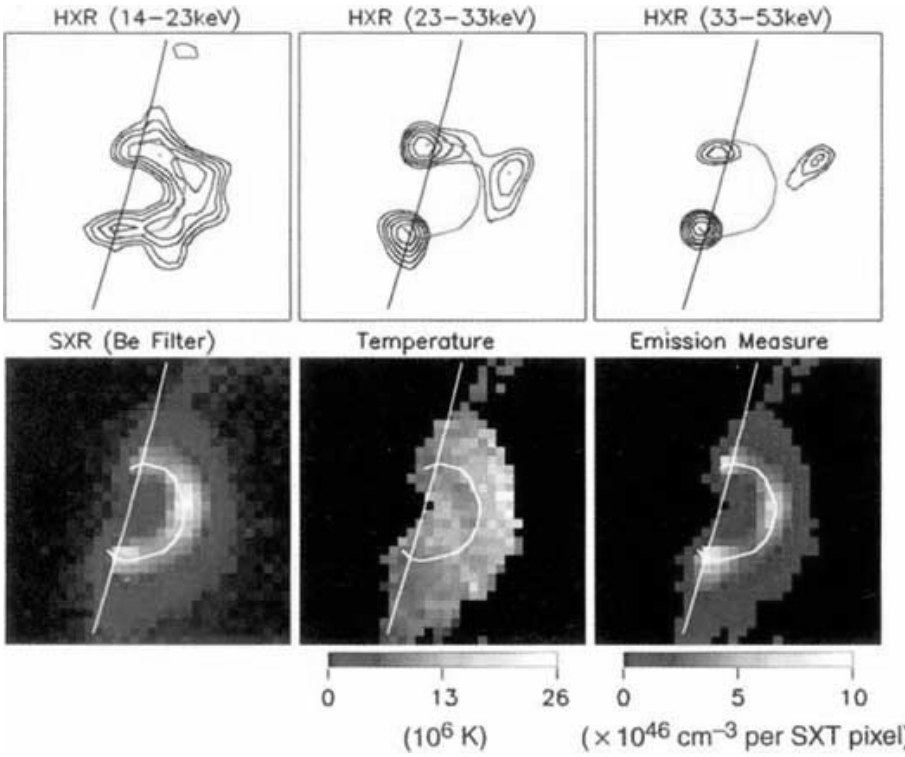

Figure 2.5 *Yohkoh* SXR and HXR images of the Masuda flare (Masuda et al. 1994).

2.3 Magnetic Reconnection

2.3.1 Release of Magnetic Energy by the Reconnection Process

One of the well-accepted theories of a process to convert magnetic energy to kinetic energy in solar flares is magnetic reconnection. The difference of magnetic energy between before and after reconnection is thought to be released as kinetic energy. The idea of magnetic reconnection was first invented around 1940-1950.

One of the primary theories of converting magnetic energies to kinetic energies is a magnetic dissipation. However, it is estimated that the time scale is too long (about $\sim 3 \times 10^5$ years) for the spatial scales of flares.

The magnetic reconnection process occurs as following: Providing there are magnetic fields directed opposite adjacent to each other, a strong current sheet will flow between them. If the current spread away, the magnetic field will reconnect each other into a low-energy configuration. The reconnected magnetic fields have strong magnetic tension and will release energy.

2.3.2 Reconnection Models

One of the simplest models of magnetic reconnection was presented by Sweet and Parker (Sweet 1958; Parker 1963). This model is based on resistive magnetohydrodynamics (MHD) assuming that the length of a current sheet along magnetic fields is much longer than the width. By the Sweet-Parker model, the speed of the reconnection outflow v_o is roughly the Alfvén speed v_A,

$$v_o \sim v_A = \frac{B}{\sqrt{4\pi\rho}} \tag{2.2}$$

where B is the magnetic field strength and ρ is the mass density of the plasma. According to this model, the time scale of energy release τ_r is

$$\tau_r \sim 10^7 \left(\frac{L}{10^9 \text{ cm}}\right)^{3/2} \left(\frac{T}{10^6 \text{ K}}\right)^{3/4} \left(\frac{B}{100 \text{ G}}\right)^{-1/2} \left(\frac{n}{10^9 \text{ cm}^{-3}}\right)^{1/4} \text{ s}, \tag{2.3}$$

where L is the spatial scale, T is the plasma temperature, and n is the number density. Although this time scale is shorter than the case of magnetic dissipation, it remains still too long for ordinary flare events.

To solve this difficulty, a revised model was proposed by Petschek (1964). In the Petschek model, the length of the current sheet is assumed to be smaller, comparable to the width. The energy conversion is thought to be done by the slow-mode MHD shock. In this model, the time scale τ_r can be shortened by assuming that the current sheet is sufficiently small, such as

$$\tau_r \sim (10 - 100) \times t_A \text{ s}, \tag{2.4}$$

where $t_a = L/v_A$ is the Alfvén time scale. Since $t_A \sim$ 1-10 s, then solar flares can be explained by magnetic reconnection.

By MHD simulations, magnetic reconnection is confirmed to be a possible solution (e.g., Ugai & Tsuda 1977).

2.3.3 Flare Model

The well accepted model of solar flares based on magnetic reconnection is called the CSHKP model, from initials of the proposing authors (Carmichael 1964; Sturrock 1966; Hirayama 1974; Kopp & Pneuman 1976). The scenario is as follows; Particle acceleration and heating of coronal plasma will be accompanying magnetic reconnection in the corona, and accelerated non-thermal particles will reach and heat chromospheric plasma. Heated chromospheric plasma will evaporate and fill the flare loop along the magnetic field lines. Figure 2.6 shows two schematics of the standard flare model of magnetic reconnection. Basic structures of a flare with reconnection are calculated by MHD simulations (e.g., Yokoyama & Shibata 1998, the bottom panel of Fig. 2.6). Note that the mechanism of particle acceleration is not included in the CSHKP model and not well understood.

The standard model is supported by several observations by *Yohkoh*: the cusp shaped SXR flare loop (Tsuneta et al. 1992), the downward outflow from magnetic reconnection (McKenzie & Hudson 1999), the inflow (Yokoyama et al. 2001),

the plasma ejection (Ohyama & Shibata 1997), the coronal above-the-loop-top HXR source of the Masuda flare (Masuda et al. 1994) which suggests that the energy release in a solar flare is outside the magnetic loop.

2.4 Particle Accelerations

2.4.1 Properties of Accelerated Particles in Solar Flares

Although non-thermal HXRs are thought to be emitted by accelerated high-energy electrons, the properties of accelerated particles and the acceleration mechanism are still not well understood.

Acceleration regions of high-energy particles are not easy to determine, because accelerated particles need target particles in order to radiate HXR bremsstrahlung emission. By comparing the energy dependency of the delay of emission in footpoints, it is revealed that the acceleration region is above the flare loop top, assuming that all electrons are accelerated simultaneously in the same region (Aschwanden et al. 1996). The time scale of the HXR emission is observed as <1 s, suggesting that the time scale of acceleration is shorter than a second.

According to HXR emission in the impulsive phase, a large number of accelerated particles is required: $\sim 10^{39}$. However, this number cannot be explained by any observational evidence of inflow and volumes of reconnection sites. This problem is referred to as the "number problem" of energetic particles. "Recycling" of electrons, a repeating of acceleration and energy loss by emission, may be needed to solve this problem. We note that the number and total energy of accelerated particles depend strongly on the energy of a low-energy cut-off in the electron distribution, which produces a rollover at the same energy in the photon spectrum.

2.4.2 Acceleration Mechanisms

Theoretically, the acceleration mechanisms can be classified into roughly three types: electric field acceleration, stochastic acceleration, and shock acceleration.

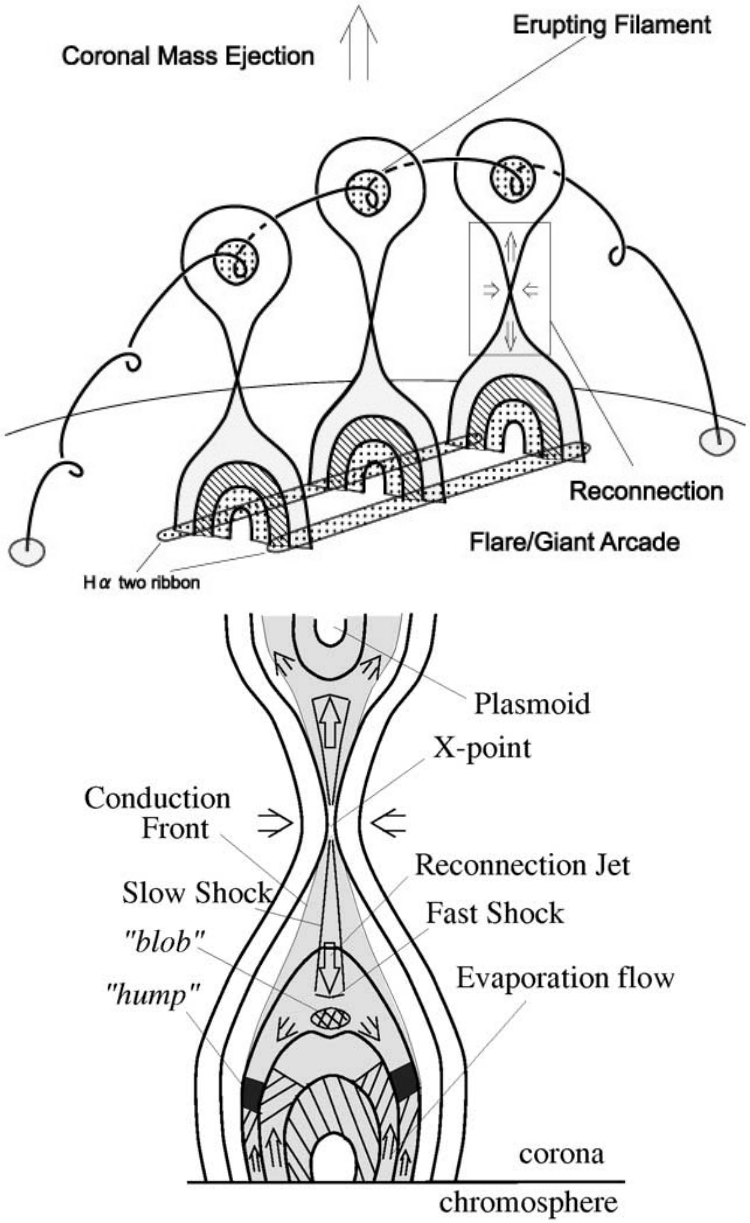

Figure 2.6 Schematic illustrations of flare models. *Top*: Giant arcade structure (Shiota et al. 2005). *Bottom*: Simulated illustration of flares by magnetic reconnection (Yokoyama & Shibata 1998).

Under the stronger and stronger electric fields, electrons with high speeds can escape from the region of a thermal Maxwellian distribution. The electric field strength by which electrons are accelerated to the speed of escape is called the Dreicer field (Dreicer 1959). The Dreicer field is strong when the density is high and the temperature and magnetic field are low. While an electric field stronger than the Dreicer field can be present in the corona, it is rarely achieved in the chromosphere (e.g. Holman 1985; Aschwanden 2005).

The stochastic acceleration mechanism energizes particles by multiple collisions in turbulence (Fermi 1949). Particles are accelerated by the difference of collisional probabilities between the case that particles move the same direction and the case of the opposite direction to the flow. As a result, the energy gain is proportional to the second power of a speed ratio V/v where V is a flow speed and v is a particle speed, and the stochastic acceleration is referred to as second-order Fermi acceleration.

In the shock acceleration mechanism, particles are accelerated by multiple collisions back and forth between a shock front (Krymskii 1977; Blandford & Ostriker 1978). Acceleration is due to the difference of velocities and densities between upstream and downstream. The energy gain is proportional to the speed ratio u/v where u is the speed of the shock, and the shock acceleration is called the first-order Fermi acceleration. Particles accelerated by shock acceleration will have a power-law distribution. Therefore, accelerated high-energy particles which emit HXRs could be related to a shock accompanied with magnetic reconnection. Indices of the power-law depend on an energy gain ratio and a probability of remaining in an acceleration region.

Chapter 3

The Reuven Ramaty High-Energy Solar Spectroscopic Imager (*RHESSI*)

3.1 *RHESSI* Satellite

RHESSI (Fig. 3.1) is the first solar observation mission for HXR and γ-ray imaging and spectroscopy up to 17 MeV, launched in 2002 (Lin et al. 2002). The principal scientific objective is to investigate particle acceleration and energy release in solar flares. Imaging of above 100 keV photons, including individual γ-ray line emissions produced by energetic ions, is possible for the first time by *RHESSI*. Accelerated electrons emit non-thermal HXR continuum above $\sim$10 keV by bremsstrahlung, and the neutron capture line of 2.2 MeV is emitted by accelerated ions.

The imaging method of the *RHESSI* instrument is rotating modulation collimators (RMCs). Images are obtained by Fourier reconstruction. *RHESSI* has nine germanium detectors and nine corresponding bi-grid subcollimators. Each subcollimator grid has a different slit pitch and thickness. Spatial resolution varies from 2.3 to 183 arcseconds, depends on a pitch of each grid (details in Section 3.3). The highest energy imaged depends on the thickness of the grids and varies from 100 keV to 10 MeV.

Energy range	$\sim$3 keV to 17 MeV
Energy resolution (FWHM)	$\lesssim$1 keV at 3 keV, increasing to $\sim$5 keV at 5 MeV
Angular resolution (FWHM)	2.3 arcseconds to 100 keV, 7 arcseconds to 400 keV, 36 arcseconds to 15 MeV
Field of view	full Sun ($\sim 1^\circ$)
Effective area (photopeak)	$\sim 10^{-3}$ cm^2 at 3 keV, $\sim$32 cm^2 at 10 keV (with attenuators out), $\sim$60 cm^2 at 100 keV, $\sim 15^{-3}$ cm^2 at 5 MeV
Launch date	5 February, 2002

Table 3.1 *RHESSI* characteristics (Lin et al. 2002).

RHESSI has an energy resolution of a few keV, superior to former solar HXR telescopes. While HXT of the *Yohkoh* Satellite has only 4 energy bands and the energy resolution is $\sim$20 keV (Kosugi et al. 1991, 1992), the energy resolution of *RHESSI* enables us to determine photon indices of HXR continuum emitted from accelerated electrons in each flare. With a fine spatial resolution of $\sim$2.3 arcseconds, spatial structures of flares can be resolved, and spectral structures and time dependence of each source of the flare can be investigated. Hence, spatially separated analysis of coronal loop-top sources and footpoint sources have become possible. The large effective area and sensitivity of *RHESSI* together with the energy response down to 3 keV make it possible to detect solar flares from large flares to microflares. *RHESSI* has detected more than 80000 flares (from February 2002 to December 2010). Table 3.1 shows characteristics of the *RHESSI* instrument.

3.2 Spectroscopy by *RHESSI*

The *RHESSI* detector has a wide energy rage, good energy resolution and high effective area (Smith et al. 2002). Nine germanium detectors, 7.1 cm diameter $\times$

Figure 3.1 The *RHESSI* satellite (from *RHESSI* Home Page, http://hesperia.gsfc.nasa.gov/hessi/).

8.5 cm each in size, are cooled to <75 K with a Stirling-cycle cooler. The high effective area up to ∼10 MeV is achieved via the thickness of the detector. For large flare events, a movable attenuator reduces the flux of low-energy photons to avoid saturation and pile-up. *RHESSI* has two attenuators with different thicknesses. The attenuator configuration has three states; without the attenuators (A0), with the thin attenuator only (A1), or with both attenuators (A3).

Electrically, each detector has two segments and signals from each segment are read out separately. Fig. 3.2 shows a cross sectional view of the detector with the segment boundary of front and rear. Front segments, placed in the direction of the Sun, have a thickness of ∼1 cm and have sensitivity to low-energy (<200 keV) photons. On the other hand, rear segments with a thickness of ∼7 cm are used for high-energy (>200 keV) photons. The effective area of the front and rear segments are comparable at ∼200 keV (shown in Fig. 3.3). Therefore, rear segment data are needed to study high energy emissions from relativistic electrons. Table 3.2 shows in-flight energy resolution of the front and rear segment of each subcollimator. Resolution is

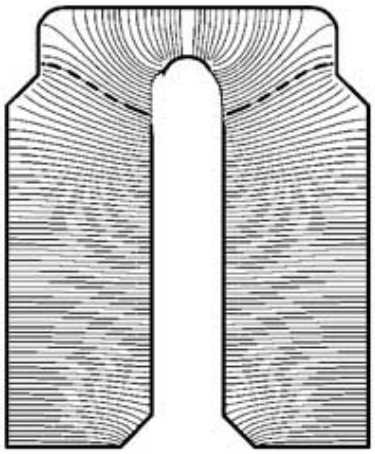

Figure 3.2 Cross sectional view of a *RHESSI* detector with field lines (Smith et al. 2002). The bold dash line shows the segment boundary. The top part of the detector is the front segment.

measured at 93.9 keV in the front segments and 1117 keV in the rears.

Due to mass restrictions, *RHESSI* utilizes a high effective area instead of heavy shielding. Hence, *RHESSI* has a large volume of detectors, but a high background. However, the background can be reduced by using anticoincidence between front and rear segments. The two segments of the detector work similar to a phoswich counter, and events of Compton scattering or charged particles can be discriminated. The photon events in which we are interested will only be measured once for each photon, not in both segments. Due to the large volumes of the rear segments, the background is higher than that of front segments by one order of magnitude. In spite of the high background, imaging and spectroscopy with the rear segment is possible for large flares.

For large flare events with high count rates, pile-up becomes considerable, especially in the front segments. The readout electronics of each segment have a fast shaping channel (time constant τ $\sim$800 ns) and slow shaping channel (τ $\sim$8 μs) for spectroscopy, and pile-up can be discriminated by the fast pulse. The rear segments of the detectors have a feature of low pile-up, because the front segments act as a

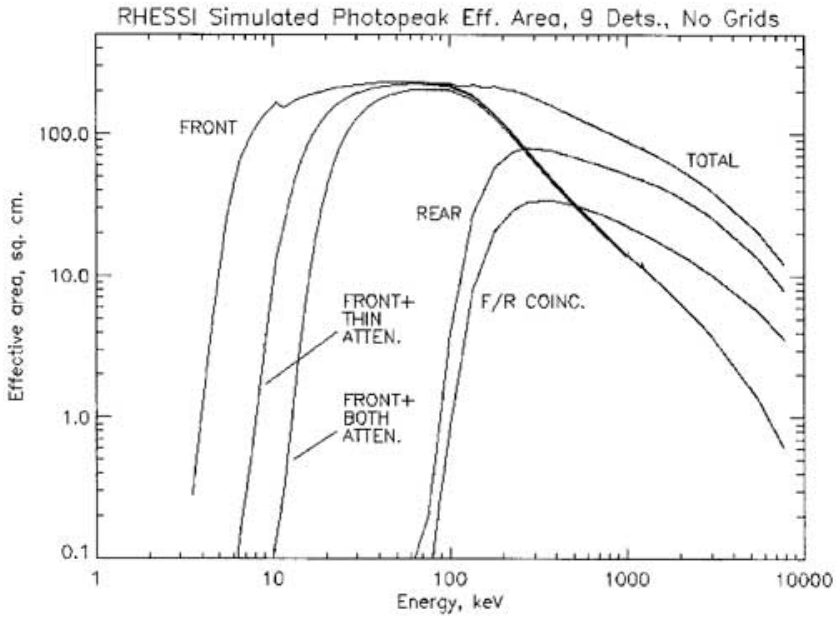

Figure 3.3 *RHESSI* front and rear segment effective areas for photopeak absorption, summed over all 9 detectors (Smith et al. 2002).

Detector	Front FWHM (keV)	Rear FWHM (keV)
G1	1.13	2.90
G2	7.94	...
G3	0.98	2.77
G4	0.98	2.82
G5	1.47	2.73
G6	1.01	3.05
G7	3.15	2.98
G8	1.26	3.36
G9	1.19	2.27

Table 3.2 *RHESSI* in-flight resolution by detector segment (Smith et al. 2002). Resolution is measured at 93.9 keV in the front segments and 1117 keV in the rears.

shield. Therefore, rear segment data provides imaging without pile-up effects even for extremely large flares.

If the memory starts to fill up, a decimation state changes and one out of every N events below a certain energy E is recorded in the front detector (FDN state). N and E are determined automatically by the remaining memory.

Fig. 3.4 is an example of a *RHESSI* spectrum, from the January 20, 2005 event. Light curves of the same event from front and rear segments are plotted in Fig. 3.5. Two discontinuous changes of the low energy count rates of 10-50 keV are seen, which correspond to changes of the attenuator state and the decimation state.

3.3 Imaging by *RHESSI*

Images from *RHESSI* are obtained by RMCs with a rotation period of ∼4 seconds (Hurford et al. 2002). A schematic of the *RHESSI* subcollimators is shown in Fig. 3.6. Incident X-rays display a modulation pattern on the detector due to the rotation of the satellite. The profile of a modulation curve depends on an incident direction and emission strength of a source. Fig. 3.7 shows examples of modulation profiles for a variety of sources. Multiple sources are observed as a superposition of individual modulation curves.

The *RHESSI* subcollimators have different grid thicknesses and slit widths. Depending on the thickness of the grids and the slit width, the maximum energy that can be imaged differ from ∼100 keV to ∼10 MeV and the spatial resolution differs from ∼2.3 to ∼ 183 arcseconds. As is discussed in Hurford et al. (2003), images are susceptible to forward scattering from the grids especially for higher energies such as >1 MeV, which lowers the effective modulation amplitude. Parameters of *RHESSI* imaging for each subcollimator grid are listed in Table 3.3. To reconstruct sources significantly by using finer subcollimators, more statistics are necessary. We used subcollimators including the finest resolutions as far as significant sources are seen in images.

To obtain an image from a modulation curve, different image reconstruction methods are used (Hurford et al. 2002). While there are various kind of methods, back

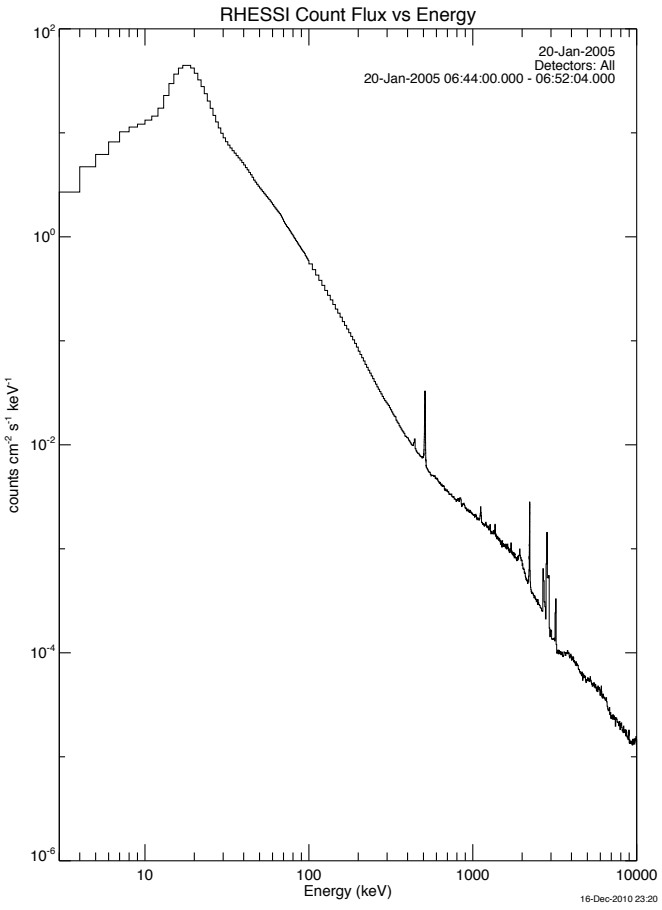

Figure 3.4 *RHESSI* count spectrum of the January 20, 2005 flare including the front and rear segments. This spectrum is observed with both attenuators in front of the detectors. Therefore, the spectrum below ∼20 keV is heavily attenuated. Several line emissions, including 511 keV positron annihilation line and 2.2 MeV neutron capture line are seen.

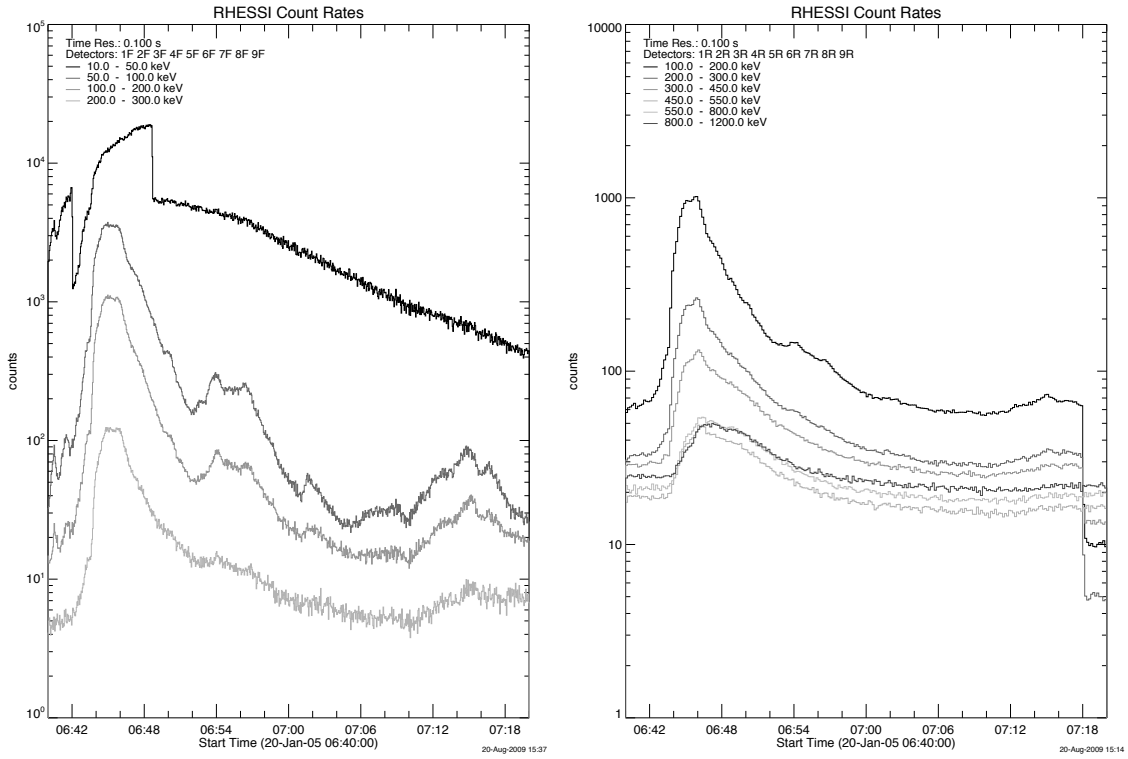

Figure 3.5 *RHESSI* light curves of the January 20, 2005 flare with the front segments (left) and rears (right). An attenuator state changed from A1 to A3 at around 06:42, and a decimation state changed from FD1 to FD4 at around 06:49. These changes are responsible for the step-like decrease in the low energy light curves.

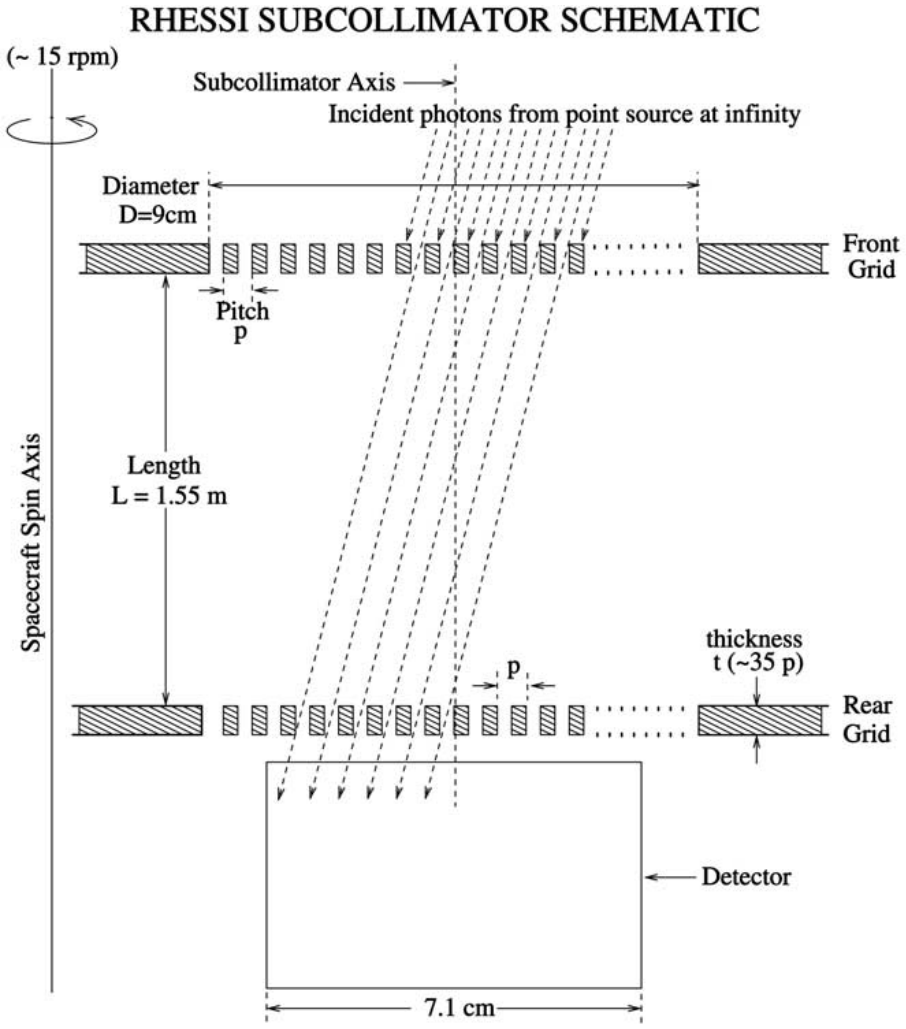

Figure 3.6 Schematic geometry of the *RHESSI* subcollimators (Hurford et al. 2002).

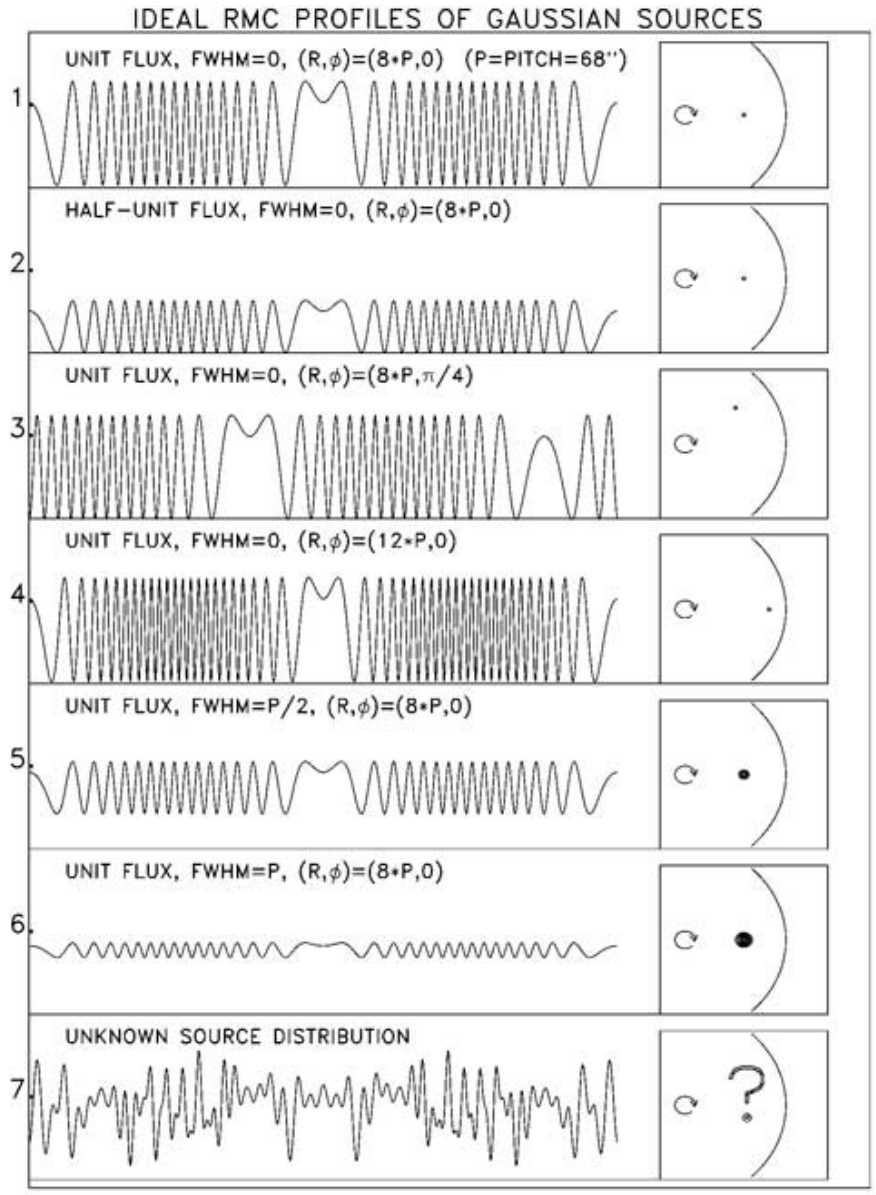

Figure 3.7 *RHESSI* modulation profiles of various sources (Hurford et al. 2002). An upper limit of a modulation curve is higher if a flux is higher, and a lower limit higher with a larger source. While a frequency corresponds to the distance from a rotation center, a difference of a phase corresponds to a direction of a source.

Subcollimator	1	2	3	4	5	6	7	8	9
Pitch (mm)	0.034	0.059	0.102	0.177	0.306	0.530	0.918	1.590	2.754
slit width (mm)	0.020	0.035	0.061	0.106	0.184	0.318	0.477	0.811	1.487
FWHM resolution (arcseconds)	2.26	3.92	6.76	11.76	20.36	35.27	61.08	105.8	183.2
Max. transmission	0.60	0.60	0.60	0.60	0.60	0.60	0.52	0.51	0.54
Grid thickness (mm)	1.2	2.1	3.6	6.2	10.7	18.6	6.2	6.2	30.0
Maximum imaging energy (MeV)	0.1	0.3	0.4	0.6	1	10	0.6	0.6	10
Slat Material	Mo	W	W	W	W	W	W	W	W
Field of view (degree)	1.0	1.0	1.0	1.0	1.0	1.0	4.4	7.5	2.8

Table 3.3 *RHESSI* nominal grid parameters (Hurford et al. 2002).

projection is the most straight forward imaging algorithm (Hurford et al. 2002). A back projection image is obtained by superposing transmission pattern of collimators. The patterns are superposed with weighting factors, which are determined by the flux of each time bin in the modulation curve. If a flux is high in a corresponding time bin, a pattern has a high contribution. By superposing back projections from each subcollimator, a back projection from the whole imaging system can be obtained. Although it is possible to superpose each back projection with the same weighting ("natural" way), a better image can be obtained by weighting finer grids to a uniform weighting in Fourier space ("uniform" way). The point spread functions (PSFs) of *RHESSI* back projections from grid 8 are plotted in Fig. 3.8 at typical energy bands used in the following chapters, 12-15 keV, 50-100 keV and 150-450 keV. As shown in Fig. 3.8, the PSF is represented not by a simple Gaussian, but by the zero-order Bessel function $J_0(\pi r/R)$ where R is the FWHM resolution (Hurford et al. 2003). This makes it difficult to separate multiple sources, especially if strengths of sources are largely different. Dynamic range is higher for high count rates, varies for each event. The dynamic range of *RHESSI* is typically $\sim$5.

We used the imaging method of Clean (Hurford et al. 2002) to make images using the front and rear segments. The Clean method assumes that the image can be well represented by a superposition of point sources. By the Clean method, an image can be improved compared to a back projection image, even if statistics are low. First, Clean finds the position with maximum flux in the back projection map. Then, the position is stored as a Clean component, and the PSF times a constant value μ ($\mu < 1$) is subtracted at this position from the back projection. A Clean image is obtained by adding a residual map and the Clean component times the Clean PSF, which is a simple Gaussian with the same FWHM as the PSF. Subsequently, the position with maximum flux in the residual map is searched, and stored to the Clean component table. The Clean image can be improved by repeating this procedure. Since a normalization of the Clean PSF is determined to conserve the flux, a source flux can be calculated using an image obtained by Clean. Hence, in case multiple sources are well-separated, the calculated value of the flux for each source is reliable. We used fluxes obtained by Clean images for spectroscopy of HXR sources in the

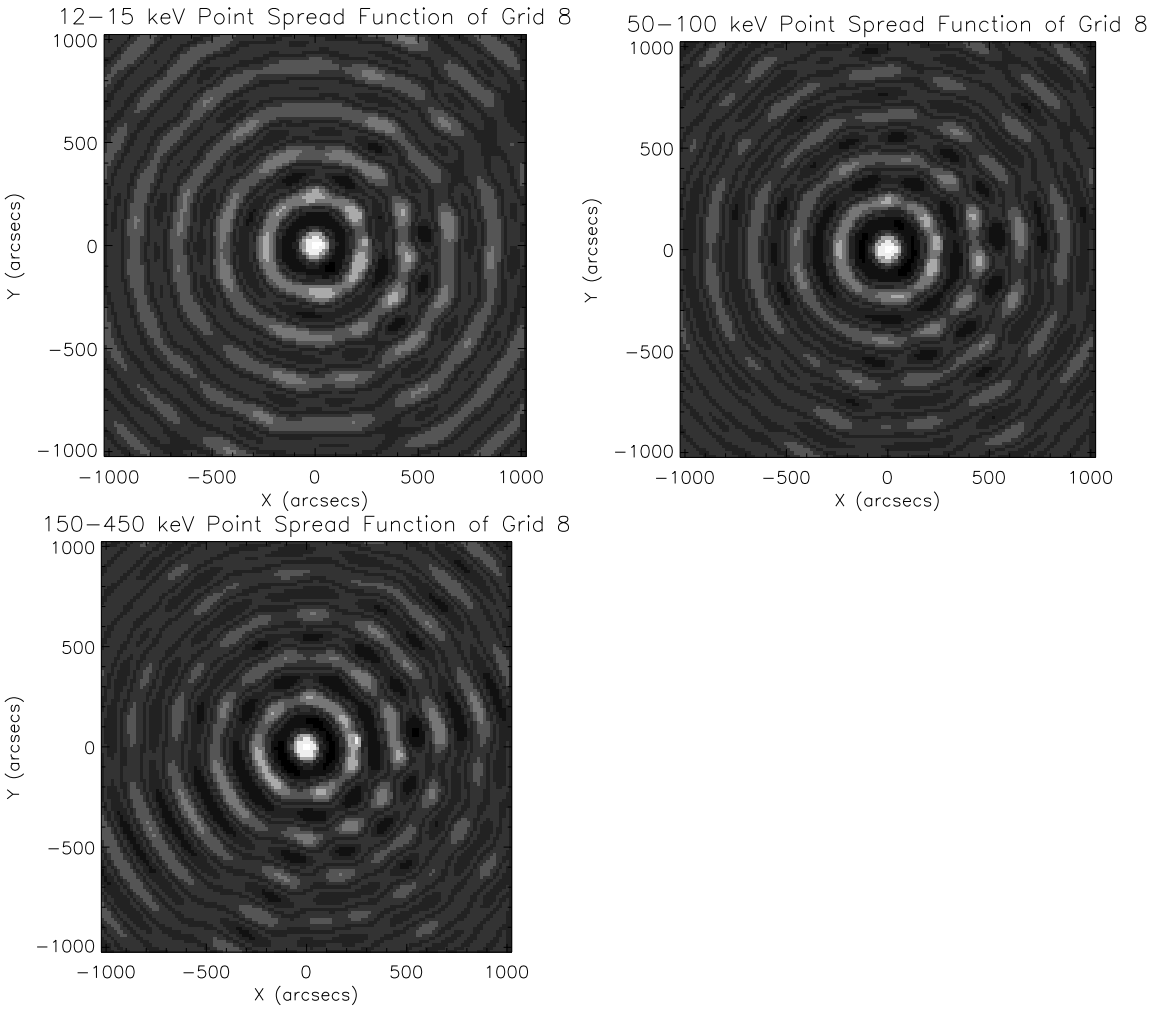

Figure 3.8 Point spread functions of the *RHESSI* detector grid 8 of 12-15 keV, 50-100 keV (top left and right, with the front segment) and 150-450 keV (bottom, with the rear segment). These PSFs are obtained by the condition of the January 20, 2005 flare observation.

following chapters. In the images in the following chapters reconstructed by Clean, we use the constant value of $\mu = 0.1$ for data from the front segments, and $\mu = 0.05$ for the rear segments.

In addition to Clean, the Maximum Entropy Methods (MEM) is effective to make a smoother image. MEM reconstructs an image to find the solution with maximum configuration entropy which agrees with the observation. This means that an image by MEM is in principle, as simple as possible while being consistent with the observation. MEM was originally developed for *Yohkoh*/HXT (Sato et al. 1999). To discuss spatial structures using smoother images, we used MEM to make clear images of the event with relatively high counts, such as images using whole duration of the flare and/or large energy band.

A comparison of a *RHESSI* back projection and images of 50-100 keV are shown in Fig. 3.9, from the January 20, 2005 event. The images are reconstructed by Clean and MEM.

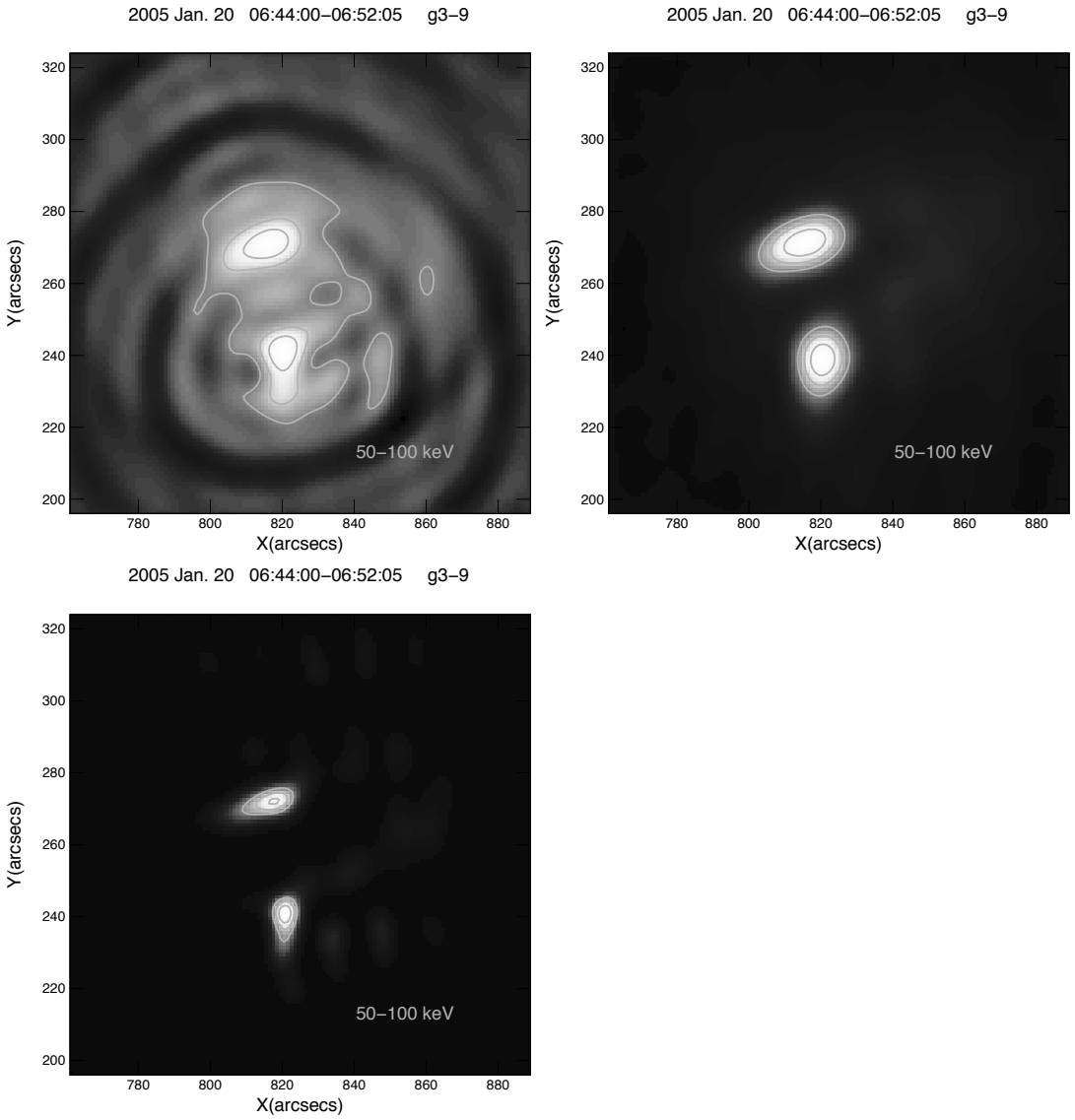

Figure 3.9 *RHESSI* back projection (top left) and images of the January 20, 2005 flare using the subcollimators 3-9. The images are reconstructed by the Clean (top right) and MEM (bottom left) methods. Contour levels of 40, 60, 80 % are plotted. The energy band is 50-100 keV.

Chapter 4

RHESSI HXR Imaging Survey from Relativistic High-energy Electrons in Large Flares*

4.1 HXR emissions from relativistic high-energy electrons in flares

In solar flares, electrons are accelerated to relativistic energy up to tens of MeV, and ions up to tens of GeV. In the non-relativistic energy band (i.e. <100 keV photons), many HXR images are provided by *Yohkoh*/HXT and studied further. However, it was not possible to obtain images of relativistic electrons (i.e. >150 keV photons) due to the limitation of the energy band of *Yohkoh*/HXT. Therefore, it is little known on the spatial structure of relativistic particles. Using the *RHESSI* rear segments of the detectors (see Section 3.2), we are able to obtain HXR images from relativistic particles at the first time.

* The content of this section is published by ApJ, Vol. 727, article id. 22, 2011, entitled "*RHESSI* Imaging Survey of γ-ray Bremsstrahlung Emission in Solar Flares" by S. Ishikawa, S. Krucker, T. Takahashi and R. P. Lin.

RHESSI observed 26 γ-ray flares (i.e. flares with emission above 300 keV) so far (Shih et al. 2009). Non-thermal bremsstrahlung emissions in the >150 keV range are produced by relativistic electrons. Several single event studies of *RHESSI* imaging above 150 keV have been published. In the flare of 2002 July 23, the location of electron bremsstrahlung emissions in 300-500 keV band and the neutron capture line of 2.223 MeV are spatially separated by $20'' \pm 6''$, implying a difference in acceleration site and/or transport effects for electrons and ions (Hurford et al. 2003). In Hurford et al. (2006), 200-300 keV images from electrons and 2.223 MeV line images from ions in the 2003 October 28 and 29, November 2 flares are compared. The October 28 event, which has the best counting statistics by far, shows two footpoints at 2.223 MeV that originate from the flare ribbon seen in extreme ultraviolet. The electron footpoints are again displaced by $17 \pm 5''$, but electron and ion accelerations appear to happen on flare loops of similar length, since the distances of the two footpoints are similar ($\sim 80''$) at the two energy bands. In the 2005 January 20 flare, two footpoints are clearly seen at 250-500keV, with a coronal source appearing during the decay phase (Krucker et al. 2008a). The limb event of 2005 September 7 shows a similar source, unambiguously locating these sources in the corona. These coronal γ-ray sources show that relativistic electrons stay long enough in the corona to lose their energy by collision in the corona, while lower energy electrons precipitate much faster. Some proposed mechanisms to explain a long time coronal trapping are shown in Section 6.6.

In this chapter, an imaging survey of all *RHESSI* γ-ray flares is presented and discussed. In the γ-ray range (>300 keV), grid 1 and 2 are not thick enough to modulate counts. While grid 3 works up to ~400 keV, all others work up to at least ~600 keV (Hurford et al. 2002). For our survey, we use rear segment data of subcollimators 3 to 9 or subcollimators 4 to 9 depending on image quality. For comparison, we also make images with the same subcollimator using front segment data at lower energy (50-100 keV). We use the CLEAN algorithm, providing a FWHM resolution of $\sim 10''$ for subcollimators 3 to 9 and $\sim 17''$ for subcollimators 4 to 9.

4.2 Event selection

We analysed 26 γ-ray flares observed by *RHESSI* from the event list of Shih et al. (2009). This list contains all events seen above 300 keV. Hence, we exclude rear segment flare events seen only below 300 keV. However, these events are expected to be small in number. Since some of the events in the list already do not have good statistics to provide images (see Section 4.3), omitting rear segment flare events, which are seen only below 300 keV, does not influence the results presented here. To enhance statistics, we make flare-integrated images over all rear segment counts (> 150 keV). Table 4.1 shows the list of analysed events and their properties. The *GOES* class of these events varies from C9.6 to X17. In Appendix A, we show 150-450 keV (from the rear segments) light curves with 50-100 keV (from the front segments) of all the flares in this list. The time intervals shown are determined from light curves of > 150 keV of the rear segments. For imaging, we exclude times of attenuator changes. As described in Shih et al. (2009), two clearly separated peaks are seen in three flares. For these events, we analyzed the two time intervals separately.

Table 4.1. Table of properties and imaging results of analyzed flare events.

Date and Interval (UT)	*GOES* Class	Location ($''$)	>150 keV Fluence (ph cm^{-2})	Number of footpoints (50-100 keV)	(150-450 keV)	footpoint separation ($''$)	pileup (%) (50-100 keV)
2002 Feb 26 10:26:00-10:28:01	C9.6	(930, −230)	179 ± 35	1	-		3
2002 May 31 00:06:00-00:09:02[a]	M2.4	(−820, −480)	364 ± 34	2	-	33*	1
2002 Jul 20 21:07:00-21:12:03[a]	X3.3	(−940, −200)	2593 ± 67	-	-		19
2002 Jul 23 00:27:00-00:30:02	X4.8	(−870, −230)	25285 ± 81	2	2	27	18
2002 Aug 20 08:24:00-08:28:02	M3.4	(580, −260)	452 ± 70	3	-		7
2003 Apr 26 08:05:00-08:08:22	M7.0	(850, 330)	582 ± 36	1	1		3
2003 May 27 23:04:00-23:08:02	X1.4	(270, −100)	52.2 ± 2.9	1	1		4
2003 Jun 17 22:53:00-22:56:02	M6.8	(−790, −140)	3281 ± 45	2	2	35	6
2003 Oct 28 11:08:00-11:11:02[c,d]	X17	(−90, −370)	$> 98514 \pm 127$	2	2	94	58
2003 Oct 29 20:39:00-20:47:05[b]	X10	(90, −380)	...	2	2	44	39
2003 Nov 2 17:16:00-17:24:05[d]	X8.3	(770, −340)	74592 ± 172	2	2	37	43
2003 Nov 3 09:48:00-09:52:02	X3.9	(920, 130)	2419 ± 55	2	1	17*	35
09:58:00-10:01:42[d]			855 ± 51	2	2	40	21
2004 Jan 6 06:22:00-06:24:01[a]	M5.8	(-970, 90)	654 ± 16	2	2	75	3
2004 Jul 15 01:37:00-01:40:02	X1.8	(−750, −190)	28.7 ± 3.1	1	-		6

Table 4.1 (cont'd)

Date and Interval (UT)	*GOES* Class	Location ($''$)	>150 keV Fluence (ph cm^{-2})	Number of footpoints (50-100 keV)	(150-450 keV)	footpoint separation ($''$)	pileup (%) (50-100 keV)
2004 Jul 15 18:21:00-18:24:02	X1.6	$(-650, -230)$	96.7 ± 5.3	1	1		13
2004 Jul 16 02:02:00-02:05:02	X1.3	$(-610, -230)$	17.5 ± 4.0	2	-	25*	8
2004 Nov 10 02:08:00-02:12:02	X2.5	(700, 90)	3756 ± 72	2	2	16	6
2005 Jan 15 22:44:00-22:47:02[d]	X2.6	(110, 310)	$> 16597 \pm 163$	2	1	39*	7
2005 Jan 17 09:43:00-09:46:02	X3.8	(440, 300)	16512 ± 120	2	2	40	9
2005 Jan 19 08:12:00-08:17:03	X1.5	(700, 280)	3996 ± 72	2	1	43*	8
08:24:00-08:30:04			11723 ± 98	2	1	68*	2
2005 Jan 20 06:44:00-06:52:05	X7.1	(820, 250)	204495 ± 312	2	2	35	32
2005 Aug 25 04:36:00-04:40:02	M6.4	$(-920, 120)$	3525 ± 52	1	2	17	5
2005 Sep 7 17:43:00-17:47:02[a,b,c,d]	X17	$(-960, -210)$	...	0	1		42
2005 Sep 9 20:04:00-20:12:05[c]	X6.2	$(-830, -270)$	$> 945 \pm 12$	2	1	87*	9
2005 Sep 10 21:33:00-21:36:02	X2.1	$(-660, -260)$	200 ± 5.8	2	1	24*	5
21:55:00-21:58:02[d]			$> 249 \pm 4.4$	-	-		5
2005 Sep 13 23:18:00-23:22:02	X1.7	$(-30, -300)$	51.4 ± 4.8	2	-	21*	22

Note. — (a) occurred near or over the solar limb, (b) poor background subtraction, (c) missing beginning data, (d) missing end data (Shih et al. 2009), (*) determined by the 50-100 keV image (others are by the 150-450 keV image)

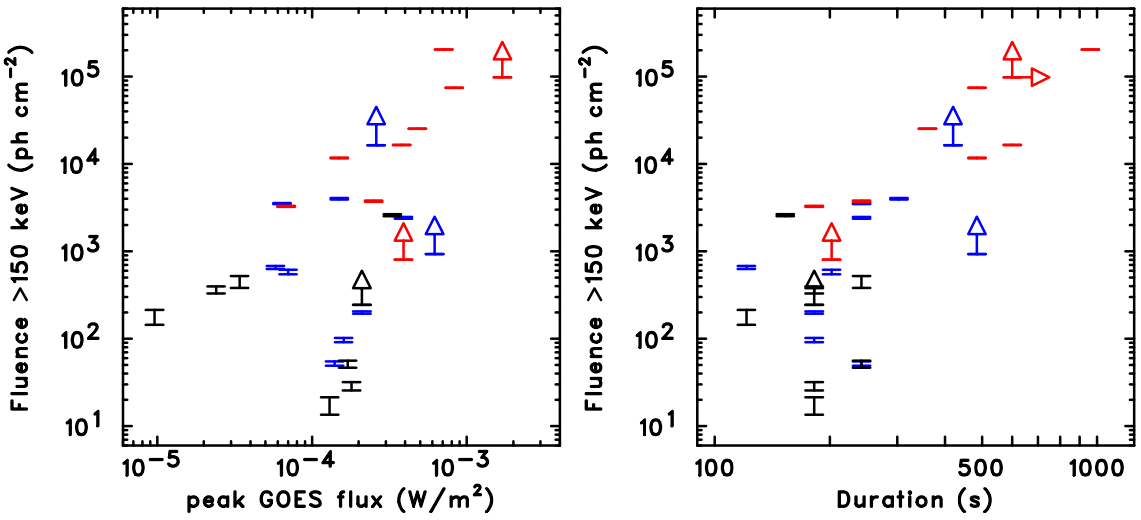

Figure 4.1 *Left*: Fluence >150 keV vs *GOES* flux. *Right*: Fluence >150 keV vs duration. Colored points indicate those for which a detailed image was obtained in the 150-450 keV band (events with a double source structure are shown in red, while events with a single source are shown in blue). For the remaining events (black) no detailed imaging information could be derived. Events for which only lower limits of the total fluence are available are marked by arrows (see Shih et al. 2009 for details).

4.3 Imaging results

As image quality depends heavily on counting statistics, we first discuss the >150 keV fluence of the selected events. Figure 4.1 shows the >150 keV fluence against *GOES* peak soft X-ray flux and total duration of the >150 keV emission for all of the selected events. Events for which a detailed image could be reconstructed are shown in color (21 out of 29 time intervals). These events have a >150 keV fluence of at least several hundred photons per cm^2. For the remaining events, counting statistics are too poor for detailed imaging, and only a centroid location of the >150 keV flux could be determined. The events given in red reveal two footpoints, while events shown in blue show a single source. In Fig. 4.2, the spatial distribution of the events are shown. As is reported in the low energies (e.g., Saint-Hilaire et al. 2008), most of the flares were occurred in rather low latitudes. All of the events in the list

are within $\pm 30^\circ$ in latitude. In fact, multiple γ-ray flares were occurred in some of the active regions, such as the events in October and November 2002, January 2005, and September 2005. Although it is suggested that γ-ray flares are more likely detectable around the limb due to the Compton degradation (Kotoku et al. 2007), we find no clear deviation of the positions of the γ-ray flares in the longitude. The >150 keV fluence against the absolute longitude (corresponding to the distance from the disk center) is plotted in the bottom panel of Fig. 4.2. We find no clear correlation between the fluences and the longitudes, and more events are thought to be necessary to confirm the correlation.

All images of flares that successfully imaged in 150-450 keV are shown in Fig. 4.3. Again, there is a dependence on counting statistics. Two-footpoint events have higher fluences than single source events, suggesting that events with a single source could have a second footpoint that is hidden in the noise. Imaging at lower energies with much better statistics confirms this, showing several events with two footpoints (e.g., 2005 January 19). Some events with a single source at >150 keV, however, are spatially unresolved (e.g., 2003 April 26). Taking the different dynamic range of the 50 keV and 150-450 keV images into account, the source morphology at both energy ranges are generally the same. Slight differences in position of the two footpoints, such as seen in the 2004 January 6 event where the weaker footpoint at higher energies is shifted relative to the location of the footpoint at 50-100 keV, are an artifact of the limited counting statistics. The main difference between the front and rear images can be attributed to pile-up. In large flares such as those investigated here, the large number of thermal photons detected produce significant pile-up events. As most low energy photons are absorbed in the front segments, almost all pile-up counts are registered in the front segment. Rear segment data generally does not suffer from pile-up effect (Smith et al. 2002). For our set of events, the fraction of pile-up counts are estimated to be between a few percent up to 60% (see Table 4.1 and top left corner of images shown in Fig. 4.3). These values are rough estimates averaged over a spin period ($\sim$4 s). Hence, during peak times in the modulation pattern, the fraction of pile-up counts is significantly higher than the reported average value. Although the effects of pile-up on imaging are complex, to the first order, pile-up events by two

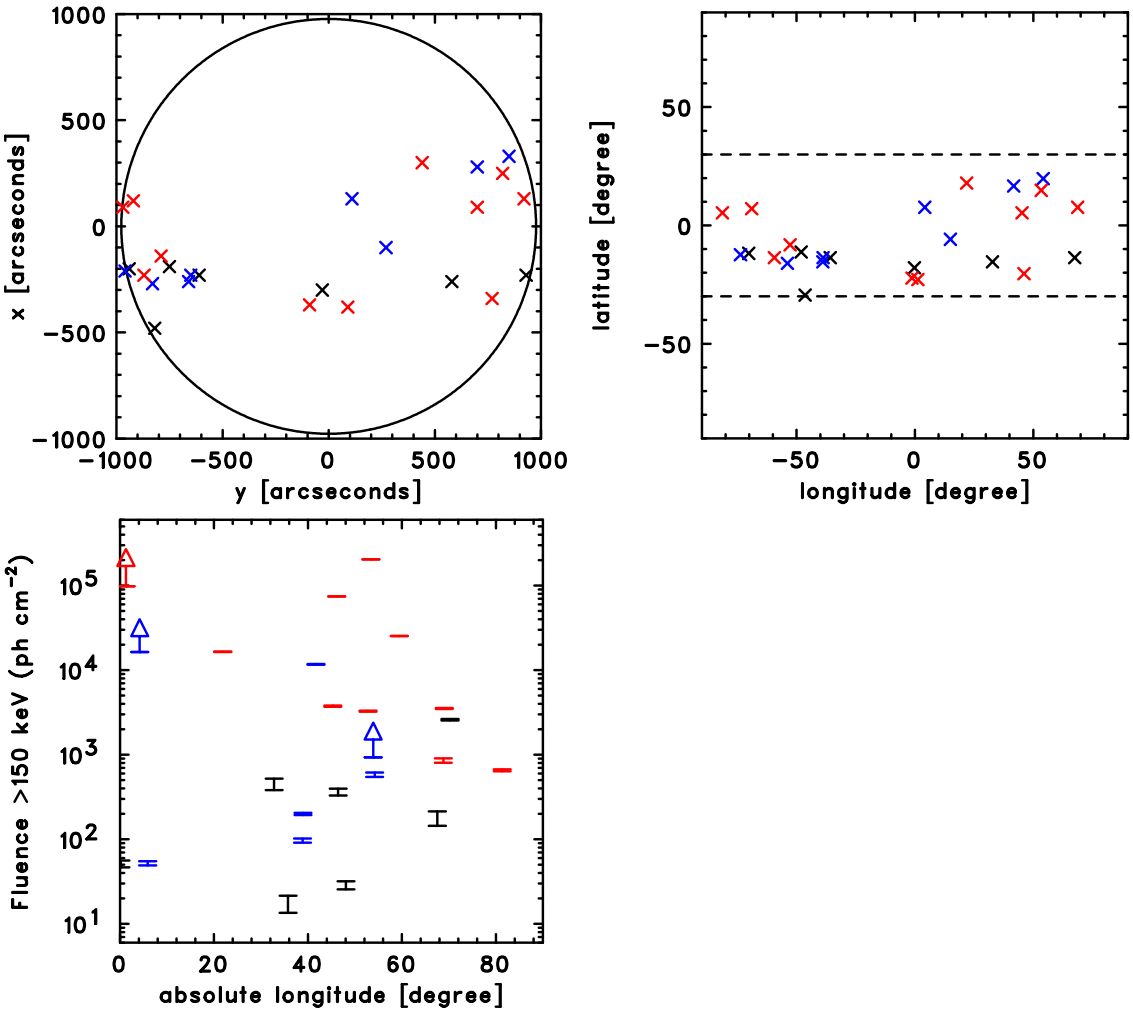

Figure 4.2 Spatial distribution of the γ-ray flares in Table 4.1. *Top left*: Position distribution on the solar disk. *Top right*: Distribution in latitude and longitude. The dashed lines shows $\pm 30°$. *Bottom left*: Fluence >150 keV vs absolute longitude. Colored points indicates as same as Fig. 4.1. Events for which only lower limits of the total fluence are available are marked by arrows.

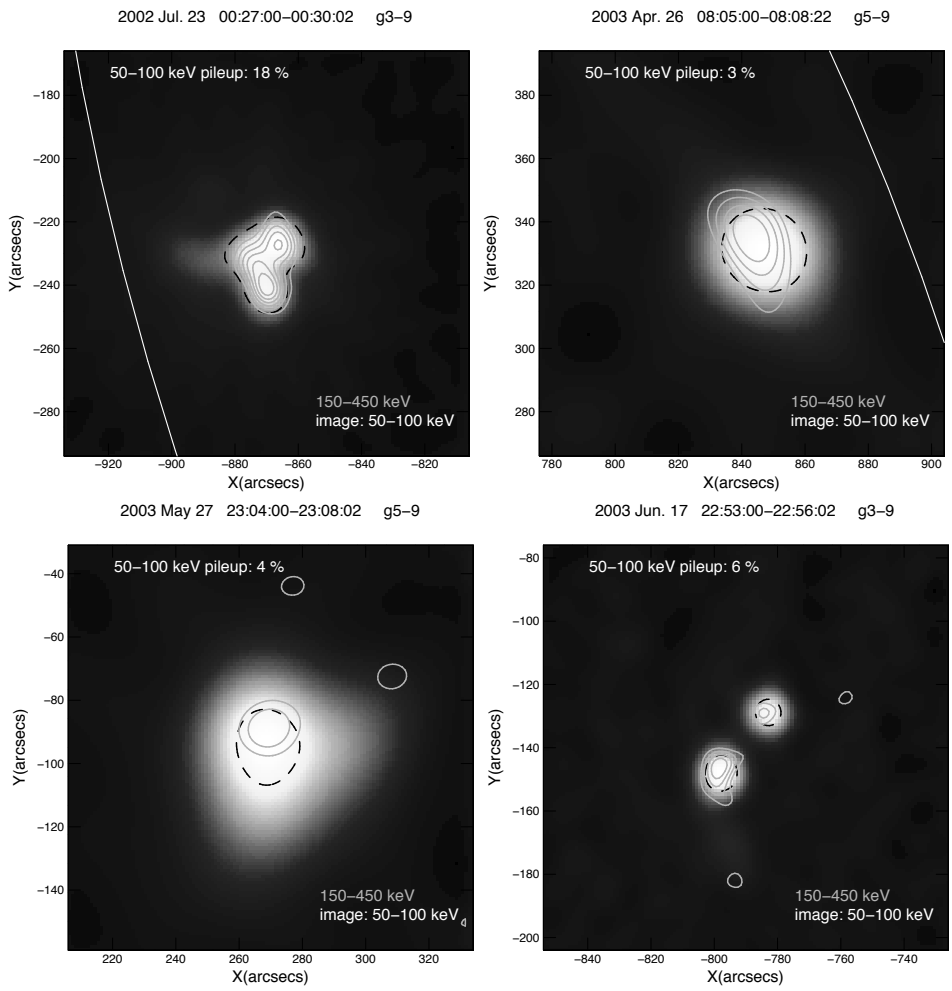

Figure 4.3 150-450 keV contours (cyan) over 50-100 keV images of events that successfully imaged in 150-450 keV. The contour levels of 90% and 80% are shown, and 70%, 60%, 50% and/or 40% are shown if the statistics are enough. For comparison, the black dashed contour shows the 50-100 keV image at the lowest percentage level used for the 150-450 keV contour plot. The subcollimators used are given in the title of each plot (the same subcollimators are used for both energy ranges).

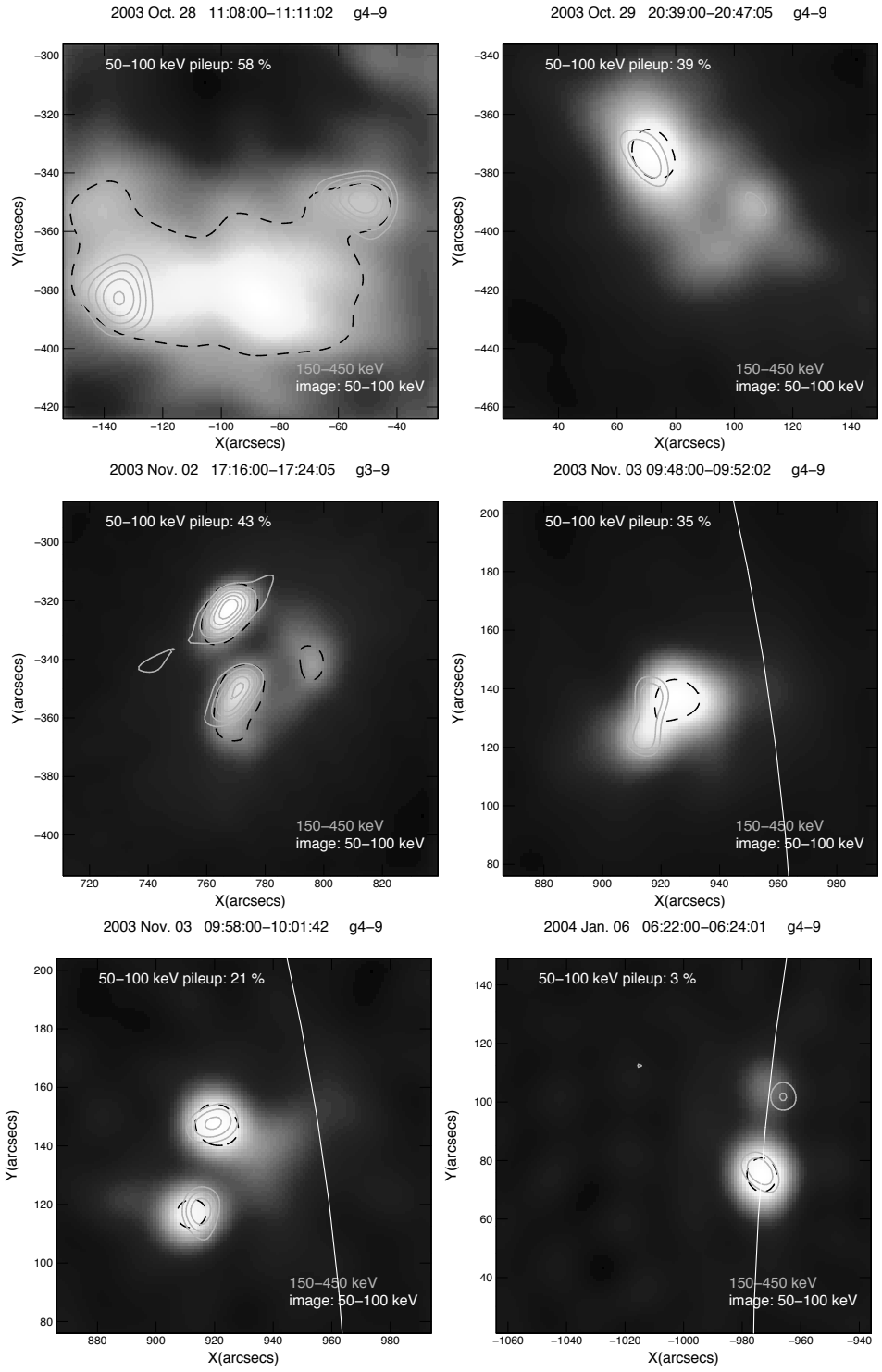

Figure 4.3 *Continued.*

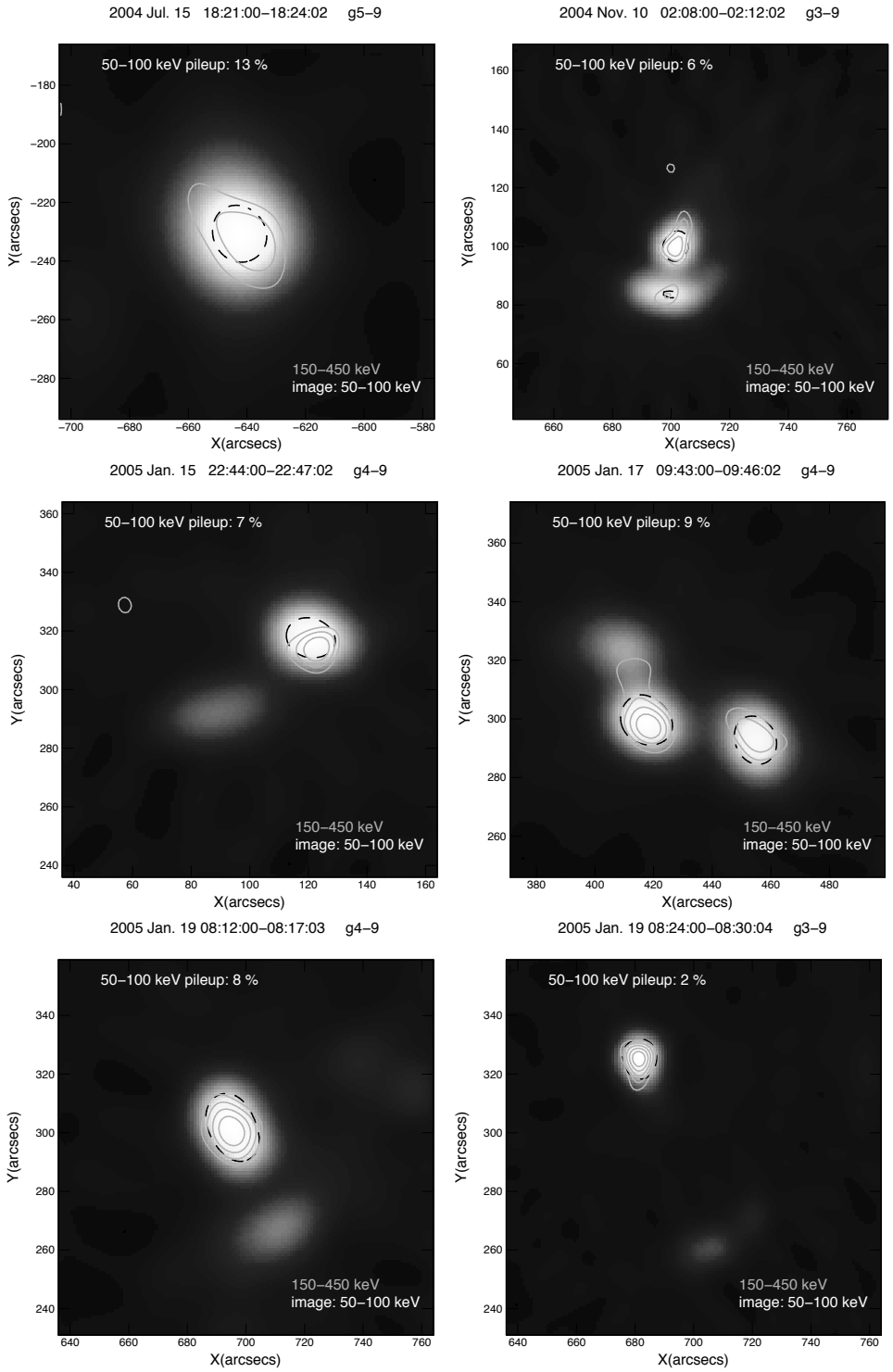

Figure 4.3 *Continued.*

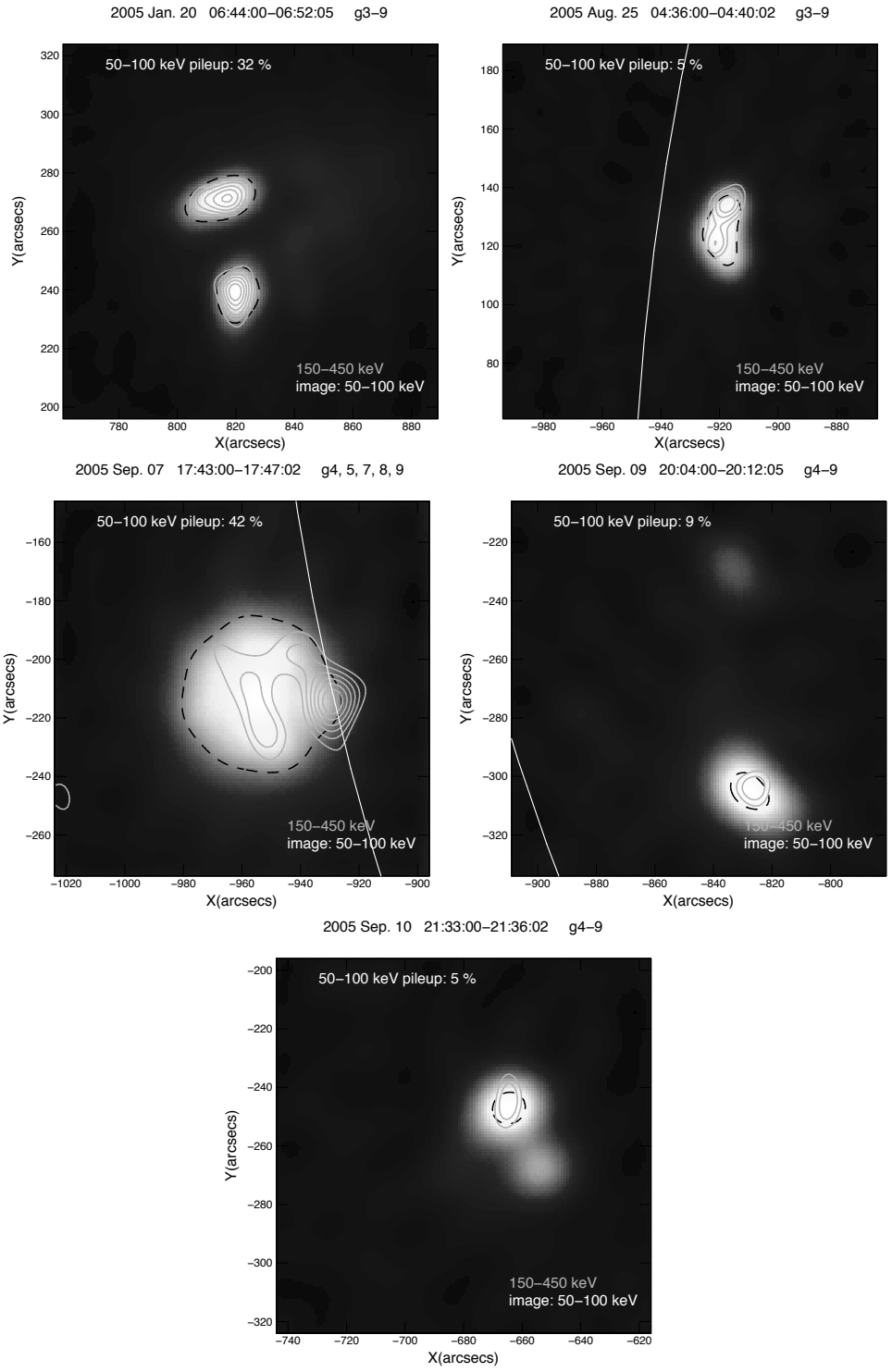

Figure 4.3 *Continued.*

thermal photons produce an image at the location of the thermal source at double the energy. Since the 50-100 keV energy range is generally dominated by non-thermal footpoint emissions from the chromosphere without any thermal contribution, pile-up effect can produce a spurious coronal source. This is most clearly seen in the 2003 October 28 event with the enormous pile-up fraction of 58% (we note that our simple pile-up estimate is likely failing for this extremely high count rate) where the 50-100 keV emission shows an extended coronal source, while the rear image shows mostly footpoint emission. A spurious coronal source is also visible in the 2003 November 2 and 3 event. In the 2005 September 7 event with 43% pile-up, a coronal HXR source is imaged with both front and rear segment data, suggesting that only part of the coronal emission at 50-100 keV is produced by pile-up.

4.4 Ratio of footpoint intensities

To investigate spectral differences of the two footpoints, we calculated fluxes of each footpoint in two energy bands (50-100 keV and 150-450 keV). Previous studies of spectral differences in hard X-ray spectral indices below 100 keV showed that spectral differences are frequently observed. However, the differences are generally small, with the spectral index differing by less than 0.6 (Emslie et al. 2003, Saint-Hilaire et al. 2008). While Emslie et al. (2003) suggested that the difference in column density in the two legs of the flare loop could produce the difference in spectral slope, Saint-Hilaire et al. (2008) noted that significant coronal hard X-ray emission would be produced in such a case, excluding different column densities as an explanation for most events. Other explanations of the asymmetry in the footpoint spectra involve asymmetrical acceleration, non-uniform target ionization, and magnetic mirroring (see Saint-Hilaire et al. 2008 for discussion).

In the following, we check if the asymmetry holds also for spectra above 100 keV. We define the footpoint with higher flux in 50-100 keV as "footpoint 1", and the weaker footpoint as "footpoint 2", and compute the flux ratio of "footpoint 2" to "footpoint 1". Flux ratios of 50-100 keV and 150-450 keV are plotted in the left panel of Fig. 4.4. The absence of ratios smaller than 0.2 reflects the limited dynamic range.

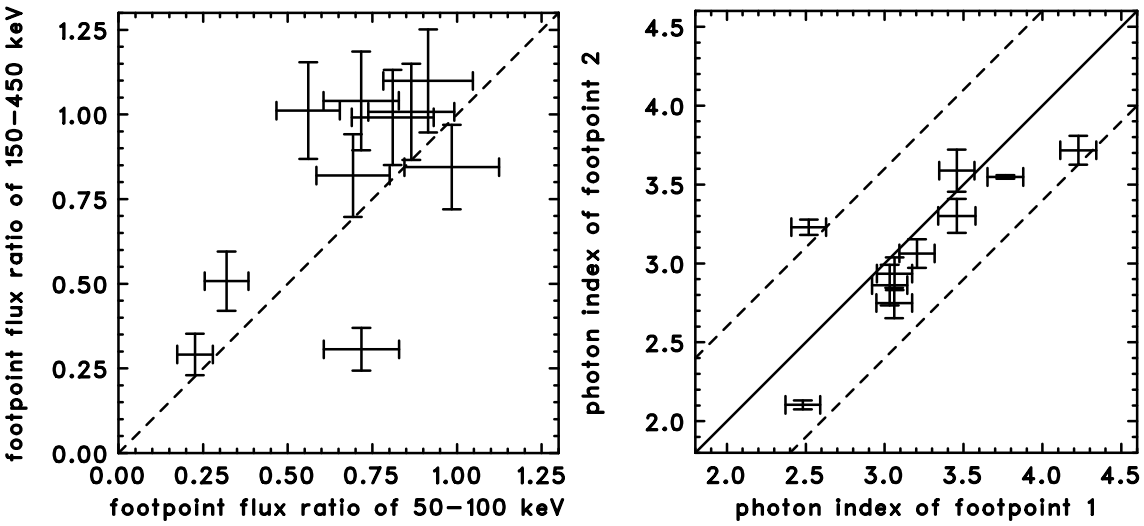

Figure 4.4 *Left*: Correlation of the footpoint flux ratios at 50-100 keV and 150-450 keV. *Right*: Correlation of the photon spectral index of each footpoint. The dashed line corresponds to a spectral difference of 0.6.

Nevertheless, the footpoint ratios below and above 100 keV are roughly proportional. In the right panel of Fig. 4.4, the power-law indices of each footpoint are plotted. Most of the events show similar spectra for both footpoints, with a tendency that the stronger footpoint has a slightly softer spectrum (8 out of the 10 events). However, the difference derived from the 8 events with a softer spectrum is only 1.9 σ. Previous studies do not report such a correlation (Sakao et al. 1996, Saint-Hilaire et al. 2008). Besides that, the results regarding the footpoint asymmetry are similar to what has been found at lower energies (Emslie et al. 2003, Saint-Hilaire et al. 2008), and it indicates that relativistic electrons penetrate at both footpoints at similar rates.

For the 7 events that occurred near disc center (see Table 4.1), we estimated the magnetic field strength at the two footpoints using *SOHO*/MDI magnetograms (Scherrer et al. 1995). In 4 out of the 7 events, the footpoints with higher fluxes in the 50-450 keV band have higher magnetic field strength. The brighter footpoints have lower magnetic fields in the remaining 3 events. Hence, there is no significant correlation within this limited number of events. To further investigate the relation between hard X-ray intensity and magnetic field strength, a larger sample of event

should be considered including the much more numerous events seen at lower energies.

4.5 Separation of footpoints

Stochastic acceleration models of impulsive flares predict that the fractions of accelerated protons and electrons are determined by the size scale of the acceleration region (Miller 2000). In Emslie et al. (2004), a relation between a scale length of acceleration and acceleration rates of electrons and protons is derived. Assuming a constant acceleration volume of 10^{27} cm^3, the proton acceleration rate increases for spatial scale increasing from 10^8 to 10^9 cm, while the electron acceleration rate decreases. *RHESSI* observations of the 2003 October 28 flare show that electron and proton acceleration occur on flare loops of similar size that are spatially displaced by $\sim(12\pm4) \times 10^8$ cm (Hurford et al. 2006). Here we investigate if the relative acceleration efficiency of electrons and protons depends on the length of the flare loop. We use the ratio of the 2.2 MeV fluence to the >300 keV fluence as a measure of the proton to electron acceleration efficiency. Furthermore, we assume that the flare loop length scales in the same way as the length of the acceleration region (see Emslie et al. 2004 for a detailed description) and we approximate the flare loop length by the footpoint separation. To avoid problems with spurious sources produced by pile-up, we use the rear segments for the largest events to determine the footpoint separation. For smaller events where pile-up effects are negligible, we calculate footpoint separations by using data from front segments. Fig. 4.5 shows the footpoint separation against the >300 keV fluences (left) and the fluence ratio of 2.2 MeV to >300 keV. The values of the fluences are taken from Shih et al. (2009). No obvious correlation is found in Fig.4.5. The only notable fact is that the event with the largest footpoint separation (2003 October 28) is the event with the highest ratio.

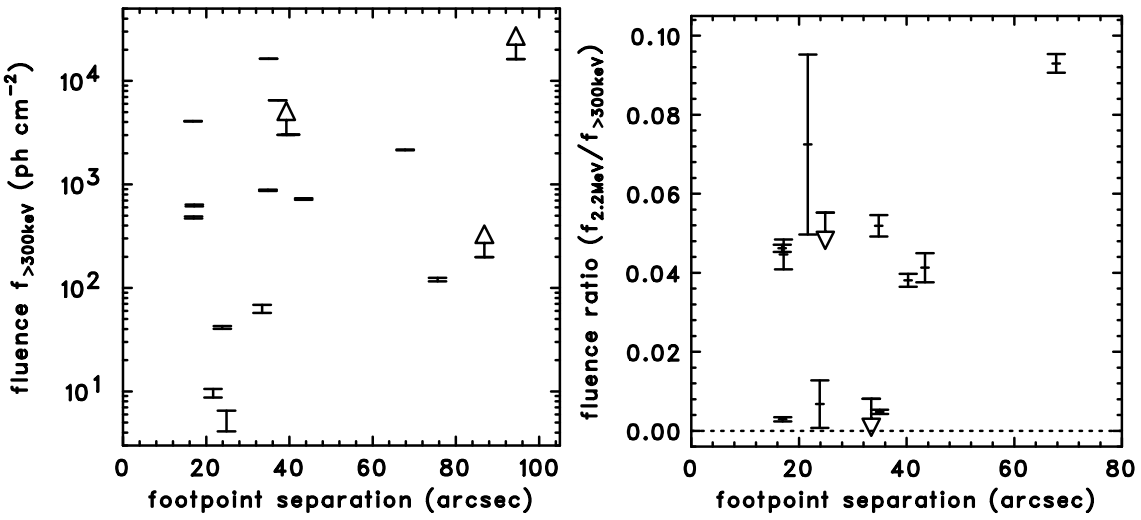

Figure 4.5 *Left*: Fluence >300 keV vs footpoint separation. *Right*: Fluence ratio of 2.2 MeV and >300 keV vs footpoint separation. Fluences are from Shih et al. (2009) and arrows mark again lower and upper limits.

4.6 Coronal γ-ray sources

Coronal γ-ray bremsstrahlung sources are reported for the three *RHESSI* γ-ray flares with the best counting statistics (Krucker et al. 2008a). These sources are best visible in the impulsive phase of the flare during the decay of the non-thermal hard X-ray emission. The observed coronal emission decays more slowly and has a harder spectrum than the footpoint emission, making it easier to detect these sources after the hard X-ray peak time. We checked the entire sample of our events for coronal emissions, in particular during the decay phase of the hard X-ray peak. However, no further event with a coronal γ-ray bremmstrahlung source has been found. For most of the events this can be attributed to low counting statistics. The only candidates with relatively good counting statistics, but without a detectable coronal source >150 keV, are the events of 2002 July 23 and 2003 November 2. However, these two events also have about three times fewer >150 keV counts than the 2005 January 20 flare discussed in Krucker et al. (2008a). Furthermore, these two events are rather compact compared to the 2005 January 20 flare, where the footpoints and the coronal γ-ray

source are separated by $\sim 40''$, making it difficult to image a coronal contribution. Hence, the absence of any further examples of coronal γ-ray bremsstrahlung sources is probably due to observational limitations.

Chapter 5

HXR Imaging and Spectroscopy of Above-the-loop-top and Footpoint Sources in a Limb Event*

5.1 Coronal above-the-loop-top HXR source

Since magnetic reconnection occurs above the flare loop top, the coronal HXR sources seen above the loop top provide important diagnostics of particle acceleration in solar flares. While the acceleration mechanism is not known, it is well accepted that a magnetic reconnection process converts magnetic energy into kinetic energy. Coronal sources are generally much fainter than footpoint sources, and almost always present as well (e.g., Krucker & Lin 2008, and also described in the review by Krucker et al. 2008b). Among these, coronal sources seen significantly above the loop top are rarely observed. In Chapter 4, we were unable to find the coronal γ-ray source except for those already known in the biggest *RHESSI* flares. It is of great interest

* The updated content of this section is published by ApJ, Vol. 737, article id. 48, 2011, entitled "On the Relation of Above-the-loop and Footpoint Hard X-Ray Sources in Solar Flares" by S. Ishikawa, S. Krucker, T. Takahashi and R. P. Lin.

to study coronal above-the-loop-top sources without a γ-ray emission, in particular using *RHESSI*'s imaging spectroscopy capabilities, to improve the understanding of particle acceleration in solar flares.

As described in Chapter 2, an above-the-loop-top source is clearly observed in the Masuda flare (Masuda et al. 1994) by *Yohkoh*/HXT, which is thought to represent evidence of magnetic reconnection in solar flares, and the particle acceleration above the flare loop top. However, since *Yohkoh*/HXT has only four energy bands in the 15-93 keV range, it is difficult to discuss the spectral structure of the sources. The above-the-loop-top source in the Masuda flare is compact (3-7 Mm), and no SXR emissions above the flare loop are seen, which suggests low thermal density in this region.

A *RHESSI* observation of an impulsive above-the-loop-top HXR emission on December 31, 2007 was reported by Krucker et al. (2010). The spectrum is well represented by a single component power-law with a photon index of $\sim$4.2. In this event, the pre-flare density is estimated from the pre-flare thermal emission, giving rather low densities in the order of $< 8 \times 10^9$ cm^{-9}. To produce the observed HXR emission, this requires the large number of non-thermal electrons such as $> 5 \times 10^{35}$ above 16 keV, which is the same order of magnitude as ambient electrons. Even with the thin-target assumption, the ambient thermal electrons will be super hot (such as $\sim$100 MK) by collisions within seconds. However, no such high-temperature emission is detected. Therefore, Krucker et al. (2010) suggest that the ambient thermal electrons are not present in the above-the-loop-top region, and that all electrons in the region are accelerated (all see the similar discussion in Section 6.2), which implies that the above-the-loop-top region is the acceleration region itself.

The rare observations of above-the-loop-top HXR sources indicate that probably this scenario cannot be applied to all flares. As in other scenarios, there are ideas such as particle acceleration in footpoints with the energy transported by Alfvén waves (e.g., Fletcher & Hudson 2008), and particle re-acceleration in footpoints (e.g., Brown et al. 2009; Turkmani & Brown 2010).

In this chapter, we describe the best example from the *RHESSI* database that resembles the Masuda flare geometry and show detailed imaging and spectroscopy of

this event.

5.2 Overview of the October 22, 2003 Flare

In the NOAA Active Region (AR) 10486, in which the two events are analyzed in Chapter 4 occurred, a flare event over the solar limb at (−950 arcseconds, −300 arcseconds) was detected by *RHESSI* on October 22, 2003 (SOL2003-10-22T20:07). HXRs up to ∼150 keV are detected in the front detectors. The *GOES* SXR event started at 19:47:00 UT, and ended at 20:28:00 UT. The soft X-ray peak time was 20:07:00 UT, and the *GOES* class was M9.9. There were no observations from *TRACE*, but a 12 minute cadence EUV observations from the Extreme-Ultraviolet Imaging Telescope (EIT, Delaboudinière et al. 1995) onboard *SOHO* (Domingo et al. 1995). 195 Å EUV images from EIT show a thermal component with relatively lower temperatures such as ∼MK. There are no radio nor optical observations of this flare.

Time profiles of *GOES* and *RHESSI* observations are plotted in Fig.5.1. *RHESSI* started the observation at 19:54:52 UT with the attenuator state A1 and the decimation state FD1. The flare had already started before *RHESSI* commenced observation, when the *RHESSI* spacecraft was in the night. The state changed to A0 and FD3 at 19:55:12 UT, to A1 and FD1 at 19:55:40 UT, to A3 and FD1 at 19:56:15 UT.

As shown in the 40-80 keV light curve, this event has four HXR peaks (shown in Fig. 5.1 as orange boxes); three peaks during the SXR rise, and one peak a few minutes after that of the SXR. The typical FWHM duration of each peak was a few tens of seconds. By comparing with the SXR time profile, we presume that HXRs were already emitted before the start of the *RHESSI* observation. In the following discussions, these four peaks are denoted as peaks 1 to 4. Data before 19:56:15 UT are used for analyzing peak 1 (A1 state), but the problem of pile-up hampers the analysis of peak 1. By first order estimation, 46% of the counts above 30 keV are due to pile-up during peak 1. All other peaks are in A3, and pile-up is not a problem. Conversely, in the A3 state, there is uncertainties in fluxes below ∼12 keV because of the effect of the attenuator, hence we used >15 keV for the spectroscopy.

The lightcurves at several energy bands of <40 keV and the 150-450 keV band

are shown in Fig. 5.2. The thermal emission in the flare loop is dominant above ∼30 keV in this flare (details in Section 5.5). Therefore the lightcurves at 12-15 keV, 15-20 keV and 20-30 keV are on the thermal component, while the 30-40 keV band is marginal. Unfortunately, in the 150-450 keV lightcurve obtained by the rear segments, no significant signal is seen. Hence, we conclude that the rear detectors did not detect any significant signal from this flare.

Figure 5.3 is the enlarged 40-80 keV light curve of the first three peaks. By fitting, the e-folding decay times of peaks 2 and 3 are obtained to be ∼60 s. These time scales are based on the total emissions from the whole flare. A time profile of each spatial component is discussed in Section 5.7.

5.3 Imaging analysis

Images during the four peaks at 35-100 keV obtained by *RHESSI* are shown in Fig. 5.4. As spectra shown in the next section, emissions above ∼35 keV are thought to be almost non-thermal emissions (details are discussed in Section 5.5). Time intervals of 19:55:50-19:56:14, 19:56:30-19:57:22, 19:57:30-19:58:51, and 20:10:10-20:11:27 (UT) are used for the analysis. The MEM image reconstruction method is used due to sufficient counts in the energy band to obtain better images, and contours of 25, 37.5, 50, 62.5, 75 and 87.5% are plotted. A HXR source in the corona above the limb around ∼(−960, −290) is clearly seen for all peaks, except peak 4. The absence of coronal source in the peak 4 image indicates that the coronal emission is at least ∼10 times (corresponding to the dynamic range of *RHESSI*) fainter than the footpoint. The coronal source is seen at almost the same position during peaks 2 and 3 and is rather compact, the size of the coronal source of peak 3 is estimated as ∼11 Mm for length along the limb and ∼6 Mm for width, using the MEM image with g4-9 (e.g., Dennis & Pernak 2009). Conversely, the width of the footpoint source along the limb in the peak 3 is estimated at 3.5 Mm, using the same MEM image. The emission from the corona of peak 1 is detected at almost the same position as the thermal source, and would be from the pile-up of thermal SXR emissions. Therefore, it is not clear whether the coronal non-thermal HXR in peak 1 is surely detected, or only due

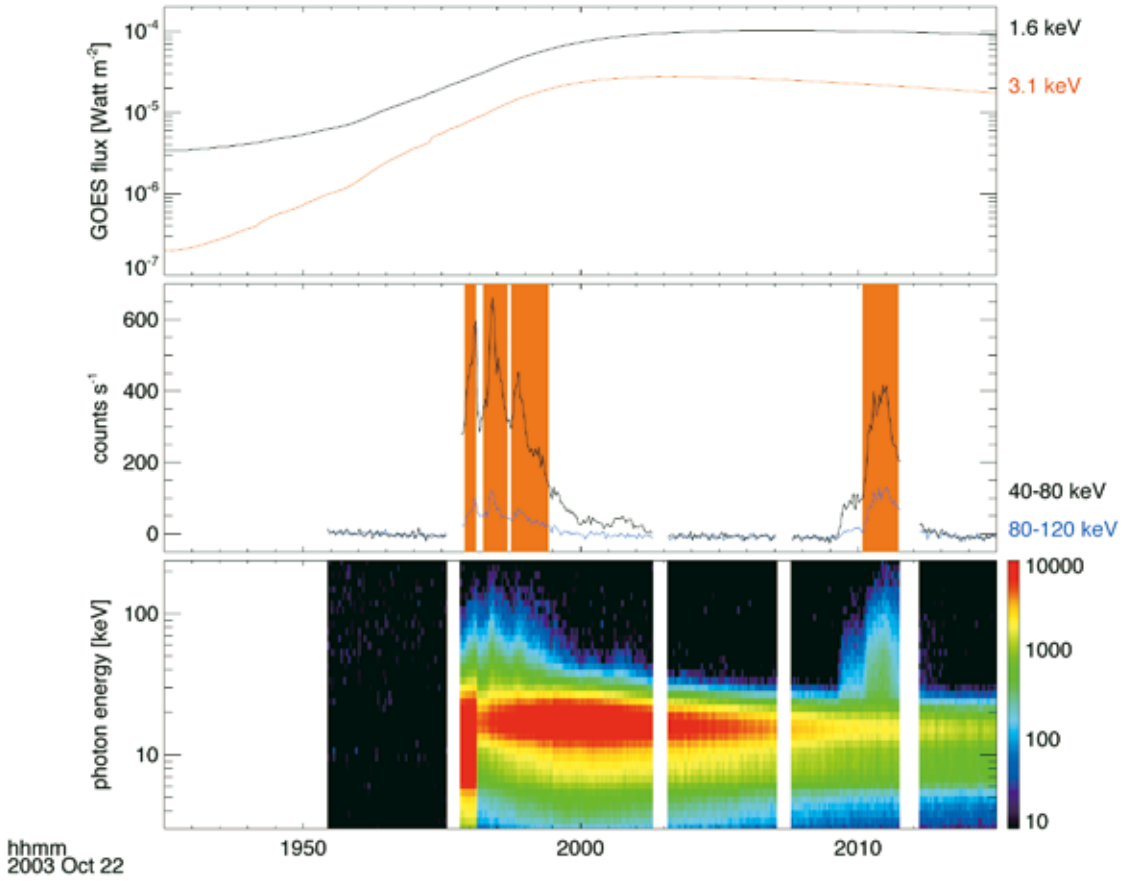

Figure 5.1 Time profiles of the October 22, 2003 flare. *Top*: *GOES* SXR light curves. *Middle and bottom*: *RHESSI* HXR time profiles. The four HXR peaks are marked in orange.

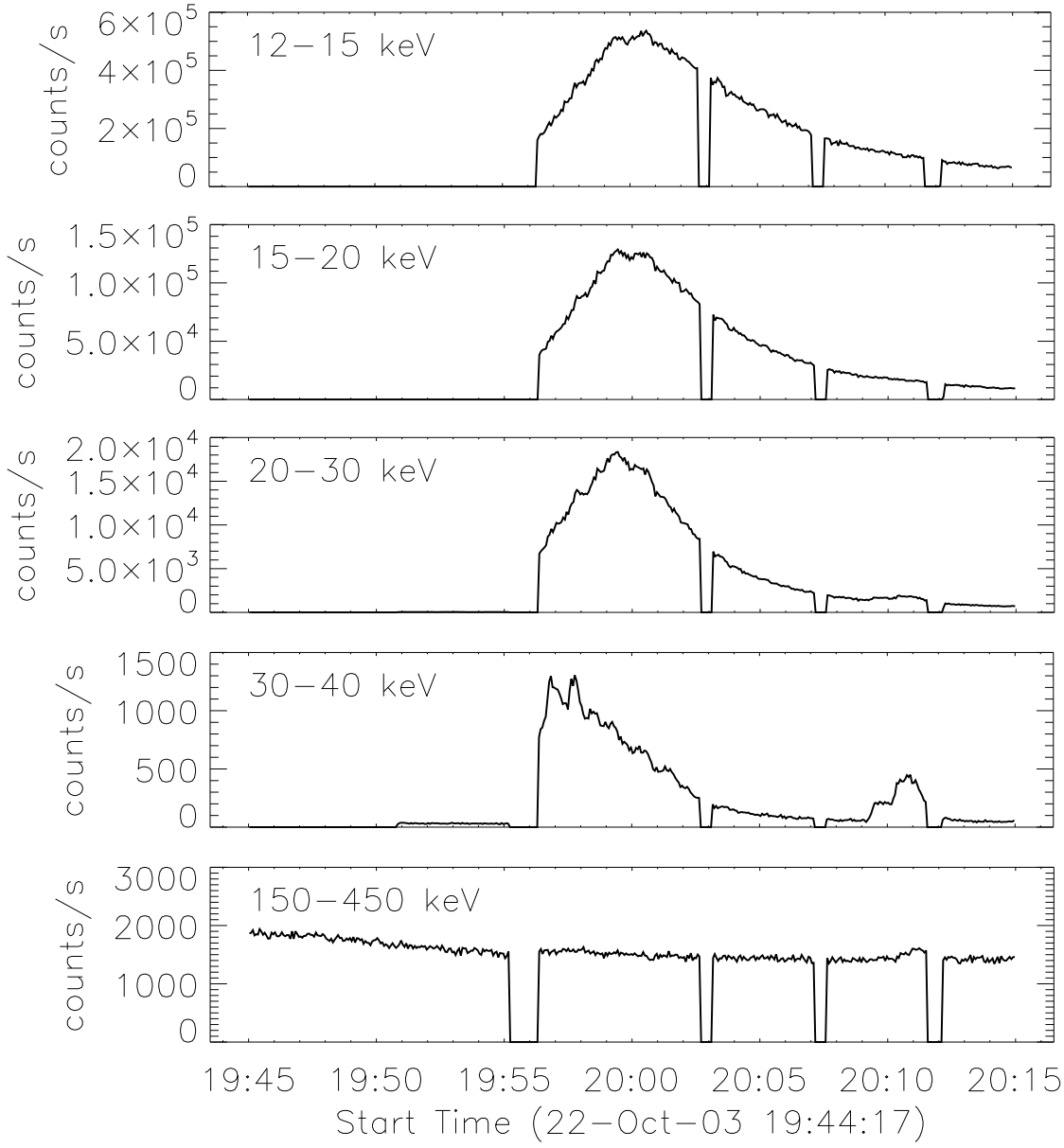

Figure 5.2 Lightcurves of <40 keV energy bands and > 150 keV of the October 22, 2003 flare. The energy bands are 12-15 keV, 15-20 keV, 20-30 keV, 30-40 keV (with the front segments), and 150-450 keV (with the rear segments). Only the data with the A3 attenuator state is plotted.

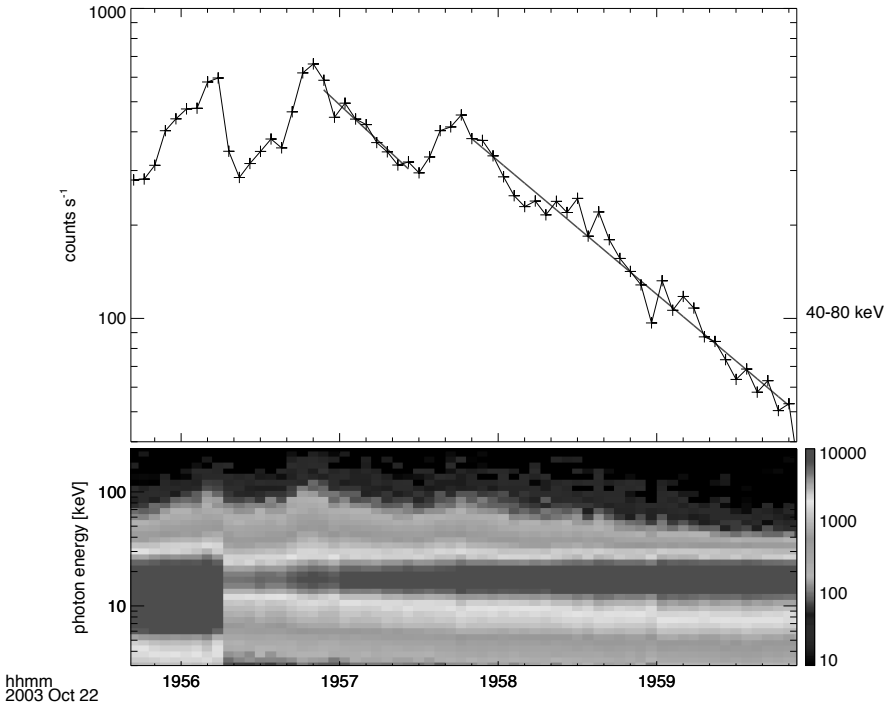

Figure 5.3 Enlarged 40-80 keV light curve of three peaks. The decay time scale of $\sim$60 s are obtained by fitting peak 2 and 3.

to the pile-up.

For all peaks, only one footpoint is visible, strongly suggesting that other footpoint sources are occulted. While a footpoint at $\sim(-935, -245)$ appears in the images of peaks 1 and 2, a completely different footpoint at $\sim(-915, -310)$ is seen during peaks 3 and 4. This is attributed to footpoint motion (e.g., Yang et al. 2009) and/or the abrupt change of position of HXR footpoint emissions (e.g., Krucker et al. 2003). By these effects, one footpoint may have become to be occulted over the limb, and the other footpoint appeared. Peaks 1 and 2 show footpoint emissions from the northern flare ribbon, while peaks 3 and 4 show emissions from the southern ribbon.

In Fig. 5.5, 35-100 keV contours over the images of the thermal flare loop in 9-12 keV and 12-15 keV of peak 3 are shown. This image shows that the coronal source is above the thermal loop top, similar as in the Masuda Flare (Masuda et al. 1994). The footpoint is also shown at 35-100 keV relative to the thermal loop seen at 9-12 keV and 12-15 keV in peak 3. While the second footpoint associated with this thermal loop should exist below the north leg of the loop, there is no detection in that position. Two footpoints with similar intensities are mostly observed (e.g., Saint-Hilaire et al. 2008), hence the second footpoint is likely occulted by the solar disk.

The plots in Fig. 5.6 show contours of 12-15 keV and 35-100 keV on a 195 Å EUV image by *SOHO*/EIT. The *RHESSI* data used in these images are from peaks 1 through 4. The EIT images are obtained every 12 minutes, and the image at 20:00:11 UT are shown with the contours of peaks 1 through 3, $\sim$70 s after the end of peak 3. No significant structure is seen in the EIT image at 19:48:12 UT, around the *GOES* start time. The EIT image with peak 4 is at 20:12:10 UT, about $\sim$30 s after the end of peak 4. The main thermal HXR loop is also seen in EUV. The EIT image matches the *RHESSI* 12-15 keV images of all four peaks in Fig. 5.6. A much fainter 12-15 keV emission appears to the north of the main flare loop around $\sim(-960, -260)$ in the image of peak 1, and matches the EIT image. This emission is also seen in Fig. 5.5, most clearly in the energy range below 12 keV. Therefore, this source could be the other flare loop in this flare arcade with a lower temperature. The EUV emission extended to the northern footpoint in the HXR peaks 1 and 2, meaning this part of

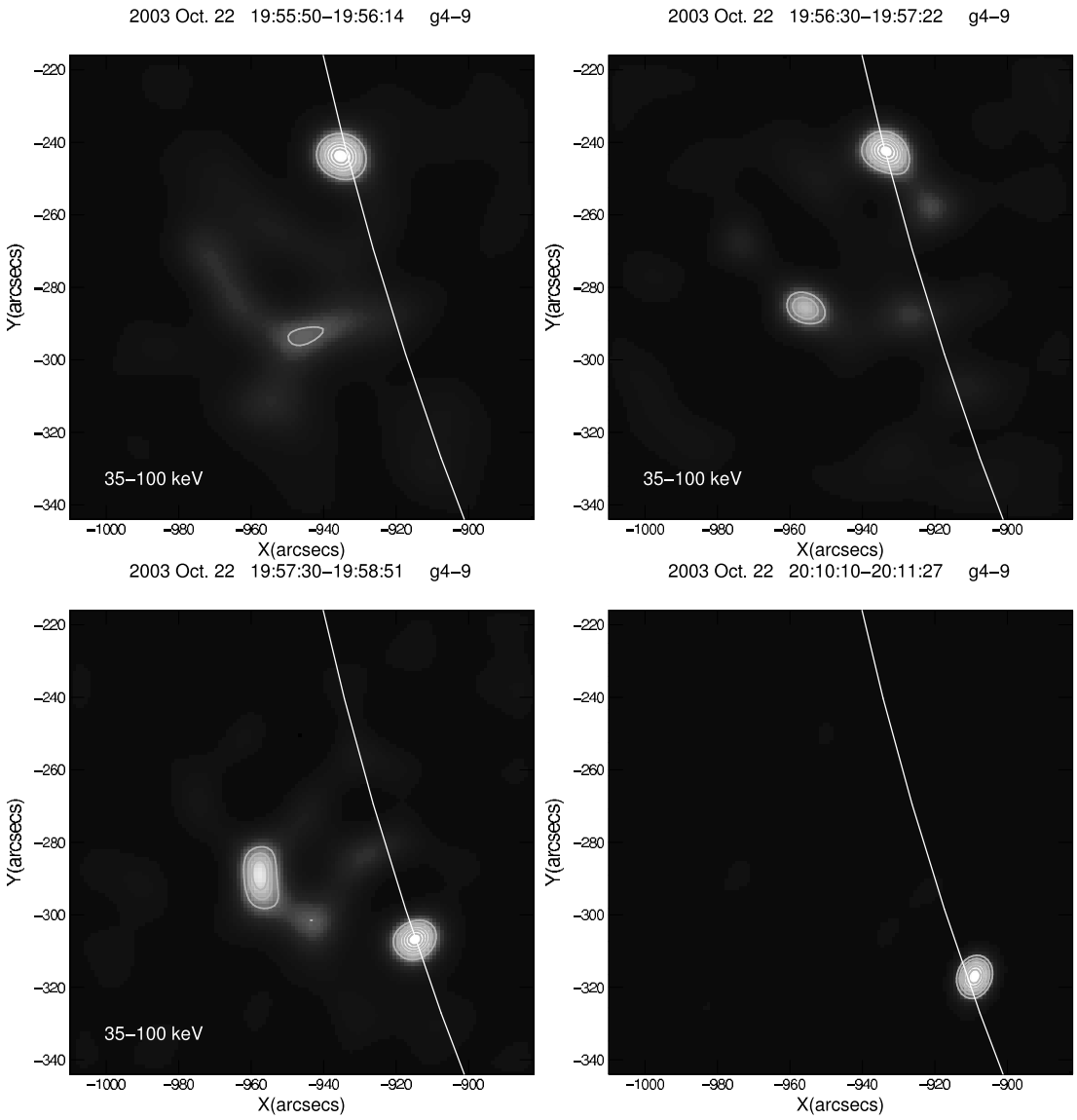

Figure 5.4 35-100 keV non-thermal images of the four peaks. MEM is used for reconstructing images.

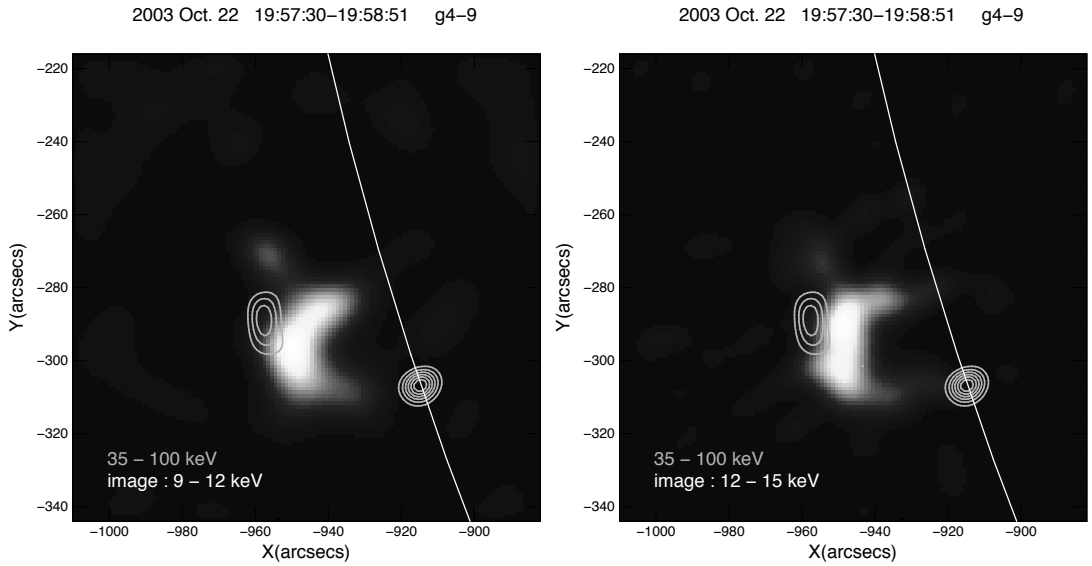

Figure 5.5 Image of 9-12 keV (left) and 12-15 keV (right) thermal emission from the magnetic loop of peak 3 with contours of 35-100 keV non-thermal emission from loop top and the footpoint. MEM is used for reconstructing images.

the arcade may be associated with peaks 1 and 2.

5.4 Thermal flare loop

The spatial scale of the thermal loop is estimated by the distance of the footpoints of the loop, at ∼20 Mm. The size of the bright region of the thermal loop is estimated to be ∼17 Mm long along the loop and ∼8 Mm wide, from the peak 3 image of Fig. 5.5. Assuming the depth of the thermal loop to be equivalent to the width, the volume of thermal source V_{th} is estimated as

$$V_{th} \sim (17\ \mathrm{Mm}) \times (8\ \mathrm{Mm})^2 = 1.1 \times 10^{27}\ \mathrm{cm}^{-3}. \tag{5.1}$$

In peak 4, the structure of the thermal source seems to be changed from peaks 1 through 3. The thermal source seen in peak 4 is relatively large; the volume V_{th4} is calculated as

$$V_{th4} \sim (15\ \mathrm{Mm}) \times (13\ \mathrm{Mm})^2 = 2.7 \times 10^{27}\ \mathrm{cm}^{-3}. \tag{5.2}$$

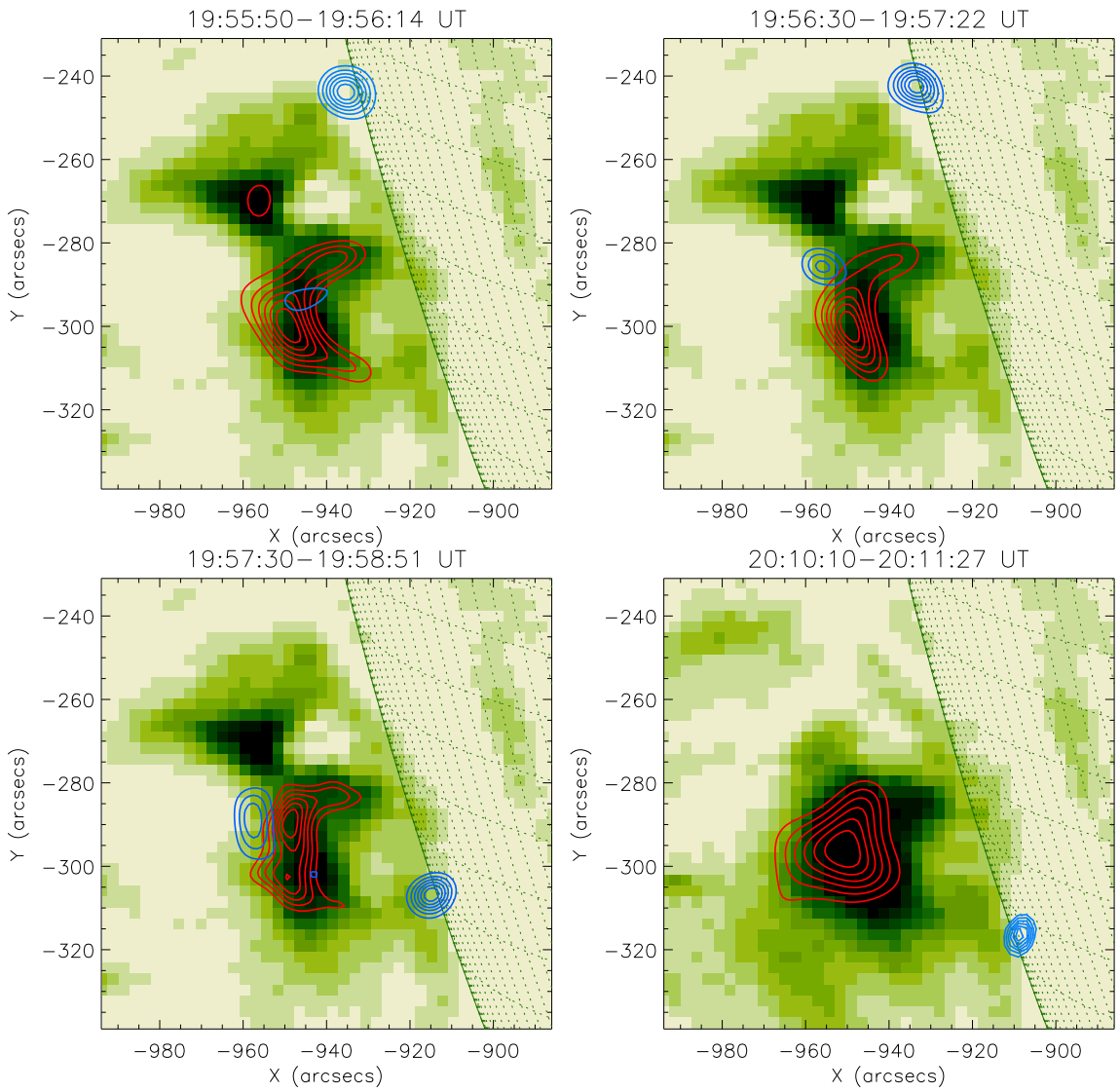

Figure 5.6 12-15 keV (red) and 35-100 keV (blue) HXR contours over *SOHO*/EIT EUV images. Contour levels are 25, 37.5, 50, 62.5, 75 and 87.5% for all contours. MEM is used for reconstructing images. The EIT images are at 20:00:11 UT with the peak 1 through 3 images, and at 20:12:10 UT with the peak 4 image.

	Temperature (MK)	Emission measure (cm^{-3})	Density* (cm^{-3})	Thermal Energy* (erg)
Peak1	32.3	2.1×10^{48}	4.4×10^{10}	3.1×10^{29}
Peak2	32.5	2.8×10^{48}	5.1×10^{10}	3.7×10^{29}
Peak3	32.6	4.7×10^{48}	6.6×10^{10}	4.8×10^{29}
Peak4	22.6	8.7×10^{48}	5.7×10^{10}	7.2×10^{29}

Table 5.1 Summary of properties of thermal emissions. (*) Uniform densities are assumed.

	Break energy E_{B1} (keV)	Photon index at $E_{B1} < E < E_{B2}$	Break energy E_{B2} (keV)	Photon index $> E_{B2}$
Peak1	26	4.5	44	3.6
Peak2	27	3.8	83	3.5
Peak3	26	4.2	79	3.1
Peak4	21	2.5	82	3.0

Table 5.2 Non-thermal parameters obtained by fitting. The fixed value of 1.5 are used for the photon index below the cut-off energy E_{B1}.

The HXR spectra of the four peaks are shown in Fig. 5.7. The black lines are the flare-integrated total spectra from the whole field of view with pile-up corrections. The spectra are well-fitted by combinations of the thermal bremsstrahlung model (the red curves) and broken power-law model (the blue lines). The thermal components originate from hot plasma filled in the main flare loop, with relatively high temperatures of ∼32-33 MK at peaks 1 through 3, and ∼23 MK at peak 4. The obtained temperatures and emission measures by fitting are shown in Table 5.1. The temperature and emission measure increase through the three HXR peaks during the SXR rise time. While the temperature decreases to ∼23 MK at peak 4, the emission measure at the peak 4 exceeds the first three peaks. The non-thermal parameters of the blue lines are listed in Table 5.2.

If we assume uniform density in the emitting region, the density of thermal elec-

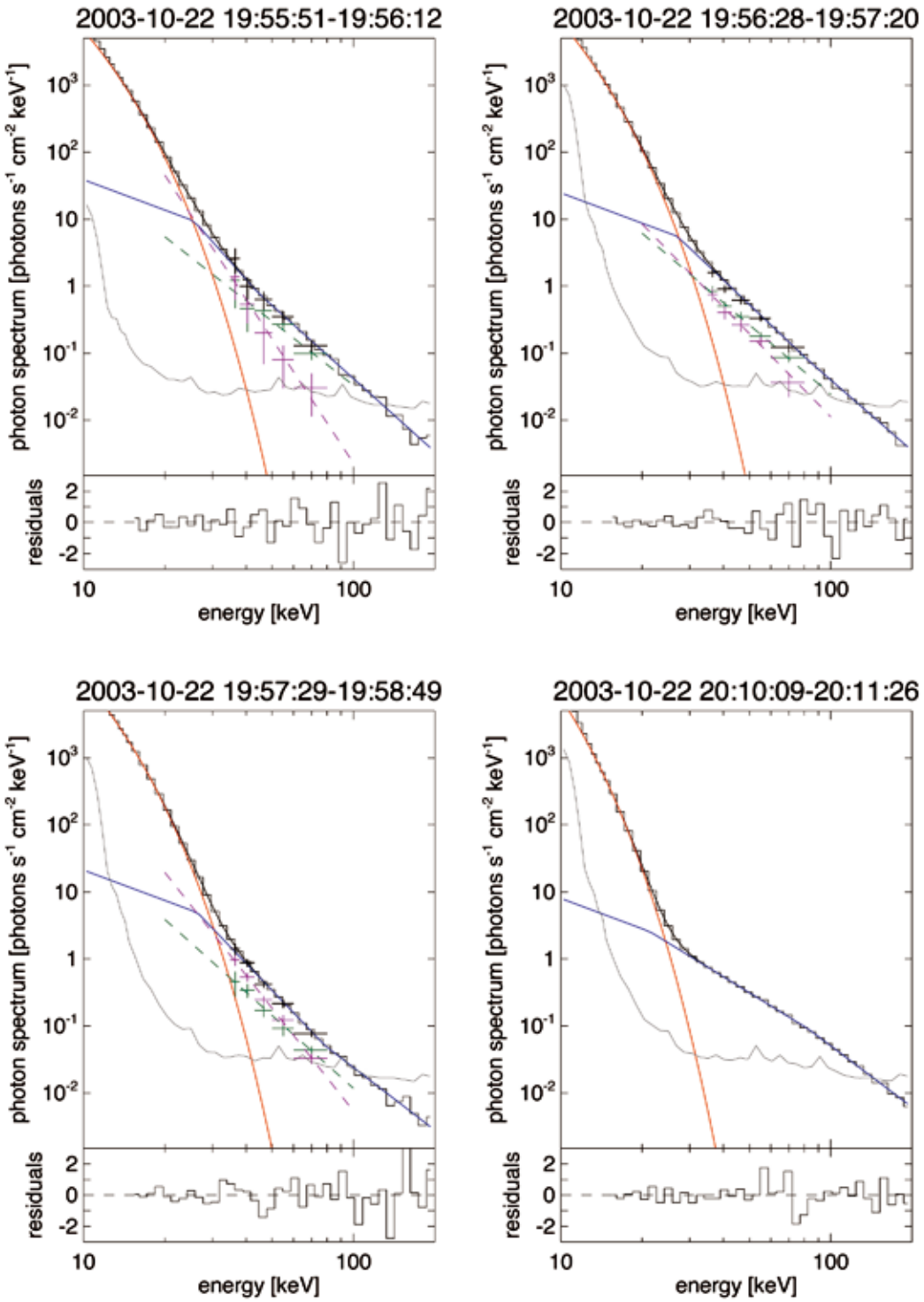

Figure 5.7 Spectra of four HXR peaks. The magenta plots are from coronal loop top emissions, and the green plots are from footpoint emissions (see text for details).

trons in the flare loop n_{th} can be calculated as follows:

$$EM = \int_{V\,th} n_{th}^2 dV \tag{5.3}$$

$$\sim n_{th}^2 V_{th} \tag{5.4}$$

$$n_{th} \sim \sqrt{\frac{EM}{V_{th}}}. \tag{5.5}$$

The thermal plasma has the Maxwell-Boltzmann distribution, and using the estimated density, the thermal energy of the electrons will be

$$E_{th} \sim \frac{3}{2} n_{th} kTV_{th}, \tag{5.6}$$

where k is the Boltzmann constant and T is the temperature. The estimated density and thermal energy for peaks 1 through 4 are shown in Table 5.1. The volume V_{th4} instead of V_{th} is used for the estimation for peak 4. The density and thermal energy increase peaks 1 through 3, while they decrease between peaks 3 and 4. The number of thermal electrons increases peaks 1 thorough 4, which is consistent with the chromospheric evaporation model.

5.5 Spectroscopy of high-energy components

To compare spectra of the coronal and footpoint sources, we made images of several energy bands and calculated fluxes of the coronal and footpoint sources for peaks 1, 2 and 3 (e.g., Krucker & Lin 2002). Figure 5.8 shows images of peak 3 at several energy bands. We made similar images for peaks 1 and 2 using the same method as for peak 3. The coronal source was found to be stronger at lower energies, and the footpoint source stronger at higher energies. Hence, in all three peaks, the footpoint sources have harder spectra than the coronal sources.

We calculated fluxes from the images and compared them to the flare-integrated spectrum in Fig. 5.7. The magenta data points show the spectra of the coronal sources, and the green points show the footpoint spectra. We note that while the footpoint emission shown in the spectra in peaks 1 and 2 is the northern footpoint, that of peaks 3 and 4 is the different, namely the southern footpoint. The error bars

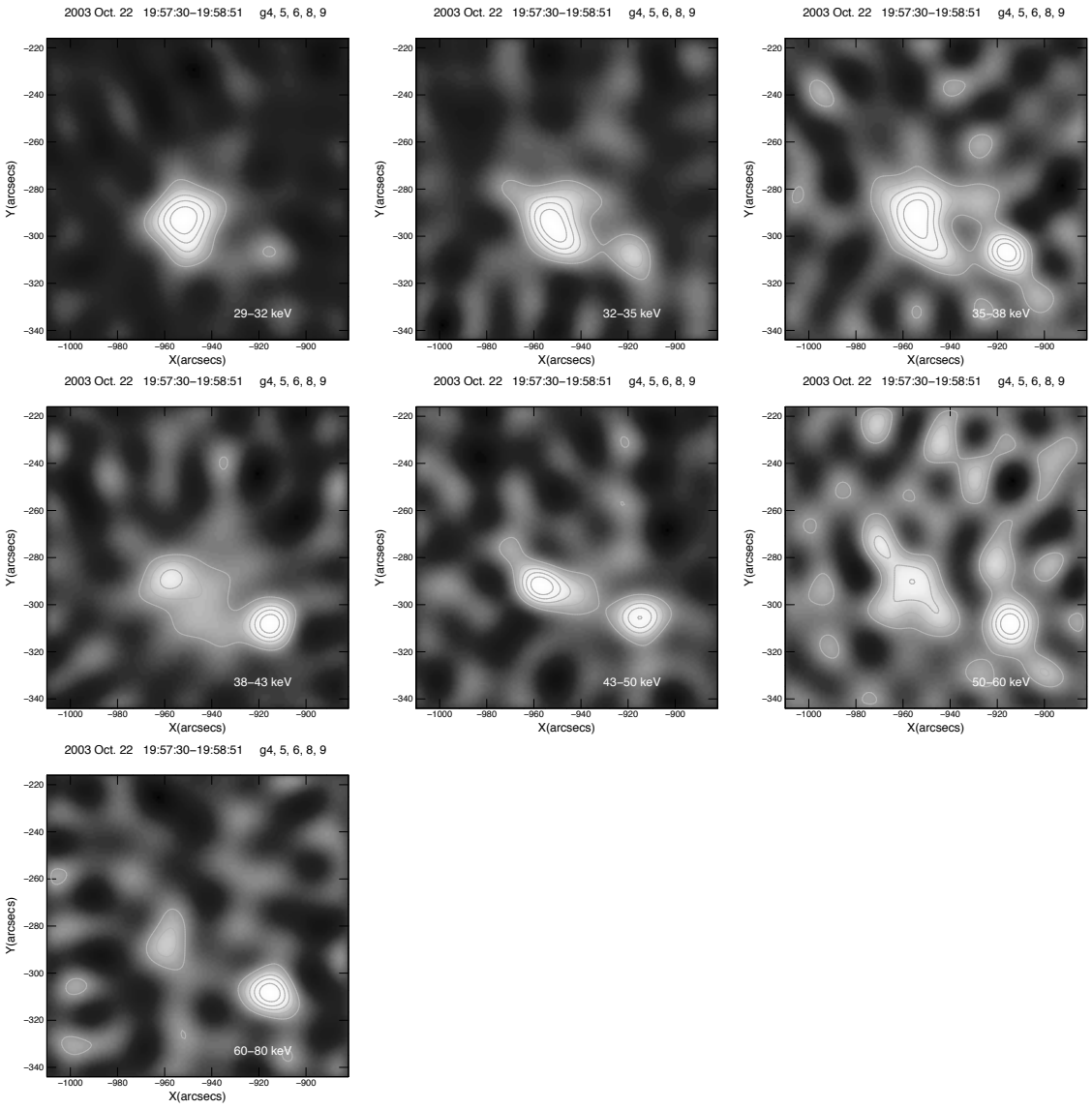

Figure 5.8 Images of various energy bands of peak 3.

are estimated based on the noise level. We roughly estimated the magnitude of noises, from the lowest to highest values, and from image regions containing no significant signal, and we regarded 1/3 of that value as $\sim \sigma$. Providing a noise is distributed completely at random in some range l, σ will be

$$\sigma = \sqrt{\int_{-l/2}^{l/2} x^2 dx} = \frac{l}{\sqrt{12}} = 0.287l. \tag{5.7}$$

Where noise of the *RHESSI* image could be distributed more than completely random to some extent, then we used the approximate value of 1/3. Although the errors estimated here have uncertainties, such uncertainties should be at least less than a factor of 2, even in the worst case. The similar estimation of errors are used by Saint-Hilaire et al. (2008). They use the highest flux value from image regions containing no significant signal multiplied by the fixed value of 1/6 as $\sim 1\sigma$. The other estimation method, in which errors are estimated by Gaussian fitting of the flux distribution from no signal regions, is shown by Mitani (2005). It is not known which method provides better estimation, since an estimation of fluxes in image regions is rather complex.

We fitted the coronal and footpoint spectra using energy bands from 35 to 80 keV. As a thermal component from the flare loops could be dominant below ∼35 keV, we ignored lower energies. Within the uncertainties, all the spectra are consistent with a single component power-law. The magenta and green lines are the result of fittings for the coronal and footpoint sources. The sum of fluxes from the two sources in each peak (Black points in Fig. 5.7) matched the total spectum, and the broken power-law shape of the total spectrum (steeper in lower energies, and harder in higher energies) could be interpreted as the superposition of two sources with different power-law slopes. The parameters obtained by fitting are listed in Table 5.3. Photon indices vary from ∼3.1 to ∼3.6 for the footpoints, and from ∼4.1 to 6.1 for the coronal sources. Relations between indices of the footpoint and coronal sources seems to be similar to the Masuda flare, in which the indices are ∼4.0 for the footpoints and ∼5.5 for the coronal source respectively (Masuda et al. 2000). Similar values for a set of 5 events are also reported by Battaglia & Benz (2006).

	Photon index	Flux at 30 keV (ph s^{-1} cm^{-2} keV^{-1})	Energy(FP=LT)* (keV)
Peak1			
Coronal source	6.1±0.9	3.8	41
Footpoint	3.1±0.5	1.5	
Peak2			
Coronal source	4.1±0.5	1.6	33
Footpoint	3.4±0.3	1.5	
Peak3			
Coronal source	5.1±0.3	2.5	59
Footpoint	3.6±0.4	0.9	
Peak4			
Footpoint	∼2.5	1.2	

Table 5.3 Summary of properties of non-thermal emissions. (*) The energy at which the footpoint and above-the-loop-top source have the same flux.

To obtain a first order correction for pile-up fluxes, we estimated the fraction of pile-up in each image. The pile-up fractions are calculated to be 46, 12 and 4% for peaks 1, 2 and 3, indicating pile-up events significantly affect affect the peak 1 data. We assumed the thermal photon from the flare loop to be dominant in pile-up events. In the latter, the pile-up signals behave as higher energy photons in the location of the flare loop in the modulation curve. Hence, we consider that all of the pile-up events affect only coronal sources, and corrected their fluxes, which were then used in Fig. 5.7.

A comparison of spectra with and without pile-up correction in peak 1 is shown in Fig. 5.9. The sum of fluxes from two sources match the total spectrum with pile-up correction, while the black points exceed the total flux in the spectrum without pile-up correction. Photon indices of the above-the-loop-top source without pile-up correction is 5.7±0.4. The difference between the spectral indices with and without the correction is 0.4±1.0, which is within one sigma error. For peaks 2 and 3, pile-up counts are much lower than the peak 1 case, and do not therefore influence the obtained results.

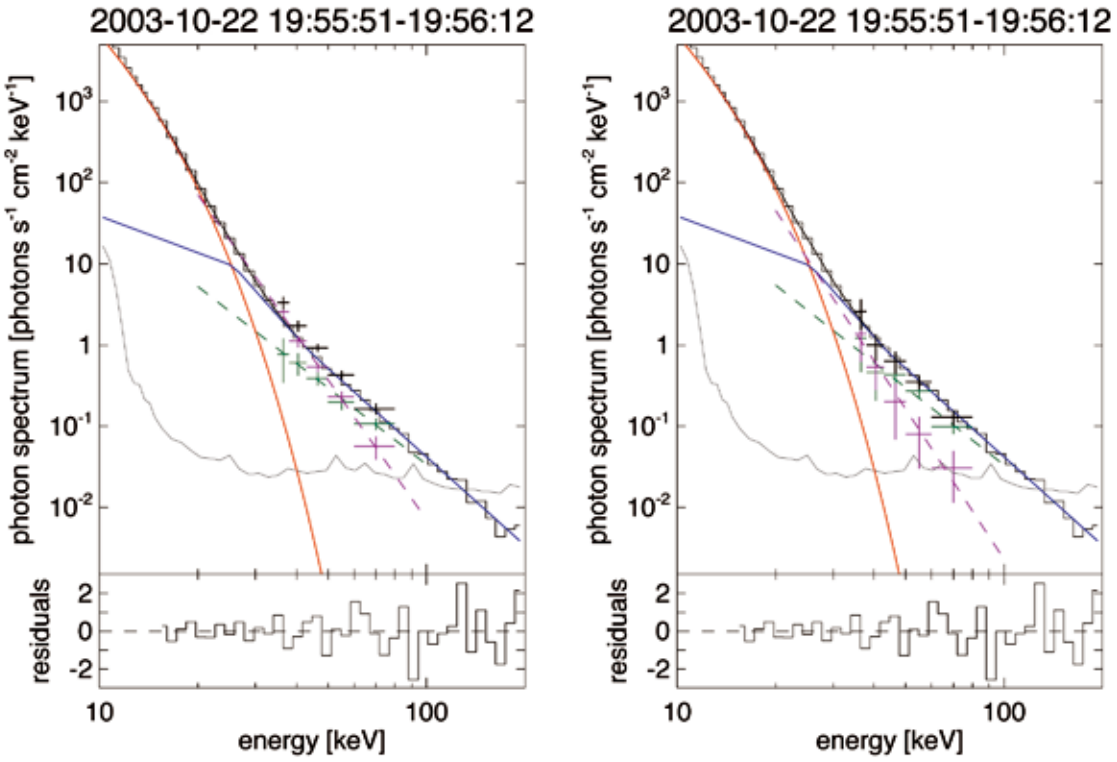

Figure 5.9 Spectra of peak 1 without (Left) and with (Right) pile-up correction.

5.6 Probability of partial occultation of the footpoint emission

In the Masuda flare, it is suspected that the footpoints are partially occulted (Wang et al. 1995). The Hα ribbons and radio emissions are likely occulted in the Masuda flare. By comparing the X-ray, microwave and Hα observations, Wang et al. (1995) suggest that the HXR footpoints may also be partially occulted.

The EUV limb is at a higher altitude than the photosphere (see Fig. 5.6), possibly because the altitude of the chromosphere at which the energetic particles in the coronal lose energy is relatively high. Therefore, even if EUV ribbons are occulted, HXR footpoints can be fully visible. A faint EUV emission is seen slightly (<10 arcseconds) above the HXR source.

If the HXR footpoint is partially occulted, the spectrum at high energy is expected to be affected. High energy emission in footpoints is observed to occur from slightly lower altitudes (e.g., Konter et al. 2009; Saint-Hilaire et al. 2010). By this effect, a spectrum of partially occulted footpoint source is steeper in higher energies due to the occultation of high energy emissions. However, the observed spectrum does not show a downward break in peaks 1 through 3, so here, we regard that the footpoints aw likely to be fully visible in peaks 1 through 3. The peak 4 spectrum in Fig. 5.7 has a high-energy break, but its image is observed to be on disk.

5.7 Time variation of each source

We checked the time variation of each source after the attenuator state changed to A3. We made images of every 2 rotating periods ($\sim$8 s) after 19:56:18 UT, and calculated the fluxes of the coronal source and the northern and southern footpoints. The calculated fluxes are plotted in Fig. 5.10. Error bars are 10% of the higher flux at each time interval. The black line is the light curve of the total flux, and data points are fluxes of the northern (blue), southern footpoints (green) and the coronal source (magenta). The two peaks in the black line correspond to the HXR peaks 2 and 3.

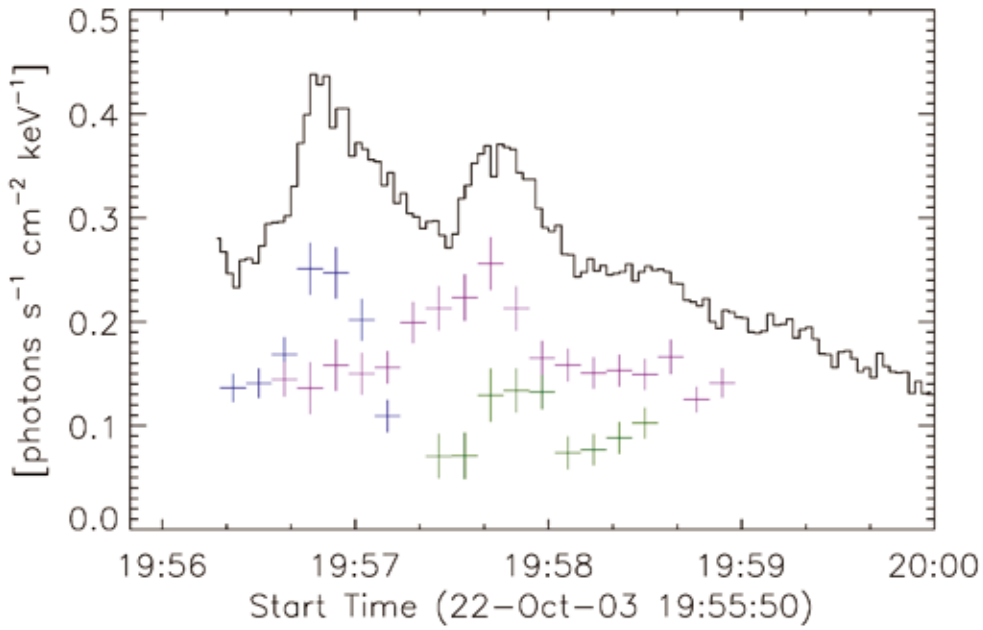

Figure 5.10 Time profiles of the northern (blue), southern footpoints (green) and the coronal source (magenta). The black line is the total flux.

Although the maximum flux value at the one pixel in the image region is higher for footpoint sources, the coronal source is rather wide. Therefore, the integrated fluxes in the image region are higher for the coronal source than the southern footpoint (this is also consistent with the spectra in Fig. 5.7).

In Fig. 5.10, the coronal and southern footpoint sources are associated with peak 3, which strongly suggests that two sources in peak 3 are related. The peak of the coronal source is at ∼19:57:42, and that of the southern footpoint is ∼8 s later. The variability of peak 2 only corresponds to the northern footpoint. Therefore, the coronal source seen in Fig. 5.4 is only a rising phase of the peak associated with the HXR peak 3. The peak time of the northern peak is at ∼19:56:46, which is also that of the HXR peak 2.

Emissions from the northern peak decay quickly, in a time scale of ∼10 s, while that of the southern footpoint seems to be of the same order. The coronal source

decays slightly more slowly, in a time scale of $\sim$20 s.

Discussions on the relation of two sources in peak 3 and a suggested model are shown in Chapter 6.

Chapter 6

Discussion of HXR emissions in above-the-loop-top and footpoint sources*

6.1 Third HXR peak of the October 22, 2003 event

In the October 22, 2003 flare, both a coronal above-the-loop-top and a footpoint source are clearly detected up to ∼150 keV. In this chapter, we discuss their relation, based on the results given in the previous chapter. We opt to discuss the HXR sources for the peak with highest statistics and low pile-up fraction (peak 3). The coronal above-the-loop-top and footpoint sources are associated in the time profiles around peak 3, which resembles the Masuda flare. Therefore, we compare the sources of peak 3 with the Masuda flare and the above-the-loop-top source detected by *RHESSI* on December 31, 2007 (Krucker et al. 2010).

We assume that the HXR emissions are from non-thermal electrons with power-

* The updated content of this section is published by ApJ, Vol. 737, article id. 48, 2011, entitled "On the Relation of Above-the-loop and Footpoint Hard X-Ray Sources in Solar Flares" by S. Ishikawa, S. Krucker, T. Takahashi and R. P. Lin.

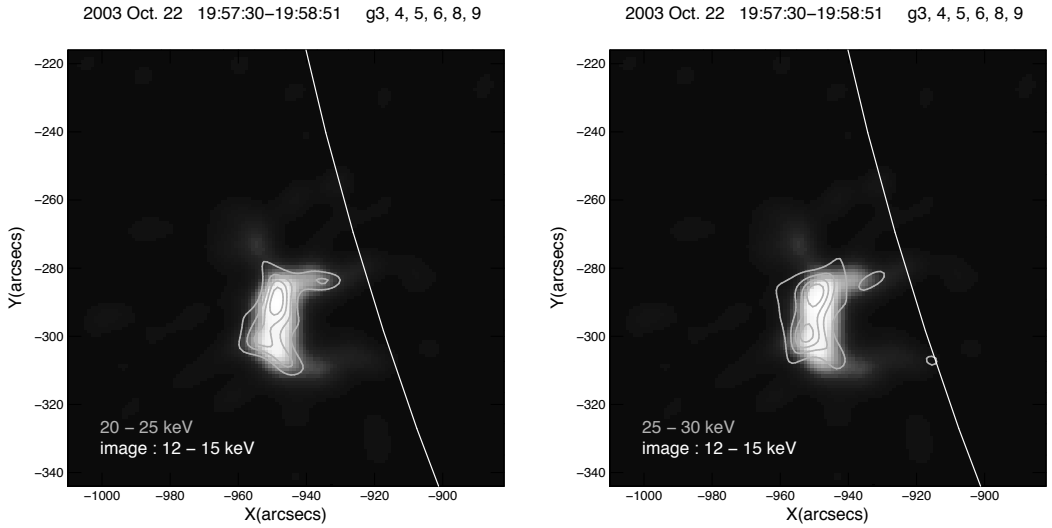

Figure 6.1 20-25 and 25-30 keV images (cyan contours) with the 12-15 keV thermal loop (color image) of peak 3. MEM is used for reconstructing images. contour levels are 20, 40, 60, 80%.

law spectrum. By Fig. 5.7, the high-energy component of the peak 3 spectrum has higher value than the thermal emission above ∼30 keV, which indicates that the accelerated electrons have low energies at least down to 30 keV. 20-25 and 25-30 keV images are plotted in Fig. 6.1, with the thermal flare loop of 12-15 keV. The 20-25 keV image has almost the same shape as that of 12-15 keV, indicating that any significant emissions, whether thermal or non-thermal, are not detected in the above-the-loop-top region below 25 keV. Conversely, the 25-30 keV image is slightly extended to the above-the-loop-top region, which suggests that the non-thermal HXR emission from the above-the-loop-top source could be extended below 30 keV. However, the cut-off energy is not necessary lower than 30 keV, since it is impossible to distinguish the non-thermal component from the thermal component from the main flare loop and estimate the non-thermal flux. In this chapter, we basically assume the low-energy cut-off of the accelerated non-thermal electrons to be 30 keV, although it could be lower. The thermal emission from the flare loop is higher at lower energies, and due to the low dynamic range of *RHESSI* such as ∼10, the non-thermal component may be hidden even below 25 keV. The thermal flux of the peak 3 spectrum in Fig. 5.7 is

more than ∼10 times higher than the extended power-law line of the coronal source below ∼25 keV.

We also assume the thick-target model for the footpoint HXR emission, and the thin-target model for the coronal source. The density of the chromosphere around the footpoint increases to $> 10^{11}$ cm^{-3} along with approaching to the photosphere, while the typical density of the corona is significantly low, such as $< 10^{9}$ cm^{-3}. The column density N_s, in which an electron with the initial energy E_e losses its energy completely by collisions, calculated as

$$N_s = 1.5 \times 10^{17} \left(\frac{E_e}{\mathrm{keV}} \right) \ \mathrm{cm}^{-2} \tag{6.1}$$

(e.g., Emslie 1978). In the corona, providing the density is 10^{9} cm^{-3}, the 50 keV electron will run 380 Mm. Conversely, if the density is 10^{9} cm^{-3} at a footpoint, the 50 keV electron will lose all the energy within 3.8 Mm, meaning our assumption would be valid. The verification of the thin-target assumption for the above-the-loop-top source is also described in Section 6.5.

6.2 Above-the-loop-top source

The size of the above-the-loop-top source of peak 3 is estimated as ∼11 Mm × 6 Mm (see Section 5.3). Assuming that the source has the same width and depth, the volume can be estimated as

$$V \sim (6 \ \mathrm{Mm})^2 \times 11 \ \mathrm{Mm} = 4.3 \times 10^{26} \ \mathrm{cm}^3. \tag{6.2}$$

Although the ambient thermal density cannot be estimated due to the absence of low-energy emission in the image, the thermal density at the above-the-loop-top region n_0 should be significantly lower than that of the flare loop. Assuming the ambient thermal density above the loop top is a typical value in the corona, $n_0 = 10^{9}$ cm^{-3}, the number of low-temperature thermal electrons is

$$n_0 V \sim 4.3 \times 10^{35}. \tag{6.3}$$

In the above-the-loop-top region, only the non-thermal HXR emission is detected, while no significant thermal emission is detected in < 25 keV. This suggests that the above-the-loop-top region is purely a non-thermal source, and all electrons are accelerated to the non-thermal spectrum. We confirm this presumption as follows. Using the thin-target assumption and the observed parameters of the flux and photon index, the collisional energy loss rate in peak 3 $\mathcal{E}_{thin}$, which can be regarded as the heating rate of ambient electrons, is estimated (e.g., McKenzie et al. 1973; Krucker et al. 2010) as

$$\mathcal{E}_{thin} \sim 1.2 \times 10^{27} \left(\frac{E_c}{30 \text{ keV}} \right)^{-\gamma_c+1} \text{ erg/s}, \tag{6.4}$$

where E_c is the cut-off energy and γ_c =5.1 is the photon index. Assuming the thermal ambient electrons of eq. 6.3 are energized to high temperature by collisions, the heating rate is

$$\begin{aligned} \frac{\mathcal{E}_{thin}}{n_0 V} &\sim 2.8 \times 10^{-9} \left(\frac{E_c}{30 \text{ keV}} \right)^{-\gamma_c+1} \left(\frac{10^9 \text{ cm}^{-3}}{n_0} \right) \text{ erg/s} \\ &\sim 14 \left(\frac{E_c}{30 \text{ keV}} \right)^{-\gamma_c+1} \left(\frac{10^9 \text{ cm}^{-3}}{n_0} \right) \text{ MK/s}. \end{aligned} \tag{6.5}$$

Therefore, the ambient low-temperature thermal electrons in the above-the-loop-top region can be quickly energized to a super hot temperature (such as 100 MK). Although the density could be low, the emission at the super-high temperature should be detected.

Assuming the thermal ambient electrons are superheated to 8 keV ($\sim$93 MK), the flux with emission measure of $\sim 3 \times 10^{46}$ cm^{-3} is comparable to that of the thermal flare loop at 20-30 keV range. However, there is no sign of such emission. Therefore, at least the emission measure should be less by the *RHESSI* dynamic range $\sim$10, which suggest the upper limit of the emission measure EM_{ul} to be $\sim 3 \times 10^{45}$ cm^{-3}. Assuming the number of non-thermal electrons are comparable to that of thermal ambient electrons in case of the upper limit, the upper limit of the density of thermal ambient electrons n_{ul} is estimated as

$$n_{ul} \sim \sqrt{\frac{EM_{ul}}{2V}} \tag{6.6}$$

$$\sim 1.9 \times 10^9 \text{ cm}^{-3}. \tag{6.7}$$

Applying this n_{ul} to eq. 6.5, the temperature will be 93 MK within ∼12 s, which is less than the observation time. Following the discussion in the similar case of Krucker et al. (2010), we conclude that all electrons are accelerated.

By the thin-target model (Brown 1971) and the flux and photon index obtained by the observation, the instantaneous number of non-thermal high-energy electrons N_{inst} in the above-the-loop-top region of peak 3 is estimated as

$$N_{inst} = 9.8 \times 10^{35} \left(\frac{10^9 \text{ cm}^{-3}}{n} \right) \left(\frac{E_c}{30 \text{ keV}} \right)^{-\gamma_c+3/2}, \tag{6.8}$$

where n is the ambient proton density within the above-the-loop-top source (corresponding to the electron density including the thermal and non-thermal component, $n > n_0$). We assume E_c =30 keV, although it is possible that E_c is lower such as <20 keV in the Masuda flare or <16 keV in the December 31, 2007 flare. Therefore, we explicitly show the dependence on the cutoff energy in each equation.

In the above-the-loop-top region, we assume the density of non-thermal electrons n_{NT} ($n_{NT} \sim n - n_0$) to be uniform. Using the instantaneous number N_{inst} and the volume V in eq. 6.2, n_{NT} can be derived as

$$n_{NT} \sim \frac{N_{inst}}{V} = 2.3 \times 10^9 \left(\frac{10^9 \text{ cm}^{-3}}{n} \right) \left(\frac{E_c}{30 \text{ keV}} \right)^{-\gamma_c+3/2}. \tag{6.9}$$

We follow the interpretation of Krucker et al. (2010) that all electrons in the above-the-loop-top are non-thermal, assuming $n \sim n_{NT}$. Hence N_{inst} and n can be estimated as

$$N_{inst} \sim 6.5 \times 10^{35} \left(\frac{E_c}{30 \text{ keV}} \right)^{-\gamma_c/2+3/4}, \tag{6.10}$$

$$n \sim n_{NT} \sim 1.5 \times 10^9 \left(\frac{E_c}{30 \text{ keV}} \right)^{-\gamma_c/2+\frac{3}{4}} \text{ cm}^{-3}. \tag{6.11}$$

With this assumption, while the ambient density n is a lower limit, the instantaneous number N_{inst} and the density of non-thermal electrons n_{NT} are the upper limit. If the thermal ambient electron is present significantly ($n_0 > 0$), the target density $n \sim n_0 + n_{NT}$ will be higher, hence the non-thermal electrons will be small. Since the upper limit of the abient thermal density n_{ul} is comparable with the calculated non-thermal density n, at least ∼a half of the electrons should be accelerated.

The average energy of non-thermal electrons $\langle E \rangle$ from cut-off energy E_c is derived by

$$\langle E \rangle = \frac{\int_{E_c}^{\infty} E \cdot E^{-\delta} dE}{\int_{E_c}^{\infty} E^{-\delta} dE} = \frac{\delta - 1}{\delta - 2} E_c, \tag{6.12}$$

where δ is the power-law index of the electrons. Assuming the thin-target model, the power-law index of electrons in the above-the-loop-top region δ_c is $\delta_c = \gamma_c - 1/2$. Therefore, the averaged electron energy $\langle E \rangle$ is

$$\langle E \rangle = \frac{\delta_c - 1}{\delta_c - 2} E_c = \frac{\gamma_c - 3/2}{\gamma_c - 5/2} E_c = 42 \left(\frac{E_c}{30 \text{ keV}} \right) \text{ keV}. \tag{6.13}$$

Hence, the total instantaneous energy of accelerated non-thermal electrons above 30 keV at the HXR peak time is estimated as

$$E_{inst} = N_{inst} \langle E \rangle \sim 4.3 \times 10^{28} \times \left(\frac{E_c}{30 \text{ keV}} \right)^{-\gamma_c/2+7/4} \text{ erg}. \tag{6.14}$$

Again, note that the estimated instantaneous non-thermal energy is the upper limit. While this E_{inst} is smaller than the thermal energy in Table 5.1, E_{inst} is strongly dependdent on the cut-off energy. Furthermore, if accelerated particles are injected and/or the electrons are re-accelerated, the total energy of accelerated electrons in the whole duration of peak 3 could be larger than E_{inst}.

Table 6.1 shows a summary of these estimations of the above-the-loop-top source, compared to that of other two events. For this comparison we used the same value of $E_c = 16$ keV for all events. While the *GOES* classes of the Masuda and tDecember 31, 2007 flares are similar (M2), that of the October 22, 2003 is M9.9. Because of this, it is more difficult to determine the cut-off energy E_c for the October 22 event than for that of December 31. Although the location of the coronal source in the October 22 flare is similar to that of the other two events, the estimated size of the source is different. The volume is $\sim$4 times larger than that of the Masuda flare, and $\sim$2 times smaller than that in December 31. However, projection effects could be responsible for these differences. While the flux of peak 3 of the October 22 event at 50 keV is similar to that of the December 31 event, the photon index γ_c is steeper by $\sim$1.1. As a result, the total energy of accelerated electrons could be $\sim$30 times larger than that

of the Masuda flare and ∼3 times larger than that of December 31. Note that the total energy would be comparable to the December 31 event in case E_c ∼30 keV (in eq. 6.14), due to the steep photon and electron indices.

6.3 Footpoint source

Unlike the December 31, 2007 event, the October 22, 2003 event has an advantage in that the footpoint source is also detected. In the following we assume that electrons are accelerated mainly in the above-the-loop-top region, and that the footpoint is produced by electrons escaping the coronal source. We estimate the energy loss rate in the footpoints from the observed spectrum assuming the thick target model, and then calculate the time it takes to empty out the coronal acceleration region through the escape of electrons to the footpoints. Although the presence of the compact above-the-loop-top HXR source indicates the electrons are trapped, we do not assume any trapping or escape mechanism for this estimation. In the peak 3 of October 22, one footpoint could be occulted, and we note that more energy than estimated here may be lost in footpoints.

By assuming the thick target model, the energy loss rate $\mathcal{E}_{loss}$ of the footpoint source in peak 3 is estimated at

$$\mathcal{E}_{loss} = 1.3 \times 10^{27} \left(\frac{E_0}{30 \text{ keV}} \right)^{-\gamma_f + 1} \text{ erg/s}, \tag{6.15}$$

where E_0 is the cut-off energy of the non-thermal photons, and $\gamma_f = 3.6$ is the photon index of the footpoint source. Following the same discussion as the case of E_c, we assumed $E_0 = E_c$ =30 keV.

The average energy of non-thermal electrons $\langle E_f \rangle$ from cut-off energy E_0 is derived by a calculation similar to eq. 6.12. In the thick-target assumption, the power-law index of electrons δ_f has the relation $\delta_f \approx \gamma_f + 1$. Therefore, in the case of peak 3,

$$\langle E_f \rangle = \frac{\delta_f - 1}{\delta_f - 2} E_0 = \frac{\gamma_f}{\gamma_f - 1} E_0 = 41.5 \left(\frac{E_0}{30 \text{ keV}} \right) \text{ keV}. \tag{6.16}$$

Parameter	Masuda Flare	2007DEC31 Flare	2003OCT22 Peak3
Duration	∼2 minutes	∼2 minuts	∼2 minuts
Decay time (FWHM)	∼30 s	∼40 s	∼20 s
Flux at 50 keV (ph s^{-1} cm^{-2} keV^{-1})	∼0.02	∼0.2	∼0.2
Height above photosphere	∼20 Mm	∼27 Mm	∼25 Mm
Hiehgt above flare loop	∼7 Mm	∼6 Mm	∼6 Mm
Length	∼5 Mm	∼29 Mm	∼11 Mm
Width	∼5 Mm	∼6 Mm	∼6 Mm
Volune*	$\sim 1 \times 10^{26}$ cm^3	$\sim 8 \times 10^{26}$ cm^3	$\sim 4 \times 10^{26}$ cm^3
Pre-flare ambient density	low	low	low?
γ_c at hard X-ray peak time	4-5.5	∼4.2	∼5.1
Electron spectral index, δ_c	3.5-5.0	∼3.7	∼4.6
Non-thermal electron density (>16 keV)*	$\sim 2 \times 10^9$ cm^3	$\sim 2 \times 10^9$ cm^3	$\sim 5 \times 10^9$ $\times(E_c/16\text{ keV})^{-1.8}$ cm^3
Energy in non-thermal electron (>16 keV)*	$> 1 \times 10^{28}$ erg	$> 1 \times 10^{29}$ erg	$\sim 7 \times 10^{28}$ $\times(E_c/16\text{ keV})^{-0.8}$ erg

Table 6.1 Summary of properties of non-thermal emissions of the coronal sources.

(*) Assuming all electrons are accelerated.

Parameter	Masuda Flare (total of two footpoints)	2003OCT22 Peak3
Flux at 50 keV (ph s^{-1} cm^{-2} keV^{-1})	∼0.1	∼0.1
Area		~ 12 Mm^2
γ_f at hard X-ray peak time	3.2-4.0	∼3.6
Electron spectral index, δ_f	4.2-5.0	∼4.6
Electron loss rate (>16 keV)	$> 4 \times 10^{35}$ s^{-1}	$> 1 \times 10^{35}$ $\times(E_0/16 \text{ keV})^{-1.6}$ s^{-1}
Energy loss rate (>16 keV)	$> 2 \times 10^{28}$ erg/s	$> 6 \times 10^{27}$ $\times(E_0/16 \text{ keV})^{-2.6}$ erg/s

Table 6.2 Summary of properties of non-thermal emissions of the footpoint sources.

Based on the energy loss rate and eq. 6.16, the electron loss rate can be estimated as

$$\mathcal{N}_f \sim \frac{\mathcal{E}_{loss}}{\langle E_f \rangle} \sim 1.9 \times 10^{34} \left(\frac{E_0}{30 \text{ keV}} \right)^{-\gamma_f} \text{ electrons/s.} \quad (6.17)$$

The properties of the footpoint source compared with the Masuda flare are shown in Table 6.2. We re-used the same value of $E_0 = 16$ keV for the comparison. Similar to the coronal above-the-loop-top sources, the spectral indices show similar values in these two events. Although the flux of the footpoint source (total of two footpoints) is ∼5 times higher than the above-the-loop-top source of the Masuda flare at ∼50 keV, it is comparable to or lower than that of the above-the-loop-top source of peak 3 of this event. The lower limits of the energy and electron loss rates, which are derived by the detected HXRs, are lower than those of the Masure flare to within a factor of ∼2.

6.4 Comparison and implications

In this event, the difference of the photon indices $\Delta\gamma = \gamma_c - \gamma_f$ is calculated as $\Delta\gamma = 1.5 \pm 0.5$. In case that the single non-thermal electron component with spectral index of δ emits thin and thick target bremsstrahlung, if the escape is assumed to be energy-independent, the photon indices of emissions are $\delta + 1/2$ and $\delta - 1$, respectively. In this case, the difference of photon indices between two emissions is 1.5. $\Delta\gamma = 1.5 \pm 0.5$ in peak 3 of this event is consistent with the simple assumption with a single electron component, within the error. Therefore, this event can be explained without any additional elements such as non-collisional energy loss by electric fields as discussed in Battaglia & Benz (2007, 2008). Although the energy dependence of the escape probability is not known, in case the escape probability is proportional to the speed of the particle, the photon index with the thin-target assumption is $\delta + 1$. Even in this case, the $\Delta\gamma$ should be 2.0, hence the observed $\Delta\gamma$ is consistent with the single electron component, within errors.

Figure 6.2 shows the time dependence of the spectral index of the coronal and footpoint sources, as obtained by the flux ratio of 35-45 and 45-100 keV images. The dashed lines show the peak-averaged indices obtained in Section 5.5. The spectra of the sources are not found to have changed significantly along the rising, peak and decay time intervals. Although the tendency is for emissions to have harder spectra around the peak, it is almost consistent that the indices are constant within errors. Therefore, the time variations of the sources do not contradict our assumption.

By comparing this value and eq. 6.10, the time τ taken to empty the above-the-loop-top region by electron precipitation into the footpoint is

$$\tau = \frac{N_{inst}}{\mathcal{N}_f} \sim 34 \left(\frac{E_c}{30 \text{ keV}} \right)^{-\gamma_f + \gamma_c/2 + 3/4} \left(\frac{V}{4.3 \times 10^{26} \text{ cm}^3} \right)^{1/2} \text{ s}, \tag{6.18}$$

where $E_c = E_0$ is assumed. Since $\gamma_c = 5.1$ and $\gamma_f = 3.6$ in this event, the power $-\gamma_f + \gamma_c/2 + 3/4$ is 1.8. For instance, in case the cut-off energy is $E_c = E_0$ =16 keV, as same as Krucker et al. (2010), the time scale τ would be 11 s, the same order as the case of E_c =30 keV. In case that the cut-off energy is low, while the number of the non-thermal electrons in the coronal region increase, the electron loss rate at the

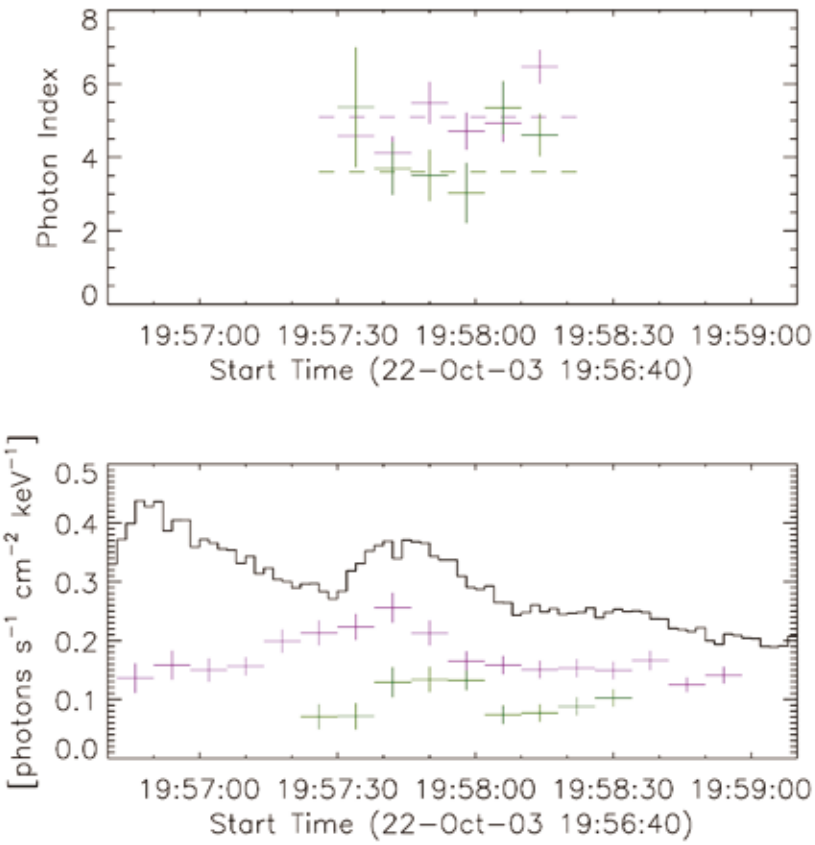

Figure 6.2 *Top*: Time varieties of the HXR spectral indices of the coronal (magenta) and the footpoint (green) sources during peak 3. The dashed lines are the averaged indices obtained by the whole duration of peak 3 (see Section 5.5). *Bottom*: The light curves of the total flux (black), the coronal (magenta) and the footpoint (green) sources for the reference.

footpoint increases with the same fraction. Hence the escape time τ is not strongly dependent on the cut-off energy E_c. Note that τ ∼34 s is the upper limit, because energies are also lost in the occulted footpoints. By assuming the presence of a second footpoint with the same properties as visible the footpoint, as is often seen in two footpoint flares (e.g., Saint-Hilare et al. 2008), the escape time would be ∼17 s. If most of the footpoint emission is occulted, τ could be even shorter. Furthermore, by assuming the thermal ambient electrons are not significant ($n_0 \sim 0$), N_{inst} estimated here is an upper limit, and τ could be more smaller. Even if τ is the upper limit of 34 s, it is lower than the decay time scale of the whole duration of peak 3 (∼60 s). Conversely, the estimated value of 17 s is consistent with the decay time scale of the coronal source (∼20 s, see Section 5.7). This indicates that the assumption in this chapter, in which all the electrons in the above-the-loop-top region are accelerated, is consistent with the observation. In the Masuda flare, the time in which accelerated electrons lose their energy is ∼0.5 s, which is smaller than the decay time of ∼30 s. In that case, electrons in the above-the-loop-top region must be replaced and accelerated multiple times.

The size of the footpoint source of peak 3 is estimated by the MEM image as (3.2 Mm, 3.5 Mm). The width of the cross-sectional surface w_f corresponds to 3.5 Mm, while the cross-sectional area of the footpoint A_f is estimated to be $A_f \sim w_f^2 = 1.2 \times 10^{17}$ cm^2. The escaped electrons from the above-the-loop-top region travel along the flare loop, wrapping around the magnetic field line, and reach the footpoint. The average speed of the non-thermal electrons above the cut-off energy from the above-the-loop-top source $\langle v \rangle$ is

$$\langle v \rangle = \sqrt{\frac{2\langle E \rangle}{m}} \sim 8.5 \times 10^9 \left(\frac{E_c}{30 \ \mathrm{keV}} \right)^{1/2} \ \mathrm{cm/s}, \tag{6.19}$$

in the non-relativistic case, which is also assumed in the thick target model calculation by Brown (1971). The speed along the flare loop is determined by the pitch angle θ, the angle between the magnetic field line and the velocity vector. Therefore, the beam density around the root of the flare loop n_B is estimated as

$$n_B = \frac{\mathcal{N}_f}{A_f \langle v \rangle |\cos\theta|} \sim 1.8 \times 10^7 \frac{1}{|\cos\theta|} \left(\frac{E_c}{30 \ \mathrm{keV}} \right)^{-\gamma_f - 1/2} \ \mathrm{cm}^{-3}. \tag{6.20}$$

This value is ∼100 times smaller than the estimated ambient density in the above-the-loop-top region n.

Assuming the volumes of the above-the-loop-top region and the leg of the flare loop to be comparable, the fraction of total fluxes emitted through the thin target by the accelerated electrons depend on the sojourn time scale. The sojourn time in the loop leg is

$$\Delta t \sim \frac{L}{\langle v \rangle |\cos\theta|} \sim 0.13 \frac{1}{|\cos\theta|} \text{ s}, \tag{6.21}$$

where L is the length of the flare loop leg ∼30 Mm, and θ is the pitch angle. If the pitch angle is nearly isotropic, the factor will be $(1/|\cos\theta|) < 10$ for almost all the particles. The fraction of the total fluxes of the coronal source $f_{coronal}$ and the loop leg f_{leg} is

$$\frac{f_{leg}}{f_{coronal}} \sim \frac{\Delta t}{\tau}\phi_e \sim 2.5 \times 10^{-3} \frac{\phi_e}{|\cos\theta|}, \tag{6.22}$$

where ϕ_e is the ratio of the emissivities. Since the flare loop has the higher density by a factor of ∼44 at bright region on the loop top, the emissivity ratio should be $1 < \phi_e < 44$. Conversely, If the second footpoint has the same property as the first, τ will be half this value and this fraction will be half. Therefore, the non-thermal HXR emission in the legs of the flare loop is not detectable in the *RHESSI* observations.

6.5 Models

Based on these estimations, the scenario whereby all electrons in the above-the-loop-top region are accelerated and escape along the flare loop to precipitate into the footpoints, is consistent with the observational results. Figure 6.3 shows a schematic cartoon of the October 22, 2003 flare derived from our observations. The green dashed curve is the limb by sight from *RHESSI*, and emissions on the other side of the curve are occulted. The 12-15 keV HXR and EIT EUV images suggest that the southern footpoint seen in peaks 3 and 4 is clearly associated with the main flare loop. The northern footpoint in peaks 1 and 2 is associated with another flare loop.

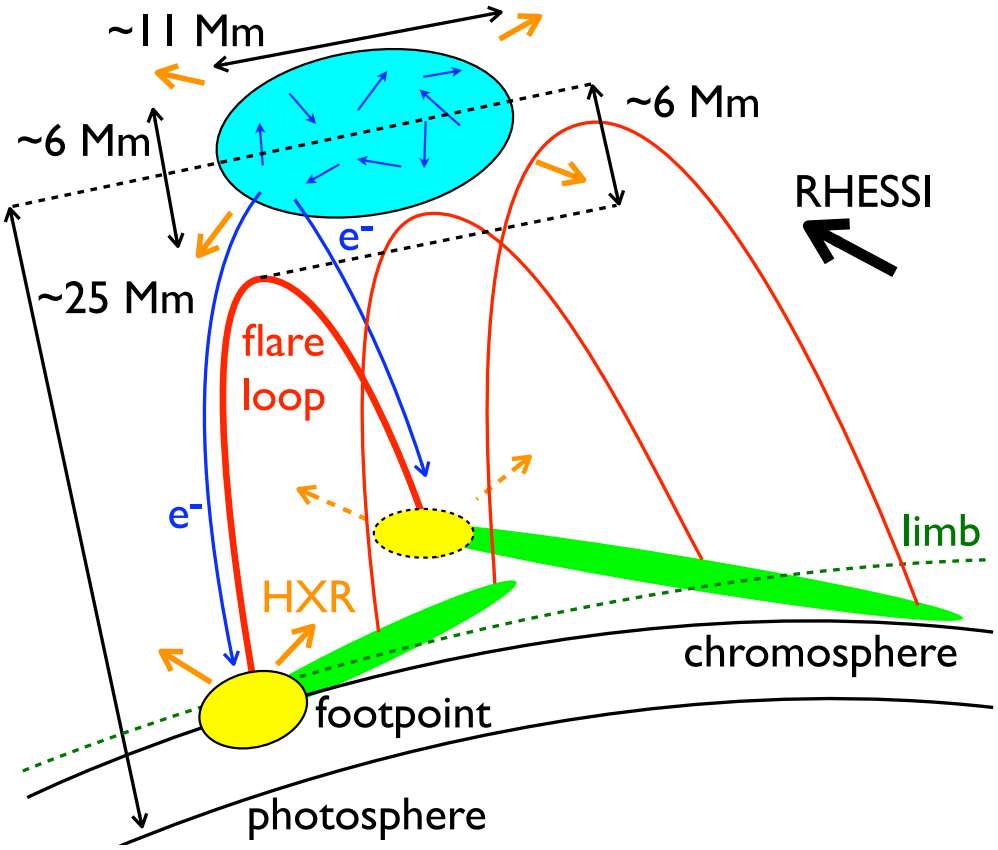

Figure 6.3 Schematic picture of the model of the October 22 flare discussed in this chapter.

The second footpoints of the northern and southern footpoints would be occulted, and their latitude would be intermediate between the two. It is not clear whether the northern and southern footpoints are associated with the same flare ribbon or not. In case these footpoints are at the same flare ribbon, the ribbon lies between the visible footpoints and should be detected in EUV. Therefore, the absence of such ribbon in the EIT image might suggest that the northern and southern footpoints are at different ribbons. We assumed the different flare ribbon with these footpoints in the schematic. However, a flare ribbon is lower in height than the footpoint, hence the possibility of the ribbon being occulted and the footpoints seen.

After energy release by magnetic reconnection, all the $\sim 6.5 \times 10^{35}$ electrons in the reconnection region are accelerated. The operating acceleration mechanism remains unknown. The electrons have a power-law spectrum with an index of $\sim$4.6. The accelerated electrons were trapped in the accelerated region with $11 \times 6 \times 6$ Mm^3, at $\sim$6 Mm above the flare loop top. These electrons emitted non-thermal HXR by thin-target bremsstrahlung. Since thermal ambient electrons are absent, the energy lost by collision in the above-the-loop-top region is not used for energizing ambient electrons in the same region. The electrons in the acceleration region escape, and travel along the main flare loop. However, the escaped electrons themselves are not detectable in the flare loop, because their time there is so short. The escaped electrons from the above-the-loop-top region precipitate into the chromosphere, and produce the footpoint emission by thick-target bremsstrahlung. The electrons escape within a time scale of $\sim$20 s. To explain the footpoint emission, no further electron acceleration (such as re-acceleration) is needed.

This model is also consistent with the delay of the peak in the footpoint compared to the coronal emission. Since the footpoint emission is the precipitated electrons, the footpoint emission should be brighter when the coronal emission decreases more. In the lightcurves in Fig. 5.10, the peak of the footpoint flux is exactly at the decay phase of the coronal emission.

The thin-target assumption in the above-the-loop-top region can be verified by comparing the time scales of the escape and energy loss. The energy loss time τ_{loss}

is estimated as (e.g., Vilmer et al. 1982)

$$\tau_{loss} = 0.2 \times \left(\frac{\langle E \rangle}{1 \text{ keV}}\right)^{3/2} \left(\frac{10^9 \text{ cm}^{-3}}{n}\right) \text{ s} \quad (6.23)$$

$$\sim 36 \text{ s}. \quad (6.24)$$

The time scale of energy loss is longer than the escape time scale τ=17 s, and the electrons will escape before the change of the spectrum through energy loss by collisions. Since the time scale τ could be smaller, the thin-target assumption is thought to be valid.

HXR emissions in the flares with above-the-loop-top sources can be explained by this simple picture, acceleration in the above-the-loop-top region and precipitation into the footpoint. However, since the time scale τ is lower than the decay time scale in the Masuda flare, certain flares with above-the-loop-top sources require further acceleration.

If the escape time scale is relatively short compared to the acceleration efficiency, even if acceleration continued sufficiently long time, more accelerated electrons would contribute not to the coronal emission, but the footpoint emission. In such a case, the above-the-loop-top source is is relatively weak, and therefore probably undetectable with the HXR imagers currently available. Therefore, the ratity of above-the-loop-top sources detection could be attributable to the fact that most flares have higher escape probabilities than the events that show above-the-loop-top sources.

6.6 Coronal trapping

By comparing the derived average speed of electrons in the above-the-loop-top region ($\sim 8.5 \times 10^9$ cm/s) and the source size ($\sim$10 Mm), electrons should bounce $\sim$144 times in the time scale τ. The trapping in the compact region for such a long time may be rather difficult. This is also the problem to explain the above-the-loop-top source in the Masuda flare.

The possible mechanism to trap energetic plasma is the magnetic mirror. To trap particles by the magnetic mirror, the energy density of the magnetic field should

sufficiently high compared to that of the particle motion. To evaluate the effect of the magnetic field, the plasma beta $\beta = p/p_m$ is often used where p is the gas pressure and p_m is the magnetic pressure. The magnetic field strength can be estimated by the radio observation, because the radio emission is produced by gyrosynchrotron. However, in the October 22 event, there was no radio observation, hence it is impossible to estimate the magnetic field strength. In the December 31 event, in which the parameter of the above-the-loop-top source is similar (see Table 6.1), the magnetic field strength is estimated at 30-50 G (Krucker et al. 2010). Assuming the similar magnetic field, the plasma beta in the above-the-loop-top region of the October 22 event is calculated as

$$\beta = \frac{8\pi p}{B^2} \tag{6.25}$$

$$\sim \frac{16\pi \langle E \rangle n}{3B^2}, \tag{6.26}$$

which is estimated at 0.7-1.9. Since the magnetic pressure is comparable to the energy by motions, the electrons could be trapped by the magnetic mirror.

Several models are proposed to explain the coronal trapping in the Masuda flare and other *Yohkoh*/HXT observations. Fletcher & Martens (1998) show that the magnetic field configuration of the CSHKP model can explain the coronal trapping by the magnetic mirror. In case the pitch angle of the accelerated electrons are rather high, a large number of electrons can be trapped in the above-the-loop-top region. Tsuneta & Naito (1998) suggests that the trapping region is surrounded by the slow-mode MHD shock. This model may explain the compact source size of the above-the-loop-top sources. Metcalf & Alexander (1999) discuss that a single acceleration mechanism is sufficient for explaining both coronal and footpoint sources of the three *Yohkoh*/HXT flares, and therefore the explanation of the trapping by Fletcher & Martens (1998) and Tsuneta & Naito (1998) are consistent with their observations.

In Fletcher & Martens (1998), the time scale of escape should be that of the pitch angle scattering. The pitch angle scattering time τ_s of this event is estimated as

(Leach & Petrosian 1981)

$$\tau_s \sim \frac{(\langle v \rangle / c)^3 \Gamma^2}{4\pi c n r_0 \ln \Lambda (1 - \cos^2 \theta)} \tag{6.27}$$

$$\sim 21 \frac{1}{1 - \cos^2 \theta} \left(\frac{E_c}{30 \text{ keV}} \right)^{\gamma_c/2+3/4} \text{ s}, \tag{6.28}$$

where c is the speed of light, Γ is the Lorentz factor, $r_0 = 2.82 \times 10^{-13}$ cm is the classical electron radius and $\ln \Lambda \sim 26.7$ in the October 22 event is the Coulomb logarithm. Although this value depends on the cut-off energy, τ_s is consistent with the estimated escape time scale τ.

6.7 Acceleration model consistent with the observation

To explain our observation and estimation, there are some theoretical models of the acceleration mechanism. One of them is the model of acceleration by the coalescing magnetic islands accompanying with the magnetic reconnection (Drake et al. 2006). In the reconnection region, a magnetic structure of clusters ("magnetic islands") is formed, and electrons are accelerated by the Fermi acceleration. In this model, almost all electrons in the multi magnetic island region could be accelerated. Therefore, the above-the-loop-top source in the October 22 flare could be the multi magnetic island region itself.

In addition, acceleration continues until electrons have comparable energy to magnetic energy, such as $\beta \sim 1$ in the model of Drake et al. (2006). Accelerated electrons will not interact frequently with magnetic islands in case $\beta > 1$. Therefore, this could be the reason why $\beta \sim 1$ is observed in the December 31, 2007 event (Krucker et al. 2010).

However, there is a problem with a gap between the spatial scale of acceleration shown in the model (∼cm) and that of the HXR source size in flares (∼Mm). While the fractal structure of current sheets might explain this difficulty (e.g., Shibata & Tanuma 2001), further investigation is required to obtain the complete picture of the above-the-loop-top source and acceleration in solar flares.

Chapter 7

Future Mission for Further Study of Particle Acceleration in Solar Flares

7.1 Limitation of Current Observations

To understand particle acceleration in solar flares, further HXR explorations are necessary. In particular, coronal HXR sources are not sufficiently observed. It is proposed that particles are accelerated close to the magnetic reconnection point above the top of magnetic loops (e.g., Yokoyama & Shibata 1998), and observations of coronal loop-top sources are important to reveal the properties and mechanism of particle acceleration. However, it is difficult to detect coronal HXR sources in the presence of footpoint emissions, due to higher brightnesses of footpoint HXR sources. Higher dynamic range is required for further explorations.

Further observations of smaller flares are also desired to reveal a complete picture of particle acceleration in solar activity. Many microflares have been observed by *RHESSI*, with non-thermal energy down to 10^{26}-10^{27} erg (Christe et al. 2008). Although it is revealed that previous studies underestimated the non-thermal energy, the energy content of *RHESSI* microflares is not enough to heat the corona to >1 MK. All of the flare events observed by *RHESSI* are in active regions, and no flare has

been detected in quiet regions. Smaller events down to 10^{24} erg outside of active regions, often referred to as nanoflares, are only observed in thermal SXR and EUV emissions. Therefore, non-thermal emission and particle acceleration in nanoflares is still unknown.

Flares with smaller scales may contribute significantly to the coronal heating (Parker 1998). Hence, to estimate contributions of nanoflares, it is necessary to evaluate the non-thermal energies of these small events. Higher sensitivity is demanded to observe smaller flares.

Past solar HXR observations, such as those by HXT onboard the *Yohkoh* satellite (Kosugi et al. 1991, 1992) and those by the *RHESSI* satellite (Lin et al. 2002), have made use of non-focusing imaging techniques such as the RMC imaging technique providing HXR imaging spectroscopy (Hurford et al. 2002). By using RMCs, it is required to reconstruct an image from an observed modulation curve. Because of this, the PSF has side lobes such as those shown in Fig. 3.8, and images are not able to achieve high dynamic range. Such imaging techniques are are not well-suited to observe loop top sources as they are limited by low dynamic range and high background due to the need for large detectors.

7.2 Hard X-ray Focusing Optics

To overcome the problems of low dynamic range and sensitivity with detectors using RMCs, HXR focusing optics show promise for next-generation HXR observation with imaging and spectroscopy. By using focusing optics, arrival directions of incident photons can be determined directly, and image reconstructions are straight forward. Thanks to this, the PSF becomes sharp and the dynamic range can be improved compared to RMCs. Furthermore, focusing enables the use of small focal plane detectors which imply a drastic reduction in non-solar background counts, thereby increasing the sensitivity to faint HXR sources.

To implement this concept, grazing-incidence HXR focusing optics are a promising new technology for future solar observations. For focusing HXR, an incidence angle of <0.5 degree is needed, and accumulating significant effective area is difficult.

Recently, several HXR focusing optics have been successfully demonstrated, such as the High-Energy Replicated Optics (*HERO*) program (Ramsey et al. 2002). The *HERO* telescope is designed to observe at a 50 μcrab sensitivity with sufficiently long observations. In a 3-hour balloon flight, the HXR images of galactic sources such as Cyg X-1 were successfully obtained in the energy range from 20 to 45 keV.

HXR focusing optics are planned to be used in future missions to observe HXRs from astronomical sources. The Nuclear Spectroscopic Telescope Array (*NuSTAR*) misson by NASA, a satellite mission planned to be launched in 2012, will observe 6-80 keV HXRs by using HXR optics for the first time in space. A Half Power Diameter (HPD) of $\sim$45 arcseconds will be achieved with a 10 m focal length (Harrison et al. 2005, Koglin et al. 2009).

HXR focusing optics will also be used for the Hard X-ray Imager (HXI) onboard the *ASTRO-H* mission, the 6th Japanese X-ray observation satellite mission, to be launched in 2014 (Takahashi et al. 2010, Kokubun et al. 2010). A $\sim$100 arcseconds half power diameter will be achieved with a focal length of 12 m in the energy range from 5 to 80 keV (Kunieda et al. 2010). In addition, *ASTRO-H* has other detectors: the Soft X-ray Spectrometer (SXS) with an unprecedented energy resolution of 7 eV in $\leq$ 10 keV, the Soft X-ray Imager (SXI) for 0.5-12 keV X-ray with Charge Coupling Devices (CCDs), and the Soft Gamma-ray Detector (SGD) for 10-600 keV with an unprecedented sensitivity.

These missions are astronomical missions to observe astrophysical objects, not for the Sun. Although the technology of HXR focusing optics is originally applied to such astronomical missions, it is also attractive for solar observations. The Focusing Optics X-ray Solar Imager (*FOXSI*, Krucker et al. 2009, 2011) will for the first time demonstrate the concept of applying HXR focusing and imaging for the Sun.

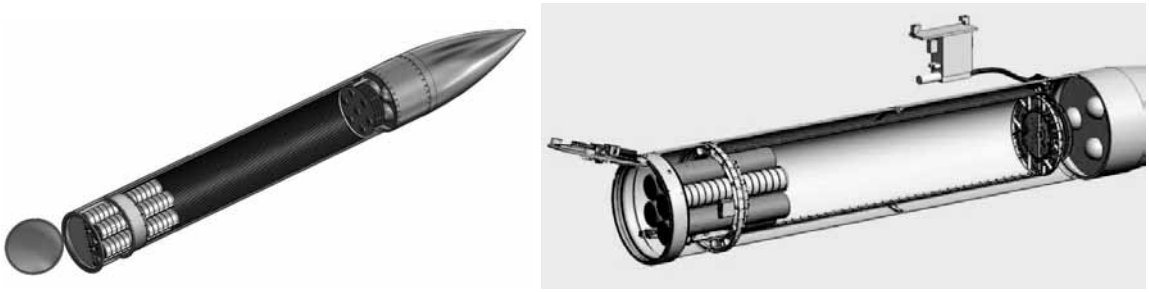

Figure 7.1 Design of the *FOXSI* payload and telescopes.

7.3 The Focusing Optics X-ray Solar Imager (*FOXSI*)

7.3.1 Mission Overview

To observe HXRs from accelerated particles, a new sounding rocket mission, the Focusing Optics X-ray Solar Imager (*FOXSI*), will test out grazing-incidence HXR focusing optics combined with solid state position-sensitive detectors for solar observations (Krucker et al. 2009, 2011). This is the first observation of the Sun with HXR focusing optics. In this mission, HXR activity in the quiet Sun will be observed for a duration of approximately 5 minutes. Its science goal is to detect the non-thermal radiation from nanoflares between 5-15 keV. As will be shown in the next subsection, this energy range is suitable to detect non-thermal HXR from nanoflares. The combination of high-resolution focusing X-ray optics and fine-pitch imaging sensors will enable superior sensitivity, about 50 times better than that of *RHESSI*. The effective area will also be improved to 120 cm^2, four times larger than the total effective area of *RHESSI*. *FOXSI* is to be launched in 2012, from the White Sands Missile Range, New Mexico, USA.

Figure 7.1 shows the design of the *FOXSI* payload. Seven HXR focusing optics modules are coupled with 7 detector units at the focal plane 2 m away. Table 7.1 shows an overview of the characteristics of *FOXSI*. The HERO team at NASA Marshall Space Flight Center (MSFC), led by Dr. Brian Ramsey, is responsible for the design

Energy range	∼5 to 15 keV
Energy resolution (FWHM)	∼1 keV
Focal Length	2 m
Angular resolution (FWHM)	12 arcseconds
Field of view (HPD)	640 × 640 arcseconds
Effective area	120 cm^2 (8 keV), ∼10 cm^2 (15 keV)
Sensitivity	0.004 $cm^{-2}s^{-1}keV^{-1}$(∼8 keV)
Dynamic range	100 for source separation >30 arcseconds
Observation time	∼360 s
Launch site	White Sands Missile Range, NM, USA
Launch date	March 2012

Table 7.1 *FOXSI* overview (Krucker et al. 2009, 2011).

and development of the focusing optics, and our group of the Institute of Space and Astronautical Science (ISAS) in Japan is responsible for the design and development of the focal plane detectors. The Space Sciences Laboratory at the University of California, Berkeley is leading this effort.

The *FOXSI* optics are grazing incidence telescopes with a Wolter I geometry (confocal paraboloid and ellipsoid). The MSFC mirror fabrication method uses a single highly polished form (mandrel) which is then electro-coated to produce many individual high-resolution mirrors. This process has already been implemented and successfully demonstrated for HXR astronomy in the HERO program (Ramsey et al. 2002). A single *FOXSI* telescope module consists of 7 nested shells. The spatial resolution of these modules is expected to be ∼12 arcseconds.

The expected PSF of *FOXSI* is plotted in Fig. 7.2, and compared to other X-ray missions including *RHESSI* and *HERO*. *HERO* telescope modules contain 15 nested shells. *RHESSI* uses a non-focusing imaging system, and the limited dynamic range is clearly shown in the left panel of Fig. 7.2. The FWHM angular resolution of *FOXSI* is expected to be 12 arcseconds, and the HPD will be 15 arcseconds.

7.3.2 Observations with *FOXSI*

Two spectra in Fig. 7.3 show expected data of a nanoflare observation by *FOXSI*. The left and right panels show the photon spectrum and count spectrum. The largest

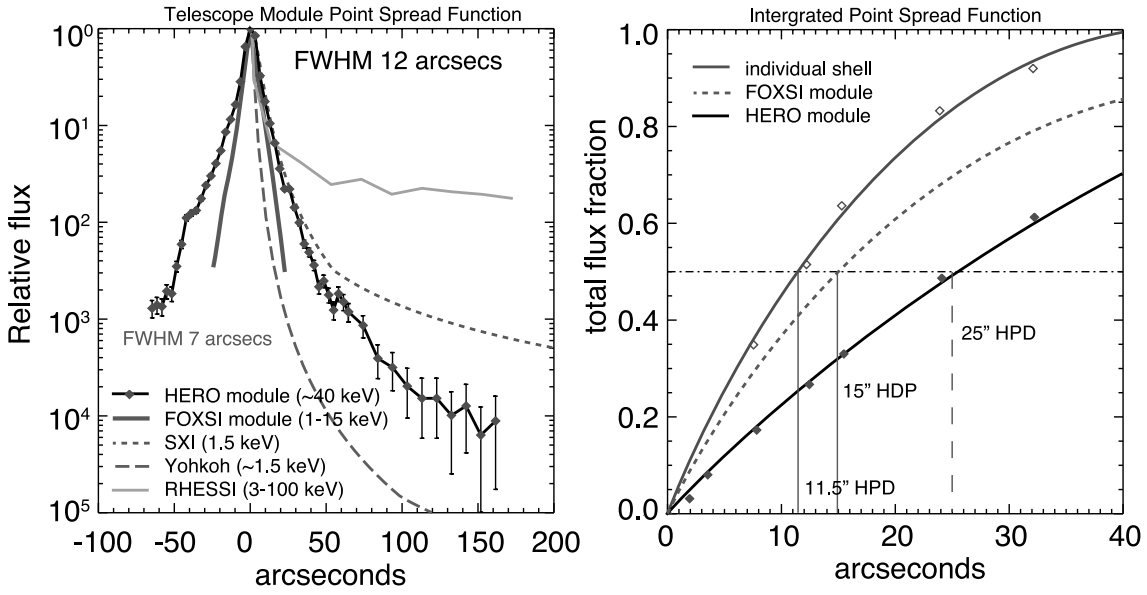

Figure 7.2 (*Left*) The point spread function of the *FOXSI* telescope compared to other instruments. (*Right*) The integrated point spread function of *FOXSI*. The HPD of *FOXSI* is expected to be 15 arcseconds.

nanoflare observed in SXR (T ~2 MK, $EM \sim 10^{44}$ cm^{-3}, $E_{thermal} \sim 5 \times 10^{25}$ ergs and duration of 60 s, from Krucker et al. 1997) is assumed for the thermal spectrum. Non-thermal spectra are calculated assuming that the energy content in non-thermal electrons is equal to the thermal energy content. The photon indices of 1.7 and 5 are assumed for below and above the turn-over energy E_0. The red line shows a thermal spectrum of T =2 MK, and the three blue plots show non-thermal counterparts with different E_0. No statistical error is assumed in the blue lines, and data points are simulated with expected *FOXSI* response and statistics. Absorption by external material and the energy dependence of effective area are shown in data points of the count spectrum. Low energy photons will be absorbed by the entrance window material, and effective area will decrease at higher energies. The largest event is assumed to hold a total of 400 counts.

Since the temperature of thermal electrons is ~2 MK, emission detected above 3 keV is expected to be non-thermal. Based on this simulation, *FOXSI* is able to

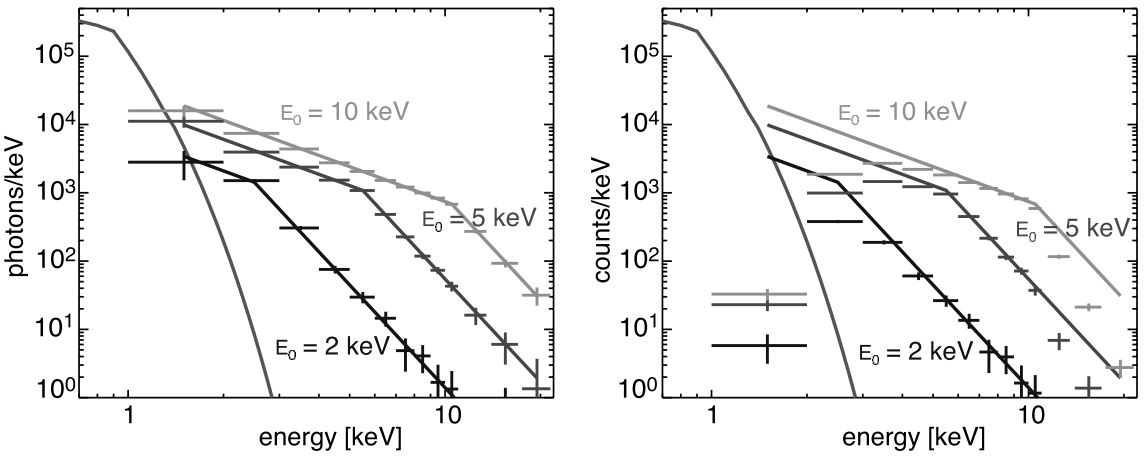

Figure 7.3 Expected spectra of *FOXSI* observations. The red line shows a thermal spectrum of T =2 MK, and blue plots show non-thermal counterparts. Three spectra with different turn-over energy E_0 are shown. The photon indices of -1.7 and -5 are assumed for below and above the turn-over energy. (*Left*) The X-ray photon spectrum. (*Right*) The count spectrum. Low energy photons will be absorbed by the entrance window material.

detect non-thermal HXR from nanoflares with a superior sensitivity. Not detecting non-thermal counterparts would indicate that nanoflares are heated by a different mechanism than flares in active regions.

Simulated image of *FOXSI* observations is shown in Fig. 7.4. The left panel shows a full-disk *SOHO*/EIT 195 Å EUV image from July 1996 with quiet corona conditions near disk center. A blue dashed line shows the *FOXSI* field of view of 640×640 arcseconds, and a red line shows the region used for simulations. The next image is the quiet Sun in EUV as observed by EIT with all significant thermal brightenings during 5 minutes outlined in dark blue line (Krucker and Benz 1998). There are 74 statistically significant brightenings during this time period. The right panel shows a simulated *FOXSI* image based on the EIT EUV image. It is assumed that all thermal brightenings seen in EUV have non-thermal conterparts in HXRs. The black contours show areas with statistical significance of 5 sigma and above. In this simulation, at least 29 statistically significant sources can be identified. Therefore, it is clearly confirmed that nanoflare events can be observed with the spatial resolution of *FOXSI*. Based on EUV observations from EIT and *TRACE*, 10-1300 nanoflares with 10^{25} ergs are expected in the *FOXSI* FOV of 640×640 arcseconds during a 5 minute rocket flight. Simultaneous EUV and SXR observations with *Hinode*, *STEREO* and *SDO* will help to resolve ambiguities in *FOXSI* images.

In addition to nanoflare observations in the quiet corona, *FOXSI* observations of active regions will reveal ∼50 times fainter microflares than *RHESSI*. The smallest microflare with enough statistics to analyze has $\sim 10^{27}$ erg. It is therefore expected that *FOXSI* can detect smaller events down to $\sim 2 \times 10^{25}$ erg. It is expected that *FOXSI* will observe 5 flares in the observation time.

Observations of non-thermal HXR in larger flares by focusing optics is very attractive, because spatial structures of flares along and above magnetic loops will be spatially resolved. However, most of emissions in the energy range of 5-15 keV are thermal emissions, and it would be difficult to detect large flares within the limited duration of 5 minutes. Observations of large flares by focusing HXR optics will be left to space-based mission in the future (also described in the second half of the next subsection).

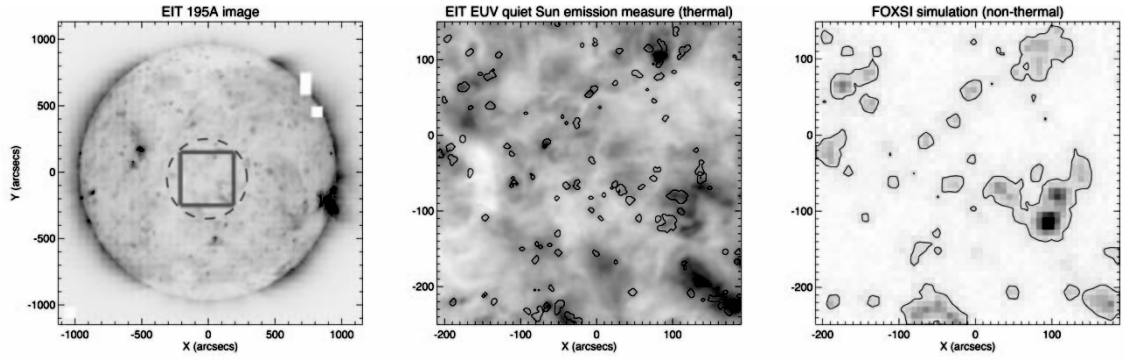

Figure 7.4 (*Left*) Full disk EIT 195 Å image from July 1996 with quiet corona conditions near disk center. A blue dashed line shows the *FOXSI* field of view, and a red line shows the region used for simulations. (*Center*) The EUV quiet Sun image by EIT with all significant thermal brightenings in 5 minutes, outlined with a dark blue line (Krucker and Benz 1998). (*Right*) A simulated *FOXSI* image. A pixel size is 7.5 arcseconds, assuming that all thermal brightnings seen in EUV have non-thermal HXR conterparts.

To achieve the goal of *FOXSI*, several properties are required for focal plane detectors. A good position resolution is required for well resolved imaging, and a good energy resolution is required to detect X-rays with as low energy as possible. These requirements suggest the use of semiconductor detectors with fine position resolution and good energy resolution. Details will be discussed in the next chapter.

7.3.3 *FOXSI* 2 and Future Missions

After the observation with *FOXSI*, we plan to upgrade *FOXSI* and have a second flight (*FOXSI* 2). The main purpose of *FOXSI* 2 is an observation with improved active area especially in high energy (>10 keV). To attain this objective, HXR optics will be upgraded to add three more shells, from 7 to 10 shells. The effective area will be 160 cm^2 at 8 keV, slightly larger than for *FOXSI* 1. However, at 15 keV, the effective area will be improved to 40 cm^2, four times as large as that of the first flight. The silicon detectors will be replaced with CdTe detectors to take full advantage of

the newly gained sensitivity at high energies. Detectors for *FOXSI* 2 will be described in the Section 8.3. The proposal of *FOXSI* 2 was accepted in 2010, and the *FOXSI*-2 rocket is to be launched in 2013.

After a successful *FOXSI* 2 launch, we are planning to submit a proposal for a spacecraft version of *FOXSI* with unprecedented dynamic range and sensitivity. A spacecraft enables long-duration observations, including many large flares. With HXR focusing and imaging of large flares, the non-thermal radiation from coronal sources will be observed. This will provide a significant leap in understanding the mechanisms of solar flares and particle acceleration. It would be possible to observe HXR in a wider energy range such as 5-80 keV, and such a mission will be at least $\sim$100 times more sensitive than *RHESSI* at 40 keV.

Chapter 8

Development of Imaging Detectors for the *FOXSI* Mission

8.1 Requirements

To meet the science objectives of the *FOXSI* mission, a focal plane detector needs to satisfy the following requirements: A spatial resolution of <116 μm (corresponding to the angular resolution of the optics of ∼12 arcseconds), an energy resolution of below ∼1 keV (FWHM) and good photoabsorption efficiency (better than 50%) in the 5–15 keV band. The focal plane detector also needs to be able to perform quasi-single photon counting for count rates up to ∼100 counts/s expected from the quiet Sun. Existing imaging technologies widely used in focusing X-ray optics do not have meet all of above requirements. For example, charge-coupled devices can achieve good energy resolutions and low threshold energies, however, their time resolution is limited to an order of 1 s (Singh et al. 2005). Therefore, it is critical to develop a new focal plane detector for *FOXSI*.

To achieve a good spatial resolution and low power consumption simultaneously, a double-sided strip detector is attractive as a detector geometry (Watanabe et al. 2009). In a double-sided strip detector, top and bottom electrodes are divided into strips and implemented orthogonally. By reading out signals from both electrodes, the detector can provide 2-dimensional information of energy deposits. Another

advantage of strip detectors is that to obtain spatial information corresponding to $N \times N$ pixels only $2N$ channel must be readout instead of N^2 channels. Therefore, a double-sided strip detector is well-suited to reduce readout channels and power consumption, especially for a detector with a fine spatial resolution.

Based on requirements above, we have developed a double-sided silicon strip detector (DSSD) and a prototype of a double-sided cadmium telluride (CdTe) detector for focal plane detectors of the *FOXSI* missions.

8.2 Development of a Double-sided Si Strip Detector (DSSD) for *FOXSI*[*]

8.2.1 Design

In order to take advantage of the good angular resolution of 12 arcseconds of the *FOXSI* HXR focusing optics, we designed and fabricated a fine-pitch DSSD specified for *FOXSI* (the *FOXSI* DSSD). As the material for the semiconductor imaging detector, silicon has a sufficient photoabsorption efficiency in the energy band of interest. Although other materials such as cadmium telluride or cadmium zinc telluride also have a sufficient efficiency and can achieve good performances under temperatures around -20°C, silicon is a well-researched and highly pure material, and detectors with high performances in high yields can be obtained at low cost. In addition, we have many years of experience in operating silicon detectors in high radiation environments.

DSSDs consist of highly positively doped (p^+) silicon strips (p-side) and negatively doped (n^+) silicon strips (n-side) implanted orthogonally on a n-type silicon wafer (n-bulk). Each n-side strip is surrounded by a floating p^+-doped implantation

[*] The updated content of this section is published by IEEE Trans. Nucl. Sci., Vol. 58, p. 2039, 2011, entitled "Fine-pitch Semiconductor Detector for the *FOXSI* mission" by S. Ishikawa, S. Saito, H. Tajima, T. Tanaka, S. Watanabe, H. Odaka, T. Fukuyama, M. Kokubun, T. Takahashi, Y. Terada, S. Krucker, S. Christe, S. McBride and L. Glesener.

Active Area	9.6 mm×9.6 mm
Thickness	500 μm
Strip pitch	75 μm
Number of strips per side	128

Table 8.1 Specification of the *FOXSI* DSSD.

(p-stop) to isolate it from adjacent strips. Aluminum electrodes are directly coupled on each strip with an ohmic contact. DSSDs have been widely developed for astrophysical and nuclear physics applications (Sellin et al. 1992; Tajima et al. 2003). A DSSD with a strip pitch of 250 μm or 400 μm has been developed by our group as a scattering detector of a Si/CdTe Compton camera (Tajima et al. 2003; Takeda et al. 2007; Watanabe et al. 2007). In this development, we added aluminum electrodes DC-coupled to p-stops in order to minimize the p-stop resistance since it generates Johnson noise. A similar DSSD is also being developed for the Hard X-ray Imager on board the Japanese X-ray astronomy satellite *ASTRO-H* (Takahashi et al. 2010; Kokubun et al. 2010).

The active area of the *FOXSI* DSSD is 9.6 mm×9.6 mm and the number of strips is 128 for p-side and n-side, providing position information for 128×128=16384 pixels by reading out only 128+128 = 256 channels, resulting in lower power consumption. The pitch of the strips is 75 μm, corresponding to an angular resolution of 8 arcseconds at the focal length of 2 m. Hence, the spatial resolution of the optics is oversampled by a factor of 1.5. The thickness is 500 μm, which implies a photoabsorption efficiencies of 98 % for 10 keV and 68 % for 15 keV. Guard-ring electrodes with a width of 100 μm are implemented on both sides to block the leakage current from the periphery. Fig. 8.12 shows a photo, and Table 8.1 shows the specifications of the *FOXSI* DSSD. The device is manufactured by Hamamatsu Photonics, Japan.

8.2.2 The Readout System

To achieve good energy resolutions and a low threshold energy, a 64-channel analog ASIC, VATA451, has been developed by ISAS, KIPAC and GM-IDEAS based on a low noise front end ASIC previously developed for Compton cameras for applications

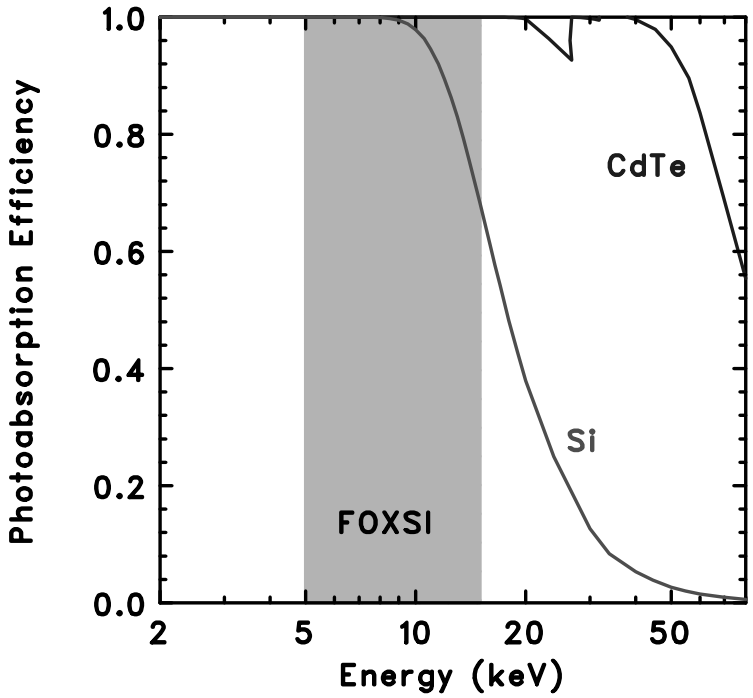

Figure 8.1 Photoabsorption efficiencies of 0.5 mm thick Si (red) and 0.5 mm thick CdTe (blue). Although each of them has sufficient efficiencies in the *FOXSI* energy band, CdTe has a higher efficiency for above ∼10 keV.

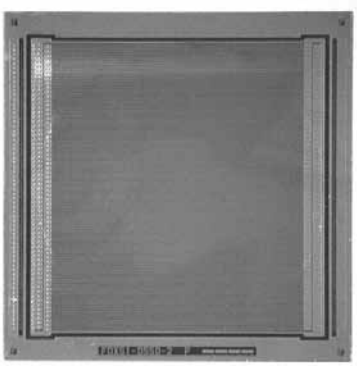

Figure 8.2 Photo of the 128×128 *FOXSI* DSSD. The active area is 9.6 mm × 9.6 mm, and the strip pitch is 75 μm.

including *ASTRO-H*. Fig. 8.3 shows a function block diagram for VATA451. Each channel of the analog circuit of the VATA451 consists of a charge-sensitive amplifier (CSA) followed by two shaping amplifiers, one with a fast shaping time for generating triggers (TA section), and the other with a slow shaping time for charge measurements (VA section). If the output signal from the fast shaper of one or more channels is greater than a threshold value in the TA section, the output signals from the slow shaper of each channel will be sampled and held with an appropriate delay. A Wilkinson-type analog-to-digital convertor, by which all channels can be digitized in parallel, is also included in the VATA451. The ADC is 10 bit and takes 100 μs for digitization with a 10 MHz clock, and output signals are multiplexed. A common-mode noise calculator is also built into the ASIC. Common-mode noise, which is a noise component common to all channels of an ASIC for each event, can be obtained by using the median value of the signals from all channels for each event. These analog and ADC architectures are functionally the same as the former ASIC, VA32TA6.

This ASIC is specifically optimized for the *FOXSI* mission as follows. The gain of the CSA is higher than that of *ASTRO-H* to achieve better noise performance since the energy range of *FOXSI* (below 15 keV) is lower than that of *ASTRO-H*. The fast shaper provides a longer shaping time constant option for generating triggers, which will be beneficial to achieve a low threshold energy required by *FOXSI*. The time constant of the slow shaper can be adjusted from 2 μs to 4μs, and that of the fast shaper can be set to 0.6 μs or 1.2 μs.

The input FET of the VATA451 is optimized to minimize the noise for an input capacitance of 5 pF and a leakage current of 10 pA within a power constraint of 1 mW/channel, resulting in an equivalent noise charge (ENC) of 64 e^- (RMS) for such input loads with a shaping time of 3 μs.

Since there are 128 strips for each p-side and n-side, two ASICs for each side are required, or four ASICs are needed to read out one *FOXSI* DSSD. To connect from the DSSD to the ASICs, each DSSD strip is wire-bonded to the readout pads of the ASICs.

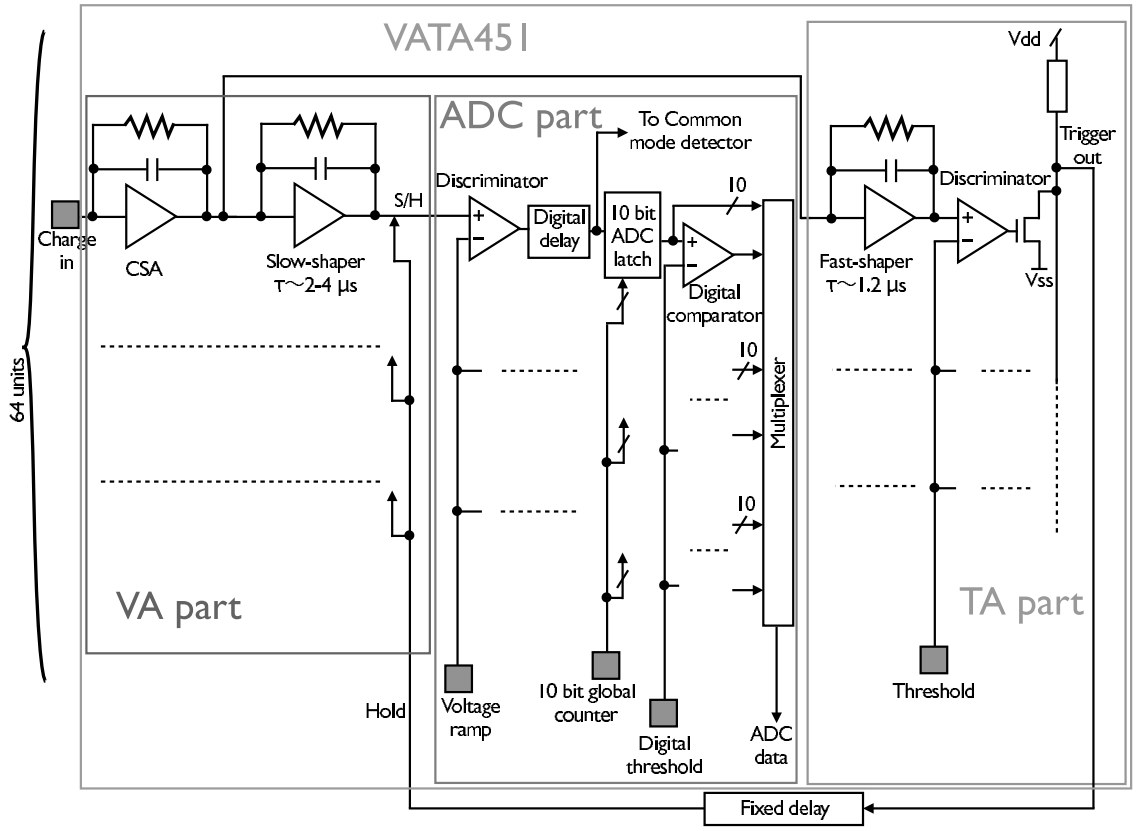

Figure 8.3 Function block diagram of the readout ASIC VATA451. The ASIC consists of the pulse-shaping VA part, and the trigger-generating TA parts. An ADC is also included.

8.2.3 Basic Properties of a DSSD

We measured the leakage current of one central p-side strip of the *FOXSI* DSSD at temperatures of 15°C, 0°C and −20°C (Nominal in-flight temperature is −20°C). Fig. 8.4 shows the measured I-V characteristic. The leakage current is found to be proportional to $\exp(-1/kT)$. This is consistent with the idea that the origin of the current is thermal effect. Under −20°C, the leakage current is measured to be ∼1.5 pA with bias voltages of >200 V. The corresponding ENC is ∼7 e^- (RMS) at a shaping time of 3 μs calculated by a formula $\sim 110\sqrt{I\tau}\ e^-$ where I is the leakage current in nA and τ is the time constant of a readout CR-RC circuit in μs. This

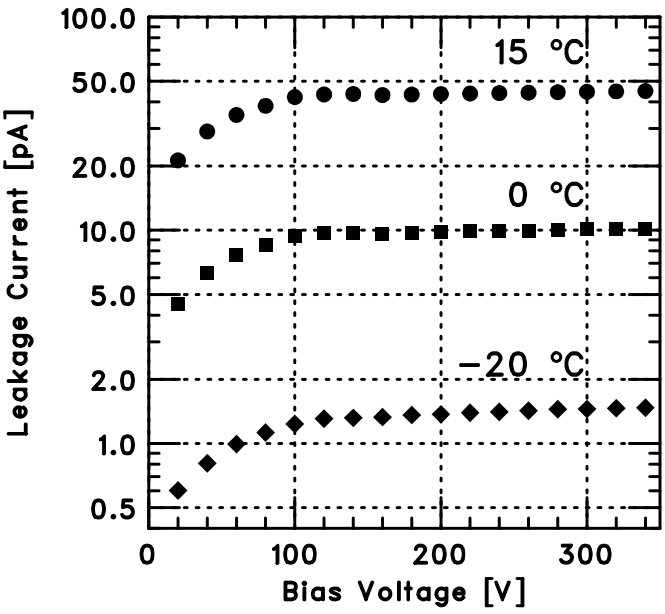

Figure 8.4 I-V characteristic of *FOXSI* DSSD.

result implies that the temperature of -20°C is sufficiently low to obtain the best performance because the noise from the leakage current is negligible compared to normal readout noise.

Fig. 8.5 shows an C-V characteristic of the *FOXSI* DSSD at a room temperature. The body capacitance and the inter-strip capacitances of p-side and n-side were measured. An inter-strip capacitance is a capacitance between one strip and the surrounding strips. The data of inter-strip capacitance are plotted for central p-side and n-side strips. The amplifier noise due to the detector capacitance for a single strip can be parametrized as $\sqrt{20^2 + (10.5 + 7 \times C_{\rm d})^2 + (12.2 + 8.1 \times C_{\rm d})^2/\tau}\ e^-$, where $C_{\rm d}$ is the sum of the body capacitance per single strip and the inter-strip capacitance.

The body capacitance becomes almost constant with bias voltages above $\sim$100 V, which implies that the DSSD is fully depleted at about 100 V. The inter-strip capacitance of the n-side can be measured above 80 V, and becomes almost constant above $\sim$200 V. This implies that n-side strips will be isolated above 80 V, and completely isolated above $\sim$200 V. The C-V characteristic suggests that a higher bias voltage such as 300 V is desired to reduce capacitance noise. The body capacitance for all

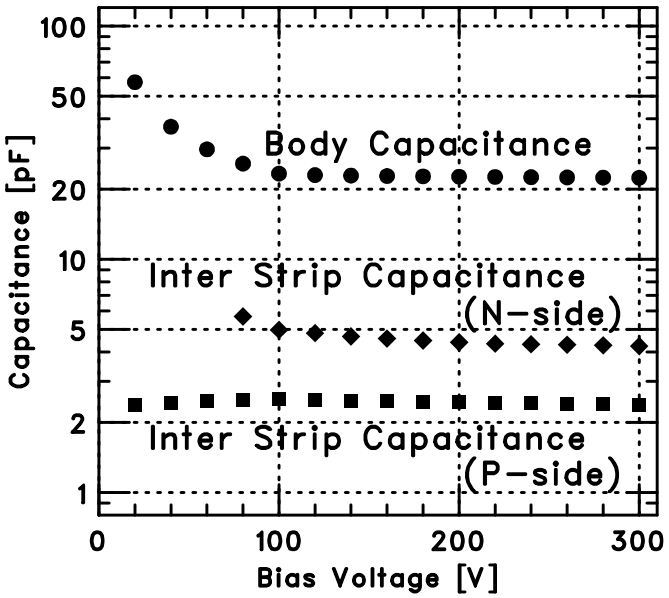

Figure 8.5 C-V characteristic of *FOXSI* DSSD.

strips is measured to be 22.4 pF, that is 0.2 pF per single strip with a bias voltage of 300 V. The inter-strip capacitances of the p-side and n-side are measured to be 2.3 and 4.2 pF at a bias voltage of 300 V.

8.2.4 Performance of a Prototype for the *FOXSI* Focal Plane Detector

We have fabricated a prototype of the *FOXSI* focal plane detector that consists of one *FOXSI* DSSD and four VA451 ASICs. Fig. 8.6 shows a photo of the experimental setup. Wire-bonding from the detector to the ASICs was performed by a semi-automatic wire-bonding machine in our laboratory. Due to operational errors, some wires failed to be bonded. Therefore, some strips are not connected to the ASICs and cannot be read out. Such strips are electrically floated.

Under a temperature of -20°C and a bias voltage of 300 V, we successfully operated the *FOXSI* DSSD. Events from 124 out of 128 strips of the p-side and 120 out of 128 strips for the n-side were used for the following analysis. In the spectral analysis, we use only events where a single hit is detected above the threshold of 5 keV in both

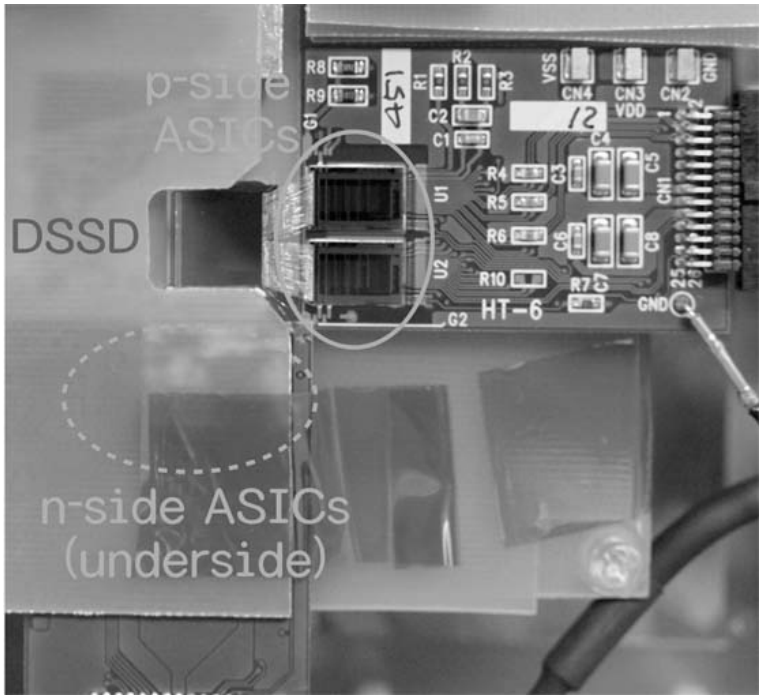

Figure 8.6 Photo of the DSSD experimental setup. Each strip of the DSSD is connected to an ASIC by wire-bonding.

the p-side and n-side in order to suppress events with more than one interaction or any charge sharing between two adjacent strips.

Spectra from the p-side and n-side were obtained with the use of a ^{241}Am radioactive isotope source. The spectra of all active strips on the p-side (black curve) and n-side (gray curve) are shown in Fig. 8.7. The energy resolutions of the p-side and n-side were measured to be 430 eV and 1.6 keV (FWHM) at 14 keV, respectively. Since we can use the better energy information from the p-side for the spectral analysis, it is confirmed that the energy resolution fulfills the mission requirement.

The distribution of energy resolutions (FWHM) of the p-side and n-side strips are shown in Fig. 8.8. The energy resolutions of most channels are distributed from 0.4 to 0.5 keV on the p-side, excluding an exception with an energy resolution of 0.9 keV. The energy resolutions for the n-side are distributed between 0.9 and 1.9 keV with the exception of an outlier at 3.1 keV. Both outliers of the p-side and n-side correspond to edge strips, which neighbor the guard ring. Since the energy resolution and its disper-

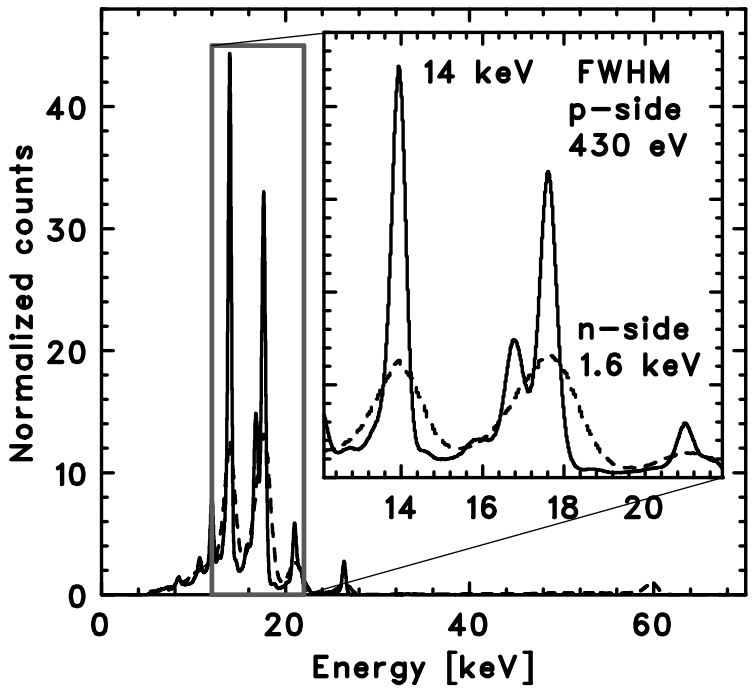

Figure 8.7 Spectra from the p-side (solid line) and n-side (dashed line) of the *FOXSI* DSSD with a ^{241}Am source. The operating temperature was -20°C and the bias voltage was 300 V.

sion are much worse on the n-side than on the p-side, the strip structure on the n-side is considered to be responsible for the excess noise on the n-side. In fact, addition of the DC-coupled aluminum electrode on the p-stop improved the energy resolution. A remaining noise source could be an accumulation layer between p-stops which may act as a floating n-strip with high resistance. Fig. 8.9 shows the position dependence of the energy resolution where we observe a moderate bump structure peaking on the n-side around strip numbers 70–90. Since the resistance of the accumulation layer is highly dependent on the fabrication process, it can reasonably explain the asymmetric bump observed here. On the other hand, we do not observe such structure or large dispersion in the energy resolution on n-side with another DSSD sample for the HXI fabricated in the same batch. These observations may indicate that the excess noise on the n-side originates from the accumulation layer and may depend on the location in the silicon wafer and fabrication process.

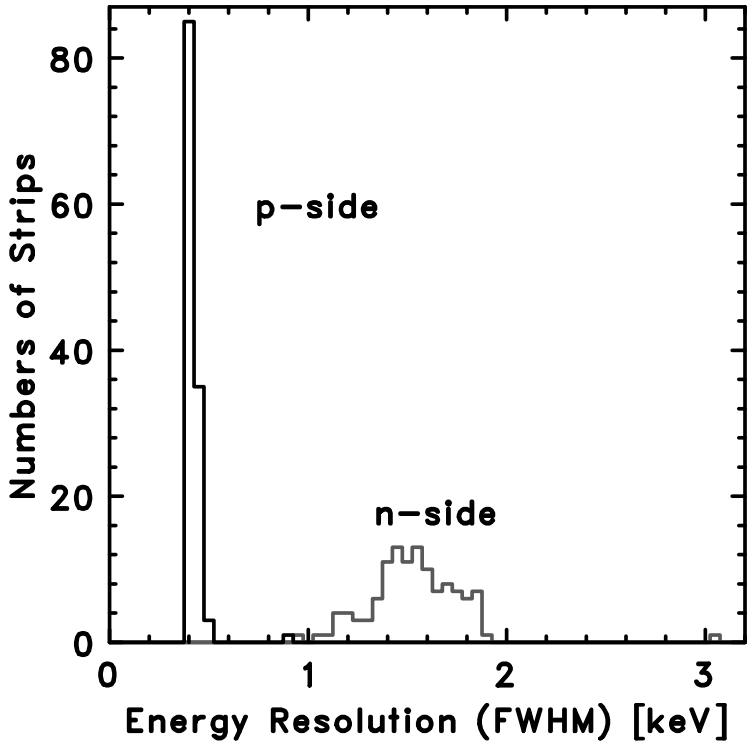

Figure 8.8 Distribution of energy resolution (FWHM) for the 14 keV line.

Although the energy resolution observed for the 14 keV line on the p-side is much better than that on the n-side, it is still worse than the energy resolution expected from the noise performance of the ASIC, especially for higher energies. In order to study the nature of the excess noise on the p-side, we study the energy dependence of the energy resolution as shown in Fig. 8.10. Data points are measured energy resolutions while a gray region gives the resolution calculated from the ASIC noise performance for a load with capacitance of (3.0 ± 0.5) pF at a peaking time of 4.8 μ s (346$\pm$28 eV) and Fano noise (fluctuation of electron hole pairs produced by ionization) where the load capacitasnce includes a parasitic capacitancer of (0.5 ± 0.5) pF. A fit to an empirical formula, $\sqrt{E_0^2 + (f_1 E)^2 + N_{\rm Fano}(E)^2}$ yields $E_0 = 365 \pm 15$ eV, $f_1 = (4.0 \pm 0.5) \times 10^{-3}$ where $N_{\rm Fano}(E)$ is the Fano noise. The linear term may be explained by the gain uncertainties of the ASIC as mentioned in previous papers (Tajima et al. 2003, 2004).

While we can achieve a spectral resolution better than <0.5 keV in the *FOXSI*

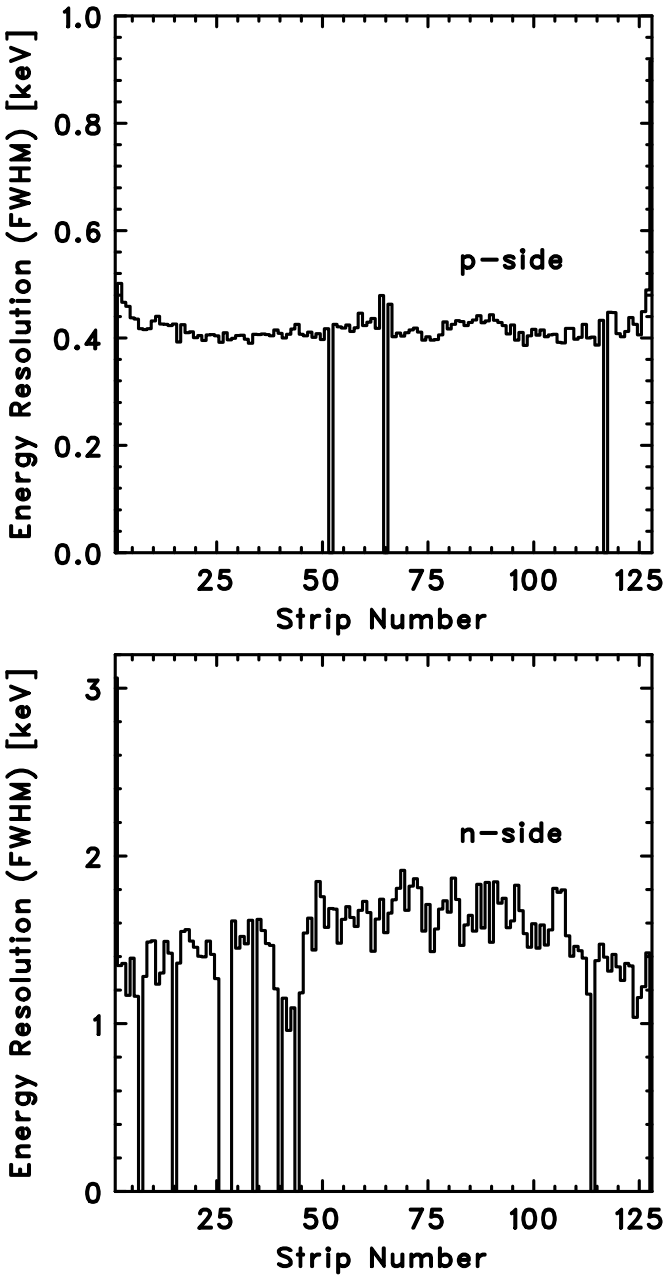

Figure 8.9 Energy resolution (FWHM) for the 14 keV line as a function of the strip number. *Top*: P-side. *Bottom*: N-side.

energy range solely due to a good noise performance on the p-side, the localization of the incident X-ray position still relies on detecting X-ray signals on both the p-side and the n-side. Since the noise performance on the n-side is marginal, we calculate

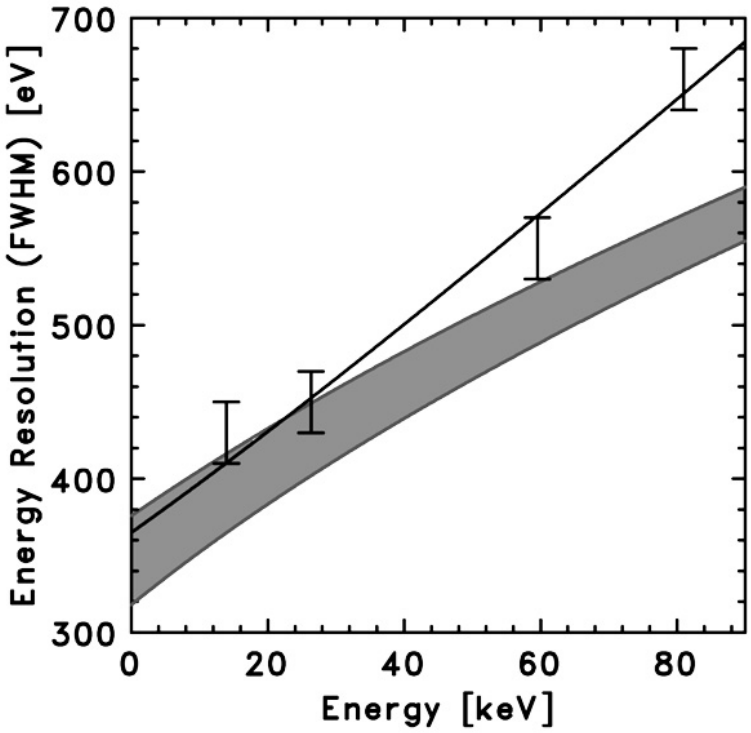

Figure 8.10 Energy resolution (FWHM) as a function of the incident energy. Gray region indicate the energy resolution expected from the ASIC performance. Solid curve shows the fit result.

the probability for wrong localizations. Assuming a Gaussian noise distribution, the energy resolution of 2.0 keV for the n-side corresponds to a chance probability of $<10^{-7}$ for recording an energy above 5 keV due to noise alone. This implies that positions of incident photons can be determined with a negligible probability of spurious hits. Therefore, we confirm that the DSSD can be operated as an imager at a low energy threshold of 5 keV, which fulfills the scientific requirements of the *FOXSI* mission.

Fig. 8.11 shows a shadow image of a tungsten plate with 1 mm pitch slits using X-rays from a ^{133}Ba source in an energy band from 20 to 40 keV. To test the imaging performance, the tungsten plate is tilted by 45° and does not cover the top left part of the detector. The width of the slits is 100 μm. The individual slits are clearly visible, successfully demonstrating the capabilities of fine-pitch imaging and spectroscopy.

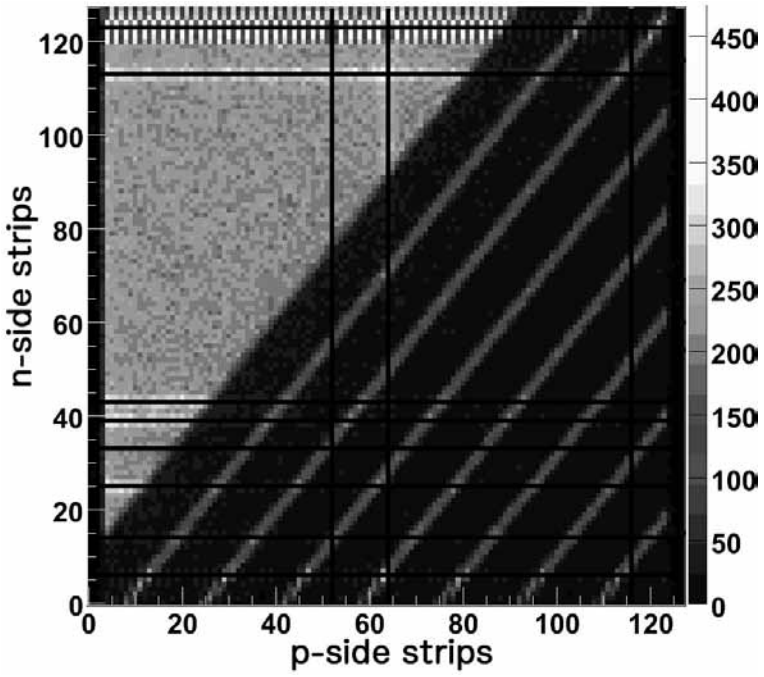

Figure 8.11 Shadow image from the *FOXSI* DSSD with a radio isotope of ^{133}Ba. The scale gives the number of counts. The width of the slits in this image is 100 μm.

In the left part of the top edge of the image ($x \leq 90$ and $y \geq 120$), a longitudinal stripe pattern appears even though counts should be almost flat in this region since there is no mask. In the edges of the p-side strips (the top edge and the bottom edge of the image), wire-bonding pads are placed, which is considered to be the cause of the pattern. The bonding pads are wider than the strips, and therefore staggered. Events in this region can be used for spectroscopy although the spatial resolution for the x-position is worse than the other regions.

On the other hand, although signals are successfully obtained by the p-side, the right and left edges on the image ($x \leq 2$ and $x \geq 125$) have no n-side signal. This is considered to be caused by the presence of wire-bonding pads on n-side. In this region, events can be used only for spectroscopy.

8.3 Development of prototype Double-sided CdTe Detectors for *FOXSI* 2*

8.3.1 The Properties of CdTe

To enlarge the effective area of *FOXSI*, improved HXR optics and detectors are planned to be used for FOXSI 2. As shown in Fig. 8.1, Si has a efficiency of 68% at 15 keV, hence a material with higher efficiency is desired. Recently, CdTe have attracted attention as material for future hard X-ray and γ-ray imaging detectors for astrophysical, medical and industrial application (Takahashi et al. 2001; Limousin et al. 2003). Their large atomic numbers (48 for Cd, 52 for Te), enable high photoabsorption efficiencies. It has also become possible to produce CdTe crystals with large volumes and high uniformity (Bolotnikov et al. 2005, Shiraki et al. 2007). For the *FOXSI* energy range of 5-15 keV, CdTe detector 0.5 mm thick has efficiencies above 99% even in >10 keV (Fig. 8.1). CdTe is also planned to be used for the *ASTRO-H* mission (Takahashi et al. 2010; Kokubun et al. 2010). CdTe detectors would be also applicable as focal plane detectors of HXR focusing optics in future missions dedicated to solar flare observations.

The lifetime-mobility product of charge carriers (especially holes) are small in CdTe crystals ($\mu\tau \sim 2 \times 10^{-3}$ cm^2/V for electrons and $\mu\tau \sim 4 \times 10^{-4}$ cm^2/V for holes (Bencivelli et al. 1991)), which leads to asymmetric spectra (tailing) and reduces the energy resolution. To overcome this difficulty, we have developed thin devices to which a high bias voltage can be applied, thereby reducing the effect of limited mobility. The use of Schottky CdTe diode detectors, with indium (In) and platinum (Pt) as the anode and cathode, respectively, enabled the first fabrication of such devices. However, In anodes of CdTe diode devices cannot be divided into strips or

* The part of this section is published in Jpn. J Appl. Phys. 2010, vol. 49, no. 11, p. 116702, entitled "Development of double-sided CdTe strip detectors for γ-ray imaging and spectroscopy" by S. Ishikawa, S. Watanabe, S. Fukuyama, G. Sato, M. Kokubun, H. Odaka, S. Saito, T. Takahashi, K. Nakazawa and T. Tanaka.

pixels owing to technical difficulties. In recent years, however, an alternative material, aluminum (Al), has been found to overcome this problem (Toyama et al. 2004, 2005). With an Al/CdTe/Pt configuration, anodes can be successfully divided into pixels or strips and an energy resolution as low as $\sim$ 1 keV (FWHM) can be achieved at $\lesssim$ 100 keV photons (Watanabe et al. 2007; Ishikawa et al. 2007; Meuris et al. 2008).

Opposite to DSSDs, the energy resolution of a double-sided Al/CdTe/Pt strip detector is almost the same for both sides of electrodes, due to the same geometrical configurations of anodes and cathodes. This enables us, by using signals from both anodes and cathodes for each photon, to improve the spectral performance as described in the next subsection.

For the FOXSI-2 mission, we plan to change Si with CdTe as a material of focal plane detectors. We have developed prototypes of double-sided CdTe strip detectors, and measured their performances.

8.3.2 The performances of prototypes

We developed prototypes of double-sided CdTe strip detectors and evaluate performances to determine whether CdTe could be achieve the required performances. First, we developed the detector with 2.56 cm $\times$ 2.56 cm in effective area and 64 strips for each electrode, and evaluated an imaging capability. Based on the first detector, we also developed the detector with smaller size to improve a spectral performance. The size of the smaller detector is 1.28 cm $\times$ 1.28 cm in effective area, contains 32 strips for the anode and cathode. Fig. 8.12 shows a photo of the large detector. For both detectors, the strip pitch, which corresponds to the position resolution, is 400 μm. The thickness of the detectors is 0.5 mm. Guard ring electrodes 1 mm wide are implemented on both sides to reduce the leakage current (Nakazawa et al. 2004). The guard rings are kept at the same electric potential as the strips on either side of the detector.

To read out the detectors, 32/64-channel analog ASICs, VA32TAs/VA64TAs are used. VA32TA/VA64TA is a former version of VATA451, and the architecture of analog circuits are basically the same. However, the noise performance is worse than

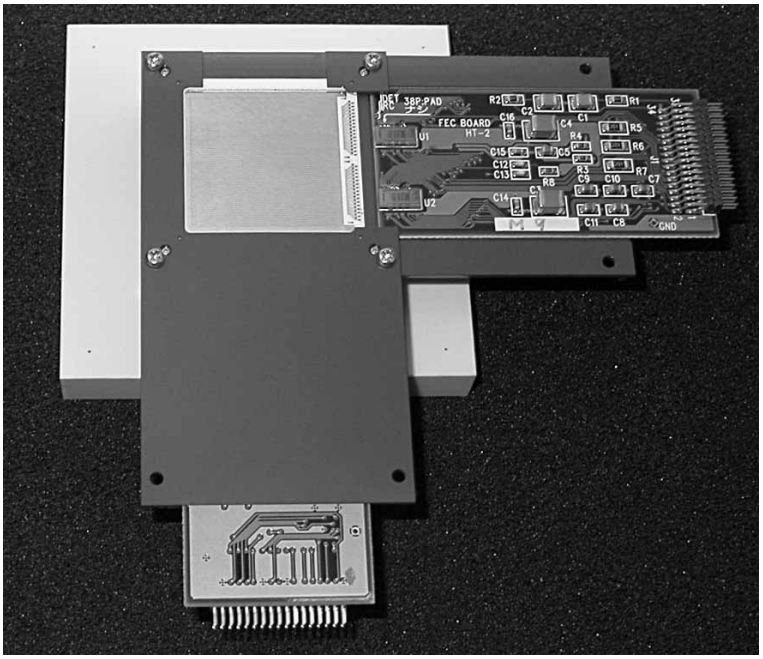

Figure 8.12 Photo of a double-sided CdTe strip detector. The effective area of the detector is 2.56 cm $\times$ 2.56 cm, and the strip pitch is 400 μm.

that of VATA451, and the ADC function is not included in the ASIC. We used VA32TA/VA64TA only because the detectors are just prototypes, and we intend to use VATA451 for detectors for *FOXSI* in the future. Contrary to DSSDs, it is impossible to wire-bond directly to the electrode of CdTe to connect the detectors to ASICs. The performance of CdTe would become worse because of a pressure and heat. To connect electrically from strips to ASIC, a stud-bump method is adopted for both the anode and cathode strips. By using needle shaped soft metals of gold and indium as a stud, CdTe can be connect to a read out system without excessive stress.

We successfully operated the large detector with 2.56 $\times$ 2.56 cm effective area under a temperature of -20 °C and a bias voltage of 500 V. The enery resolutions were measured to be 2.6 and 6.3 keV at 60 keV for the cathode and anode. The energy resolution is worse than expected, mainly because the leakage current is higher than expected. For anode signals, the leakage current tolerance of VA64TA is low, and the resolution could become even worse as the leakage current increases.

To evaluate a imaging performance, we obtained a shadow image using a nut, washer and solder, shown in 8.3.2, at several γ-ray peaks of radio isotopes. The used γ-ray peaks are 31, 60, 81 and 122 keV, from sources of ^{133}Ba, ^{241}Am and ^{57}Co. 62 out of 64 strips of the cathode and 61 out of 64 strips for the anode were used for the images. Signals from the two edge strips of each anode and cathode neighboring the guard-ring are noisy and not included for the analysis. A single strip shows no signal ('white line in Fig. 8.3.2), probably because it is not connected to the ASIC. Note that the washer (largest diameter) is thinner than the nuts, and therefore does not appear in the 122 keV image. Images of each energy are obtained and the imaging capability with a position resolution of 400 μm was successfully shown.

To improve a spectral performance, we developed and measured performances of the 1.28 cm size detector. The spectral performance of the small detector was measured using a ^{241}Am radioactive isotope source peaking at 60 keV. The operating temperature was -20 °C and the applied bias voltage was 500 V. The spectra from the anode and cathode strips are shown in Fig. 8.14. The anode spectrum was the sum of signals from 30 of 32 strips, while the cathode spectrum was from all 32 strips.

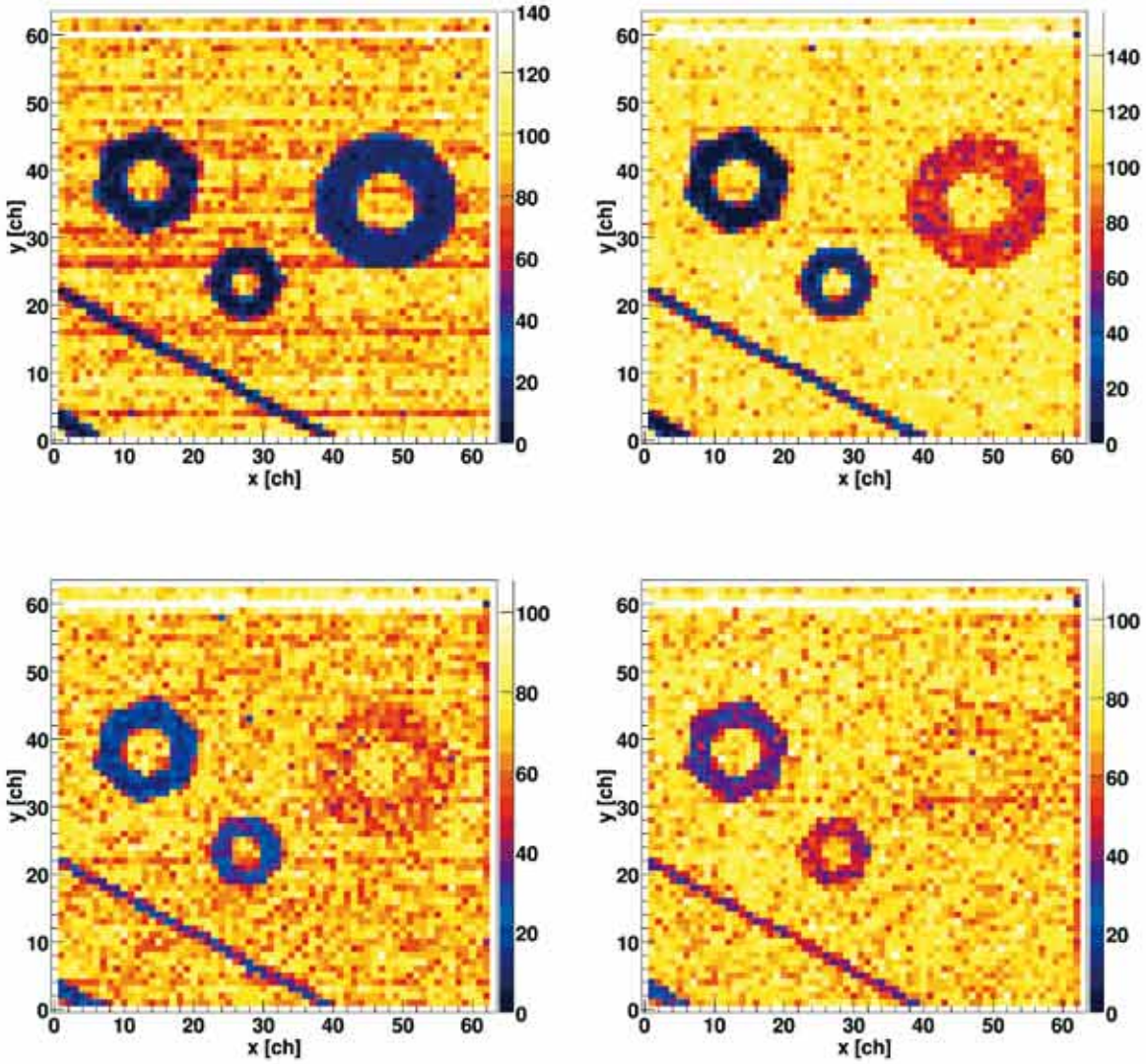

Figure 8.13 The shadow image of a nut, washer and solder obtained by the 400 μm pitch double-sided CdTe strip detector. (*Top Left*) 31 keV(^{133}Ba), (*Top Right*)60 keV(^{241}Am), (*Bottom Left*)81 keV(^{133}Ba) and (*Bottom Right*)122 keV(^{57}Co).

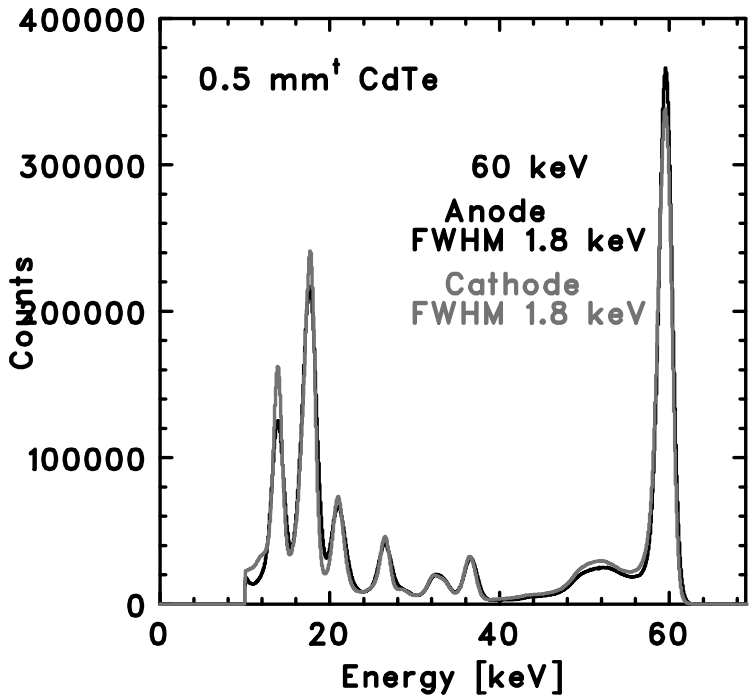

Figure 8.14 Spectra of the ^{241}Am radioactive isotope obtained by a CdTe detector, 0.5 mm thick. The detector temperature was $-20°$ C, and the bias voltage was 500 V. The energy resolution (FWHM) for both anodes and cathodes was measured to be 1.8 keV at 60 keV.

Two edge anode strips, close to the guard ring, had high noise and thus were excluded from the spectrum. The measured energy resolution was 1.8 keV (FWHM) for both electrodes, significantly improved.

When a high bias voltage ($\gtrsim$ 500 V) is applied to thin devices ($\sim$0.5 mm), the charge collection efficiency is so high that almost no low-energy tail appears for γ-ray peaks of $\lesssim$100 keV. Under such conditions, the origin of the energy resolution deterioration is mainly electrical noise that is independent of the anode and the cathode. Therefore, signals from the anode and cathode can be regarded as multisampling of the same charges, and we can estimate the incident photon energy precisely through a linear combination of signals from each electrode (Lund et al. 1996). In this case, the energy resolutions are the same for the anode and the cathode; thus we reconstructed the spectrum by averaging signals for each photon as

$$E = \frac{E_{anode} + E_{cathode}}{2}, \tag{8.1}$$

where E is the estimated energy of incident photons, and E_{anode} and $E_{cathode}$ are normalized signal pulse heights from the anode and the cathode, respectively (Watanabe et al. 2009). If the noises from the anode and cathode are completely independent, the spectral performance can be improved by a factor of $\sqrt{2}$. Figure 8.15 shows a reconstructed spectrum using this method. The energy resolution is improved to 1.5 keV (FWHM), by a factor of 1.2. The nonuniformity of charge collection efficiency is considered to remain, which may explain why this improvement is smaller than expected.

We have shown that double-sided CdTe strip detectors can achieve efficiencies and energy resolutions simultaneously. In the next step, we plan to develop and evaluate a detector with a fine strip pitch (60 μm for *FOXSI* 2) to meet the requirement of spatial resolution for the mission. For smaller strips, capacitance and leakage current is expected to be lower. By using such a detector and VATA451, better spectral performances as the *FOXSI* requirement of $\sim$1 keV resolution can be expected.

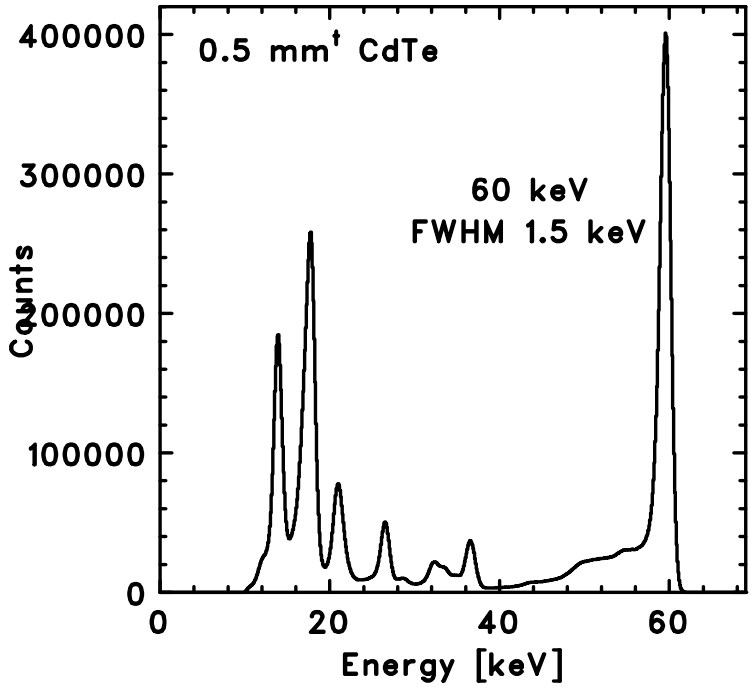

Figure 8.15 Reconstructed spectrum of a ^{241}Am radioactive isotope from a linear combination of anode and cathode signals. The resulting improved energy resolution (FWHM) is 1.5 keV at 60 keV.

Chapter 9

Conclusion

We studied particle acceleration in solar flares through HXR observations by *RHESSI*. We also discussed the requirements for future observational studies of particle acceleration in solar flares, and we developed detectors that meet these requirements.

Using *RHESSI* rear segment data, we analysed flare-integrated images of all *RHESSI* γ-ray flares with high enough counting statistics in the energy band from 150 keV to 450 keV. Out of the 26 *RHESSI* γ-ray flares, we successfully obtained images for 21 events. The remaining 8 events have >300 keV fluences of less than a few hundred photons/cm^2 and counting statistics are too poor for detailed imaging. We found the followings:

- The intensity ratios of footpoints at 50-100 keV and 150-450 keV are found to be similar. This indicates that relativistic electrons penetrate at both ends of the flare loop at similar rates. Hence, transport effects from a coronal acceleration site appear to be similar for semi-relativistic electrons producing the 50 keV emission as for relativistic electrons producing the >150 keV emission.

- There is no obvious correlation between the footpoint separation and the ratio of 2.2 MeV to >300 keV fluence. Hence, the relative acceleration efficiency of electrons and protons does not depend on flare loop length. Such a correlation is proposed to be an indicator for stochastic acceleration models. However,

not finding a correlation could also simply be because the spatial scale of the acceleration site does not scale with the loop length.

- Coronal γ-ray sources are only seen for the three events with best counting statistics. However, the absence of coronal sources for the other events could be due to observational limitations.

While the *RHESSI* imaging concept has been proven to successfully work in the γ-ray range, the limited counts available for most of the detected events makes it possible to obtain flare-integrated images only for the few largest events. To make a breakthrough from the observational side, the sensitivity of a future instrument needs to be improved significantly, preferably by two orders of magnitude.

Good examples of above-the-loop-top sources similar to the Masuda flare are rare even in the extensive *RHESSI* data base. Nevertheless, *RHESSI* observations clearly confirm the existence of this type of source. We report on the currently best example of a *RHESSI* flare that resembles the Masuda flare geometry. *RHESSI*'s imaging spectroscopy capability allows us to study the timing and energetics of the above-the-loop-top source relative to the footpoints with much better accuracy than before. The above-the-loop-top source is observed to peak $\sim$8 s earlier than the footpoint sources and decays afterwards while the footpoint source stays bright. This suggests that the above-the-loop-top source provides the precipitating electrons that feed the footpoint source. To make a more quantitative comparison we estimate the number of non-thermal electrons in the above-the-loop-top source and compare this to the needed precipitation rate of non-thermal electrons to produce the hard X-ray emission in footpoint source. The largest uncertainty in this derivation is introduced by the unknown fraction of occulted hard X-ray footpoint emission. However, assuming that half the emission is occulted, the time scale to empty out the above-the-loop-top source is of the same order of magnitude as the duration of the footpoint emission. Hence, there are enough electrons within the above-the-loop-top source to account for the footpoint emission. We therefore put forward the following scenario: Magnetic energy release within the above-the-loop-top source produces a bulk energization and accelerates all electrons to energies of tens of keV, and electrons escaping the above-

the-loop-top source then produce the footpoint emission. Both the acceleration and the escape mechanism are currently not understood. The interplay between acceleration efficiency and escape probability are important parameters for the creation of an above-the-loop-top source. If the escape probability is large compared to the acceleration efficiency, a bulk energization does not happen as accelerated electrons precipitate too quickly. Hence, the rare cases where we observe above-the-loop-top sources could be events where the escape probability is low (e.g., trapping of accelerated electrons within the acceleration region is efficient) compared to the acceleration efficiency.

To observe energetic electrons in the loop top site as they are accelerated, travel through the corona, and while in the presence of high intensity flare footpoints, higher dynamic range and sensitivity are demanded. *Yohkoh*/HXT and *RHESSI* have made use of non-focusing imaging techniques such as RMC imaging technique to provide HXR imaging spectroscopy. Non-focusing imaging observations are limited by low dynamic range and high background due to large detector volume. To improve the dynamic range for future observations, grazing-incidence HXR focusing optics are a promising new technology for future solar observations. By using focusing optics, arrival directions of incident photons can be determined directly, and image reconstructions, which are required and limit dynamic range of RMCs, are not necessary. Furthermore, focusing enables the use of small focal plane detectors while retaining large effective area, which imply a drastic reduction in non-solar background thereby increasing the sensitivity to solar HXR emissions. For future observations of the solar corona using high dynamic range and sensitivity, we developed prototypes of focal plane detectors of HXR focusing optics for the *FOXSI* mission. *FOXSI* is the first solar observation mission using HXR focusing optics. Fine-pitch semiconductor detectors with a front-end ASIC will fulfill the scientific requirements of spatial and energy resolution, low energy threshold and time resolution. We designed and fabricated a DSSD with a pitch of 75 μm, which corresponds to 8 arcsec at the focal length of 2 m. We also developed a low-noise ASIC for *FOXSI*. The detector was successfully operated in the laboratory at a temperature of -20 °C and with an applied bias voltage of 300 V, and the energy resolution of 430 eV at a 14 keV line was achieved.

We also demonstrated fine-pitch imaging successfully by obtaining a shadow image, hence the implementation of scientific requirements was confirmed. To upgrade detectors to improve detector efficiency for second launch of *FOXSI* (*FOXSI* 2), we developed prototype cadmium telluride (CdTe) detectors with the double-sided strip configuration with a strip pitch of 400 μm. The detector was successfully operated under a temperature of -20°C and with an applied bias voltage of 500 V, and the concept was successfully demonstrated. A shadow image was successfully obtained, and the energy resolution of 1.5 keV at 60 keV was achieved. The improvement of energy resolution using both the anode and cathode signals was also demonstrated.

Future spacecraft observations with HXR focusing optics are required to reveal complete picture of particle acceleration in solar flares. A spacecraft enables long-duration observations, including many large flares. With HXR focusing and imaging of large flares, the non-thermal radiation from coronal sources will be observed. This will provide a significant leap in understanding the mechanisms of solar flares and particle acceleration. Within the next years, we are planning to submit a proposal for a spacecraft version of *FOXSI* that will provide unprecedented dynamic range and sensitivity.

Appendix A

Time profiles of the *RHESSI* >150 keV flares

In Fig. A.1, we show all the count rate light curves of the events with the > 300 keV detections which analyzed in Chapter 4 (selected from the list in Shih et al. 2009).

The attenuator states are shown by the blue lines. If the dead time is sufficiently low, *RHESSI* try to unset one attenuator every 4 minutes. After that, if the dead time is still low enough for the observation, the attenuator state will be kept. In case that the dead time become too high, the attenuator is set again. This attenuator operation is seen in such as the July 20, 2002 flare.

When the *RHESSI* spacecraft is in South Atlantic Anomaly (SAA), in which the density of charged particles are rather high compared to other locations in the orbit, observational data are not obtained. The passing through SAA in the light curve corresponds to the interval with the simultaneous missing of both 50-100 and 150-450 keV data, such as appeared in the November 2, 2003 flare. If the spacecraft is in the night, the Sun is not seen and only background data are detected. The spacecraft appearance and disappearance in the sunlight corresponds to the simultaneous discontinuous jump of both energy bands.

The discontinuous jump of the count rate only from the rear detectors is caused by the decimation state change of the rear segments. If the memory for the rear detectors is full, mostly by the background, one in several counts of the observational data are

stored. The effect of the change of the decimation states of the front detectors are already corrected in the shown light curves.

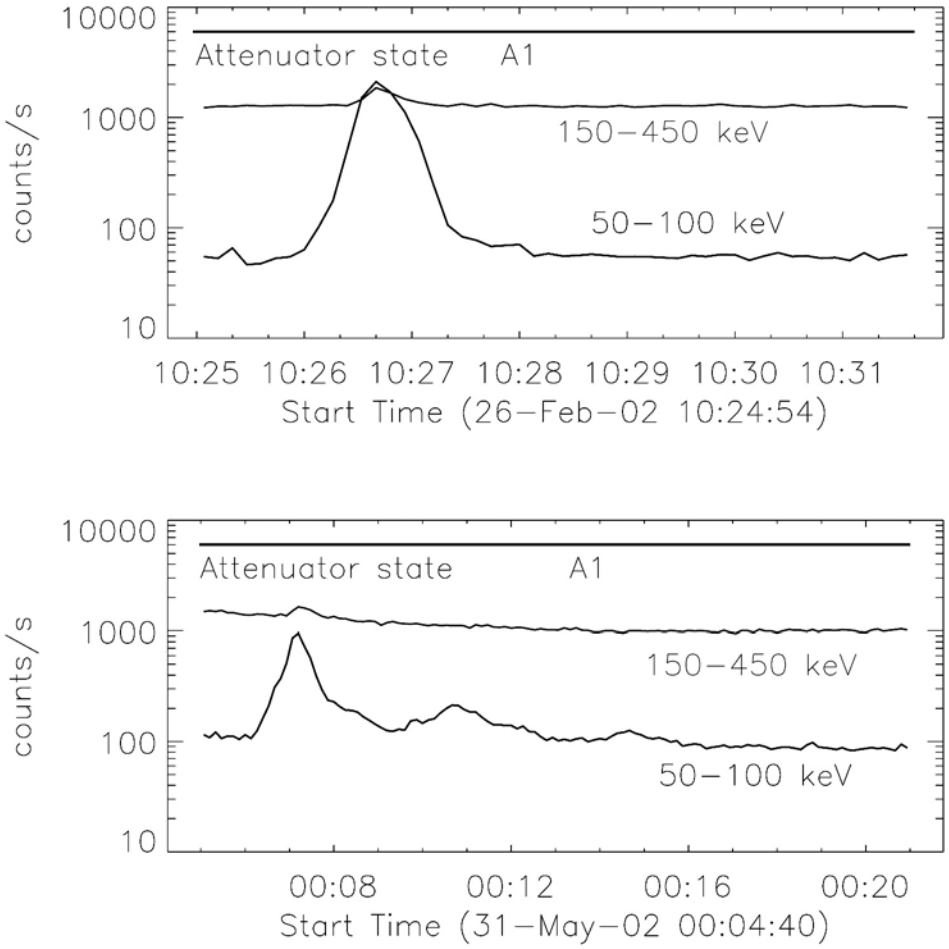

Figure A.1 50-100 (black) and 150-450 keV (red) count rate light curves of all the *RHESSI* flares with the >300 keV detections. The attenuator states are also shown (blue).

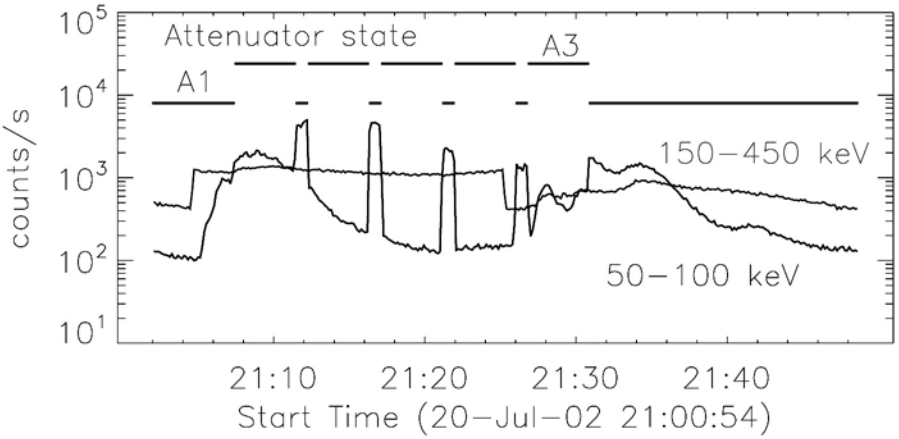

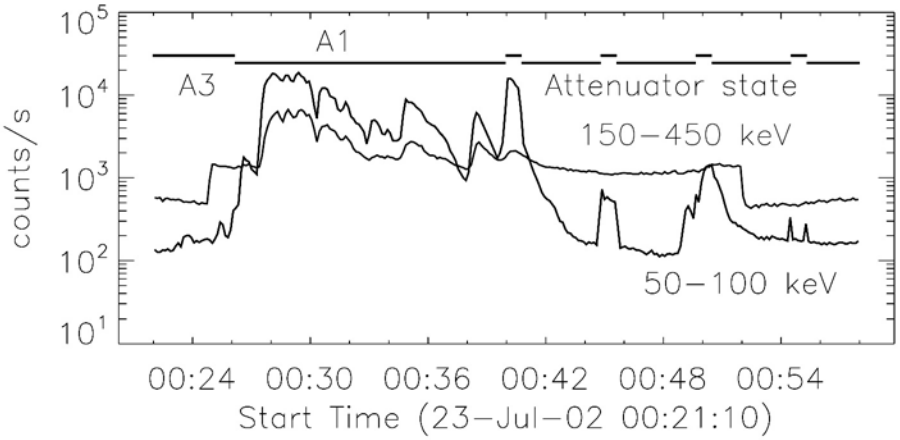

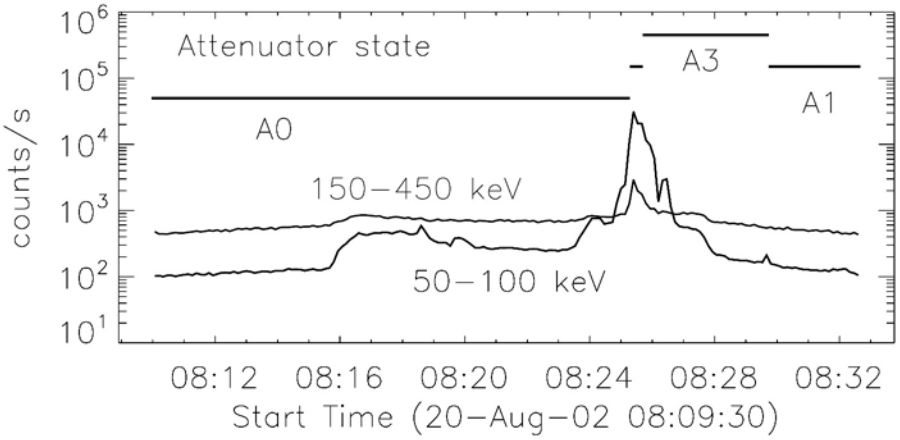

Figure A.1 *Continued.*

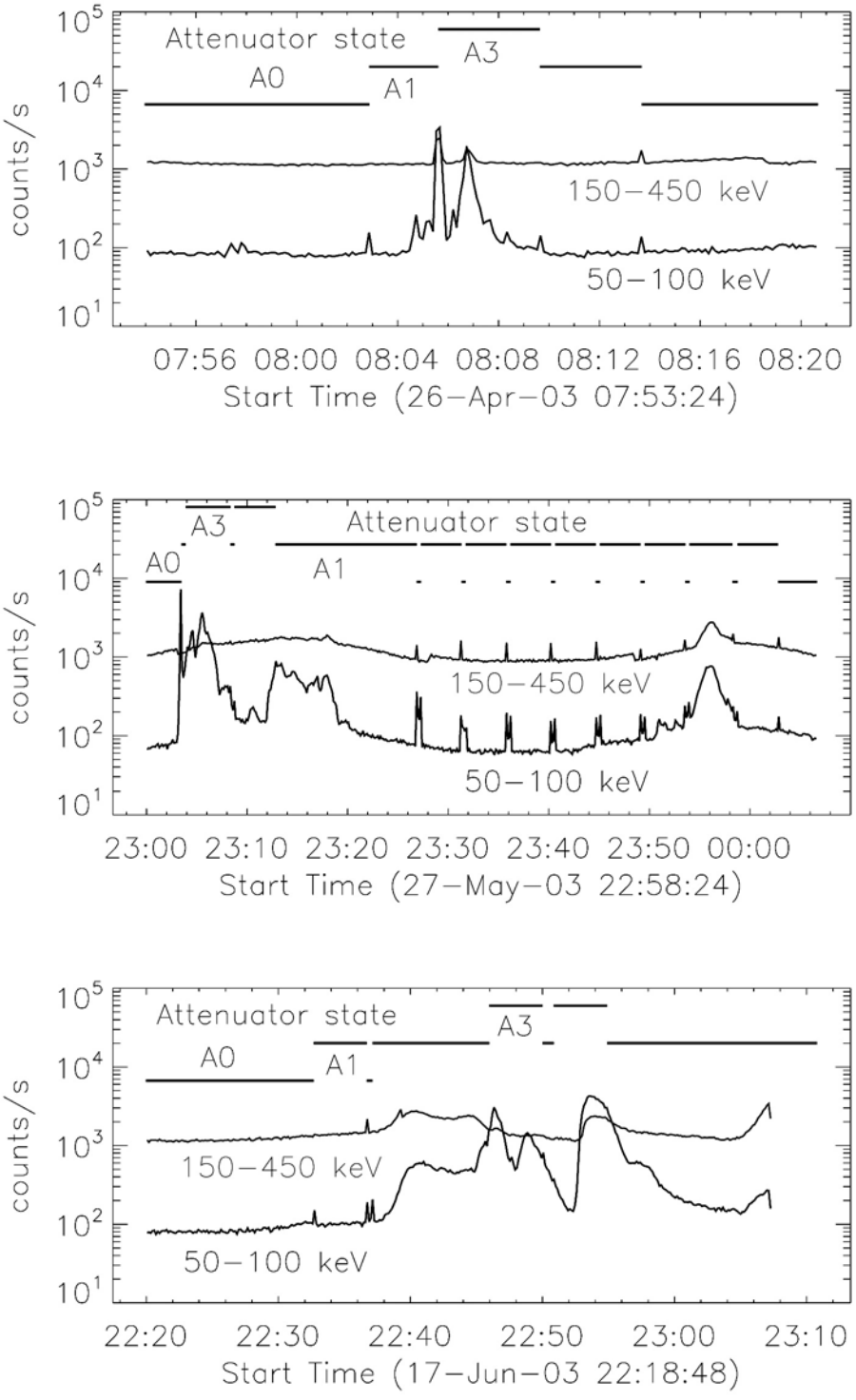

Figure A.1 *Continued.*

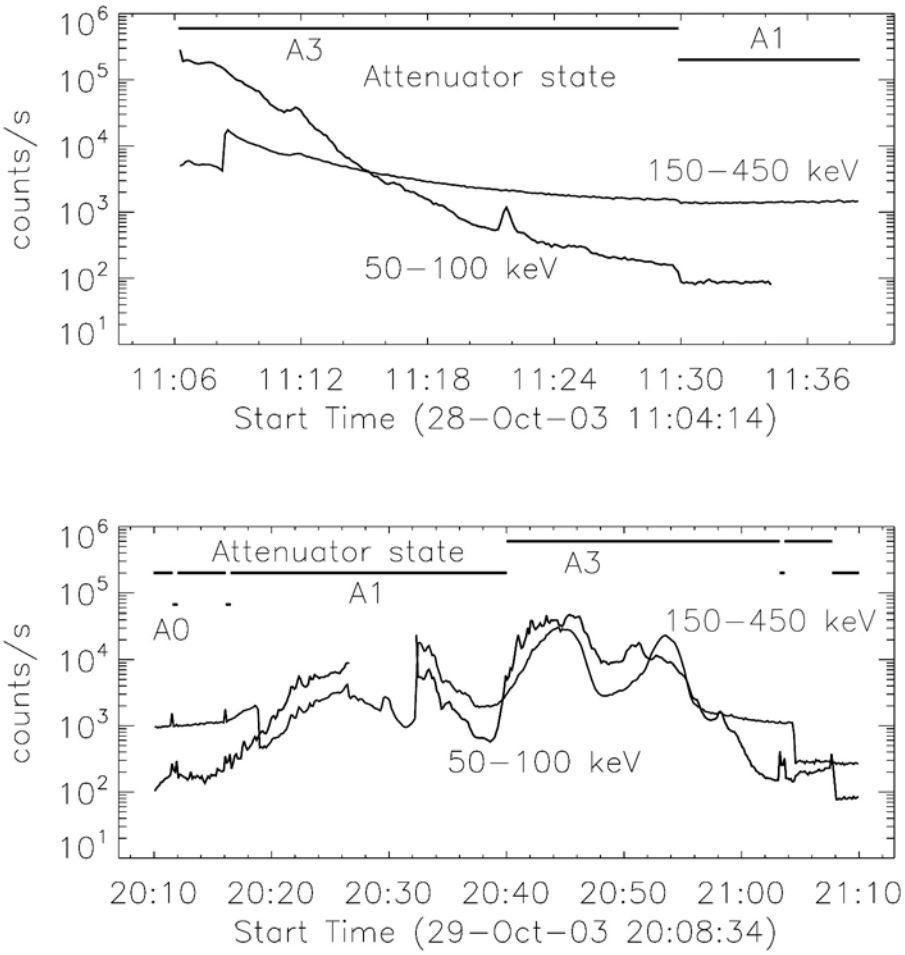

Figure A.1 *Continued.* The two later peaks in the 150-450 keV profile in the October 29 event are due to non-solar emission (particles).

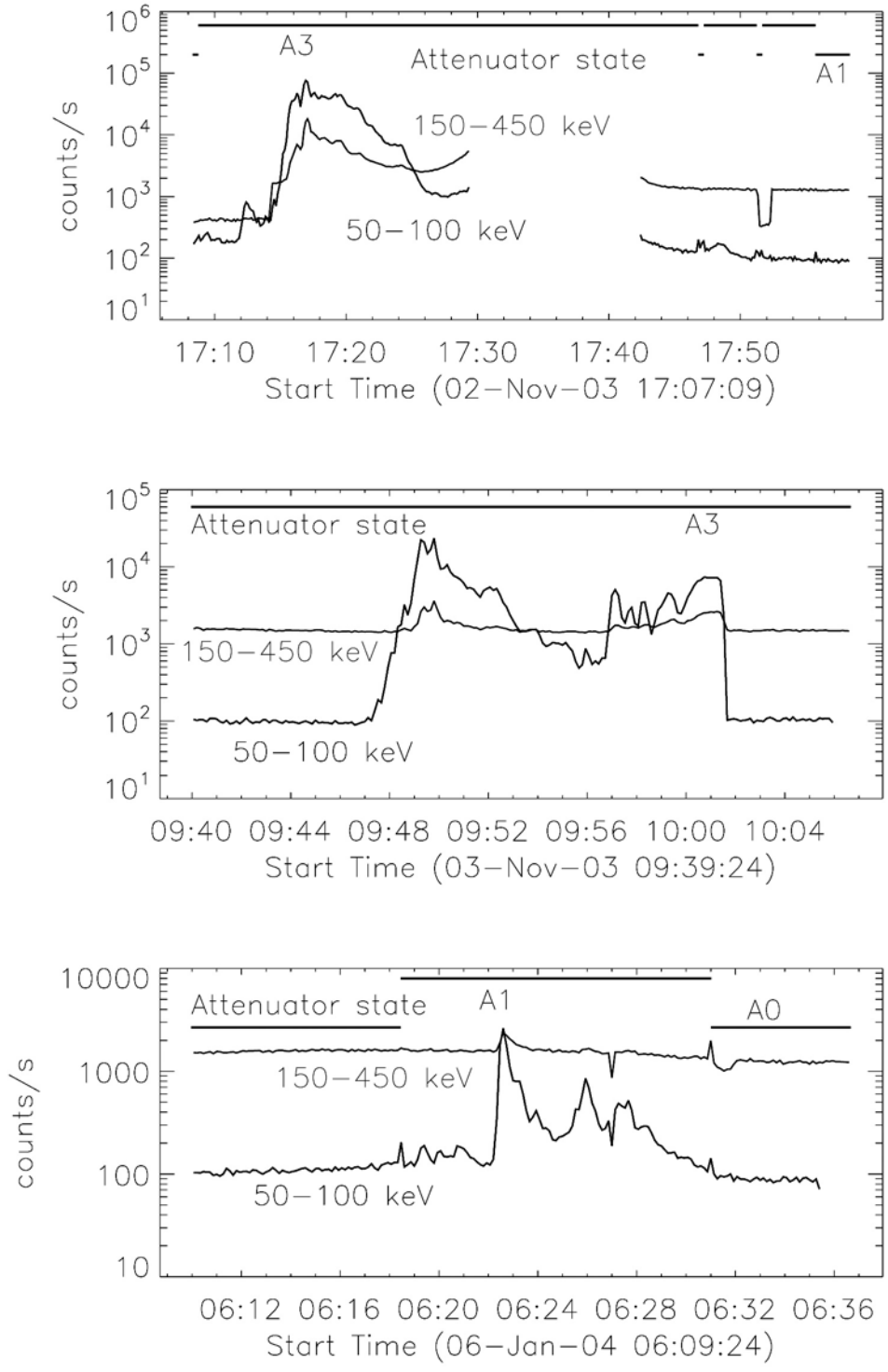

Figure A.1 *Continued.*

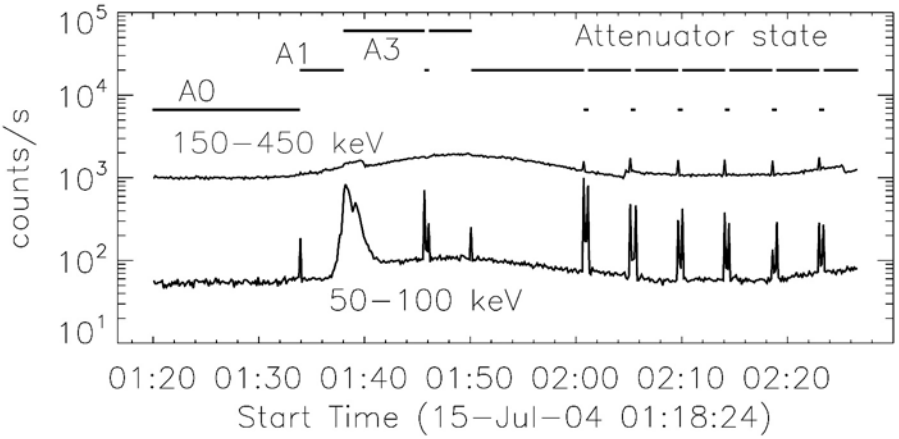

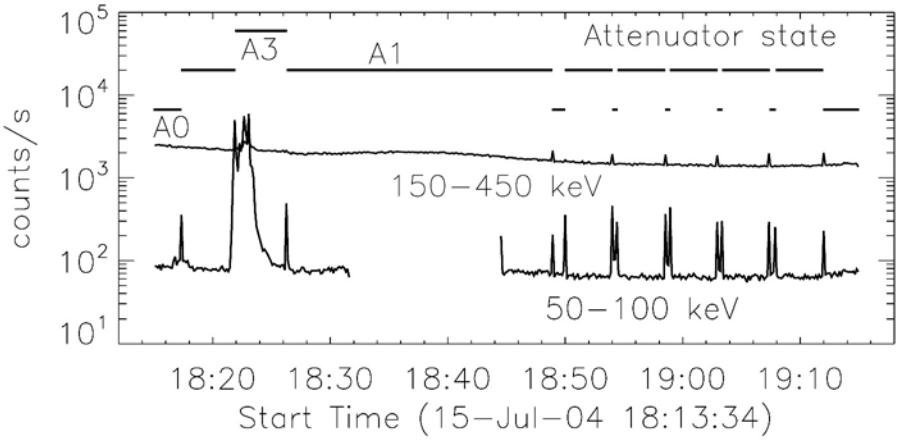

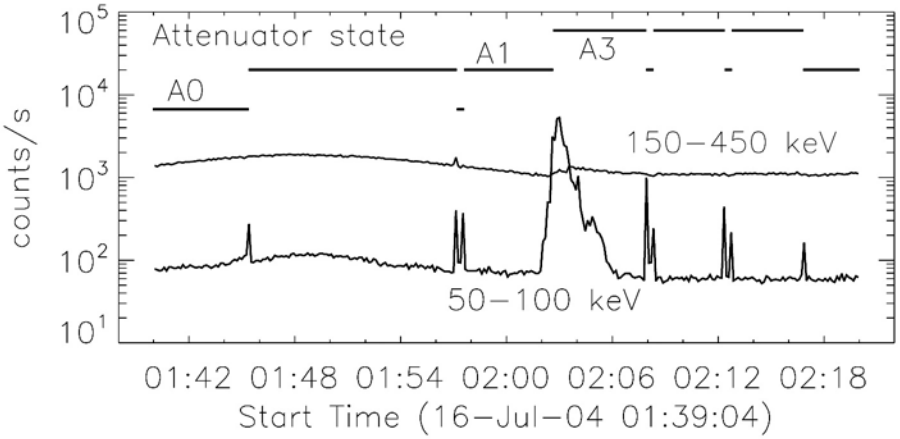

Figure A.1 *Continued.*

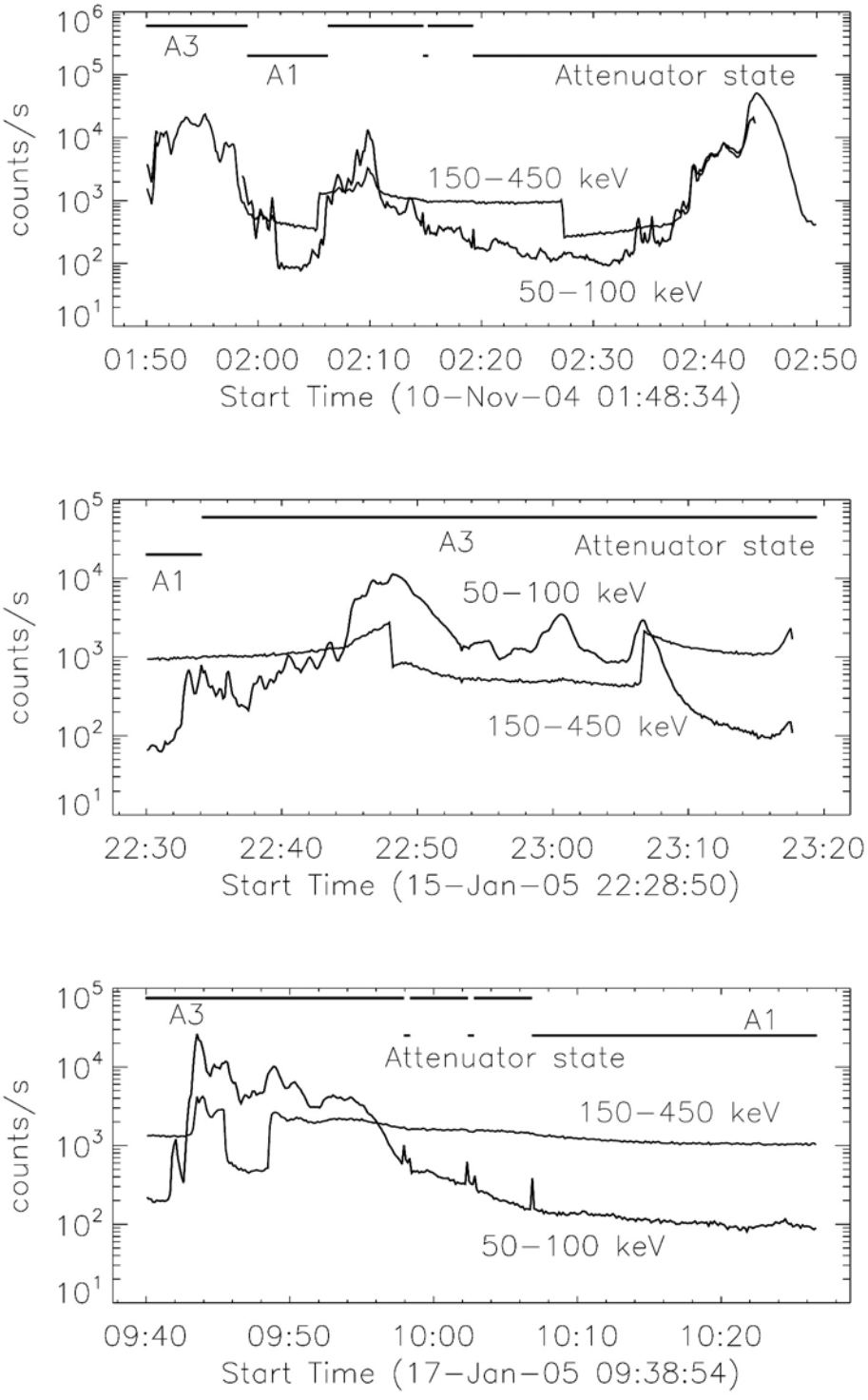

Figure A.1 *Continued.*

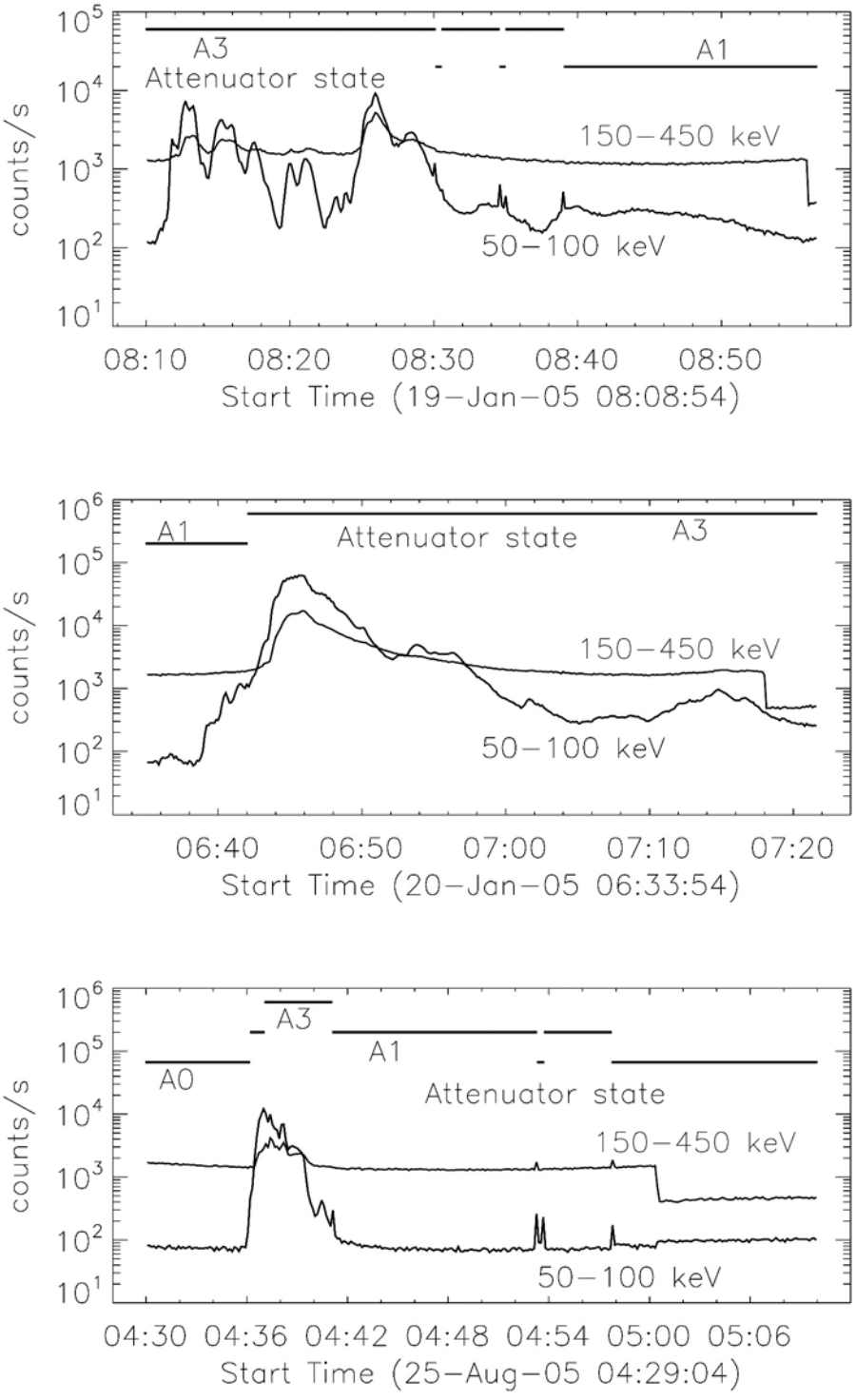

Figure A.1 *Continued.*

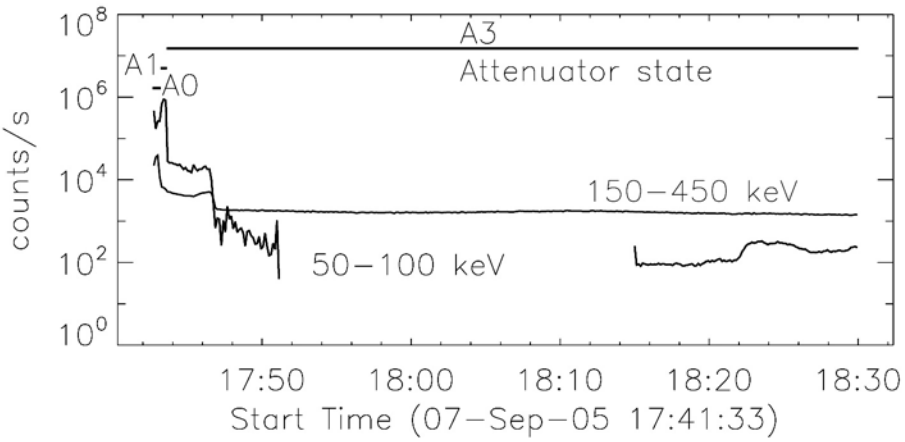

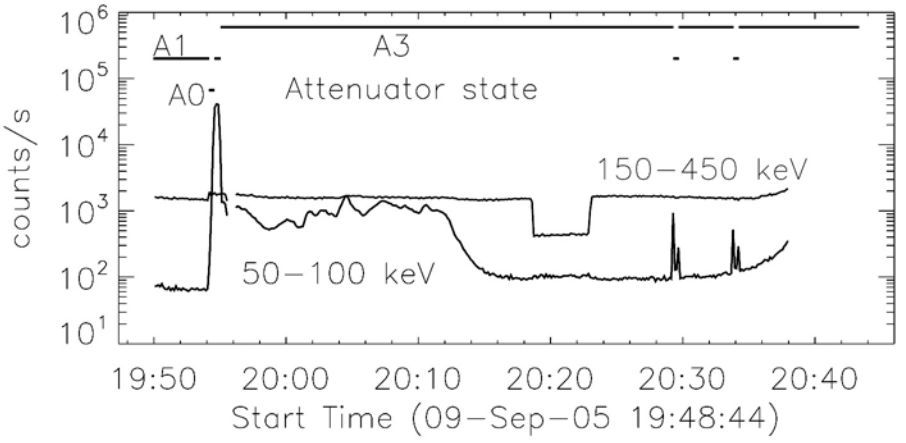

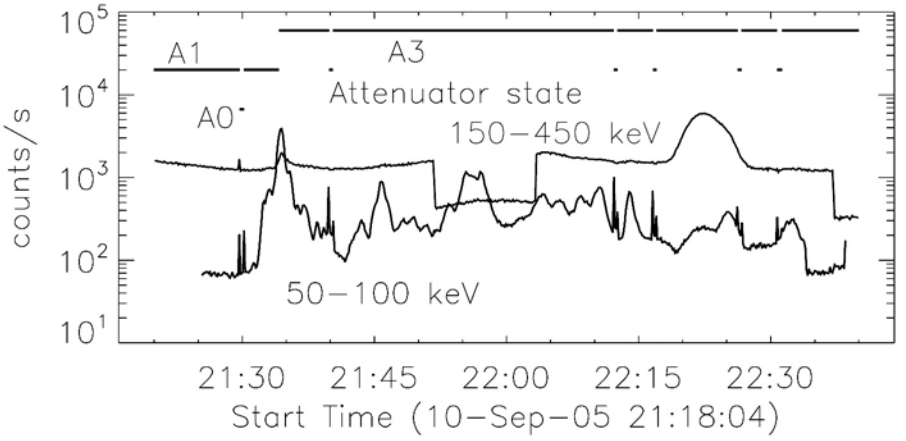

Figure A.1 *Continued.*

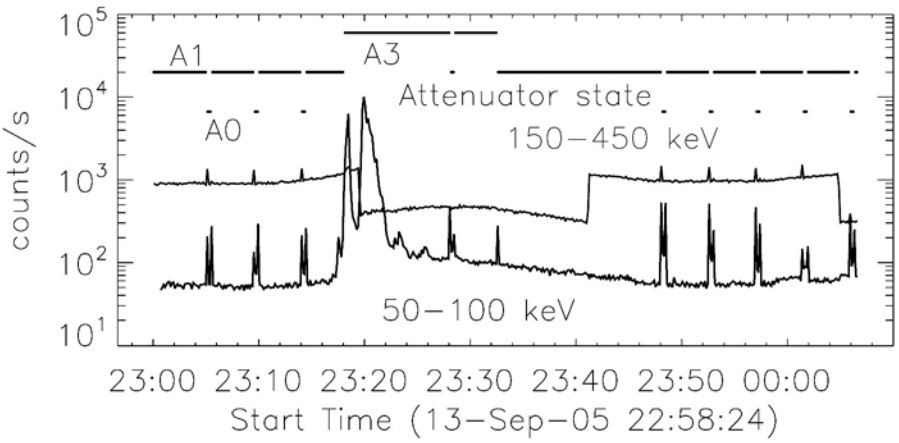

Figure A.1 *Continued.*

Appendix B

Spectroscopy of the *RHESSI* >150 keV flares

Figure. B.1 shows all the count flux spectra of the events with the > 300 keV detections which analyzed in the imaging survey of Chapter 4 (selected from the list in Shih et al. 2009). The time intervals in Table 4.1 are used to obtain the spectra. The data from both of the front and rear segments are used, and the energy band is from 3 keV to 17 MeV. Shih et al. (2009) reports the correlation between the emissions from relativistic electrons and ions in the events shown here. There is a clear correlation between >300 keV bremsstrahlung continuum and 2.223 MeV line emissions, which implies a common acceleration mechanism.

The correlation of the spectral indices at 50-100 keV and 150-450 keV obtained by these spectra are shown in Fig. B.2. The indices at 50-100 keV vary from 1.5 to 7, which is consistent with the statistical result only for the front segments (Saint-Hilaire et al. 2008). On the other hand, the photon indices 150-450 keV are rather hard, vary from 2 to 5. This could be biased, since the flare with the harder spectra at higher energies is more likely detectable in the rear segments. Between the fluxes at tow energy bands, no clear correlation is found. This is consistent with the result of *Yohkoh*, using HXT and the Gamma-ray Spectrometer (GRS) observation at above >1 MeV (Matsumoto et al. 2005).

In Matsumoto et al. (2005), the correlation between the absolute longitude and

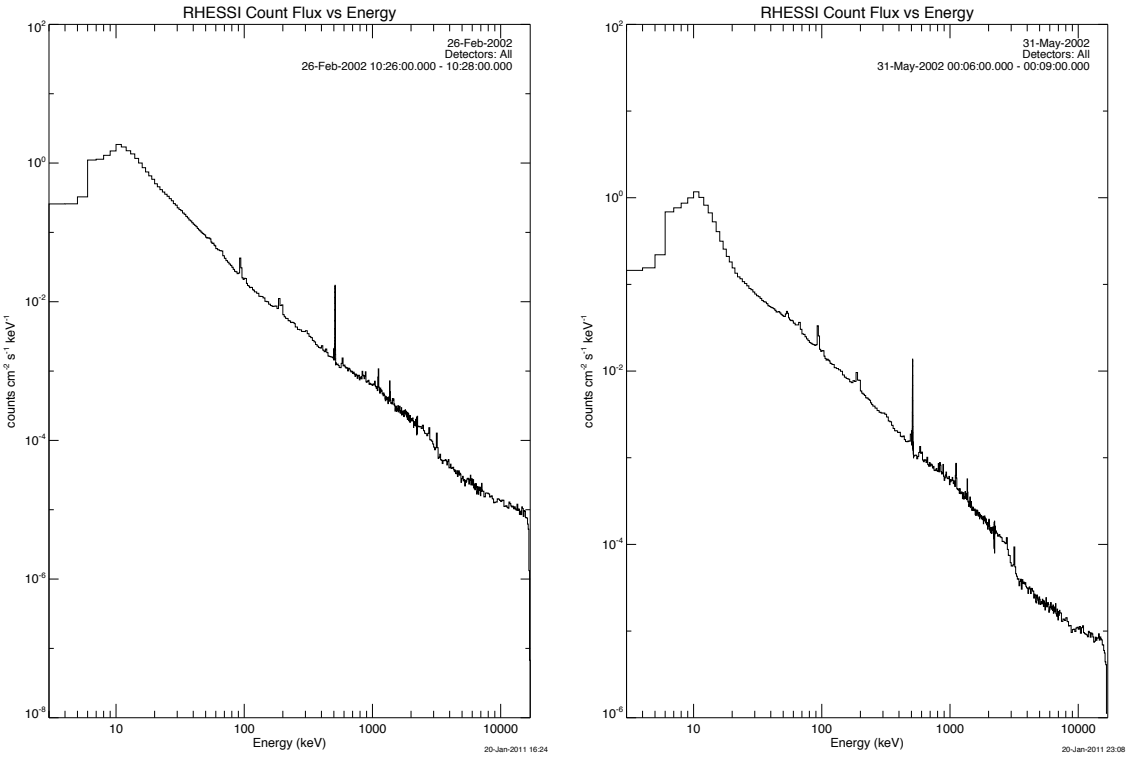

Figure B.1 Count flux spectra of all the *RHESSI* flares with >300 keV detections. The data from both the front and rear segments are used.

hardness ratio of the *Yohkoh* γ-ray flares are shown. In these events, the flares with the harder spectra are more likely to be found around the limb (at the high absolute longitudes). This relation is explained by Kotoku et al. (2007), by the effect of the Compton degradation from the relativistic beaming effect of accelerated electrons. Figure B.3 shows the similar correlations of the *RHESSI* γ-ray flares, between the absolute longitude of the events and photon indices. Both of the indices from the front segments (50-100 keV) and rear segments (150-450 keV) are not correlated with the absolute longitude. The left panel is consistent with the model of Kotoku et al. (2007), because the 50-100 keV photons do not represent the relativistic effect. Although 150-450 keV (0.6-0.8c for an electron speed) could be relativistic, higher energies may represent a clearer correlation. More events are required to investigate such correlations.

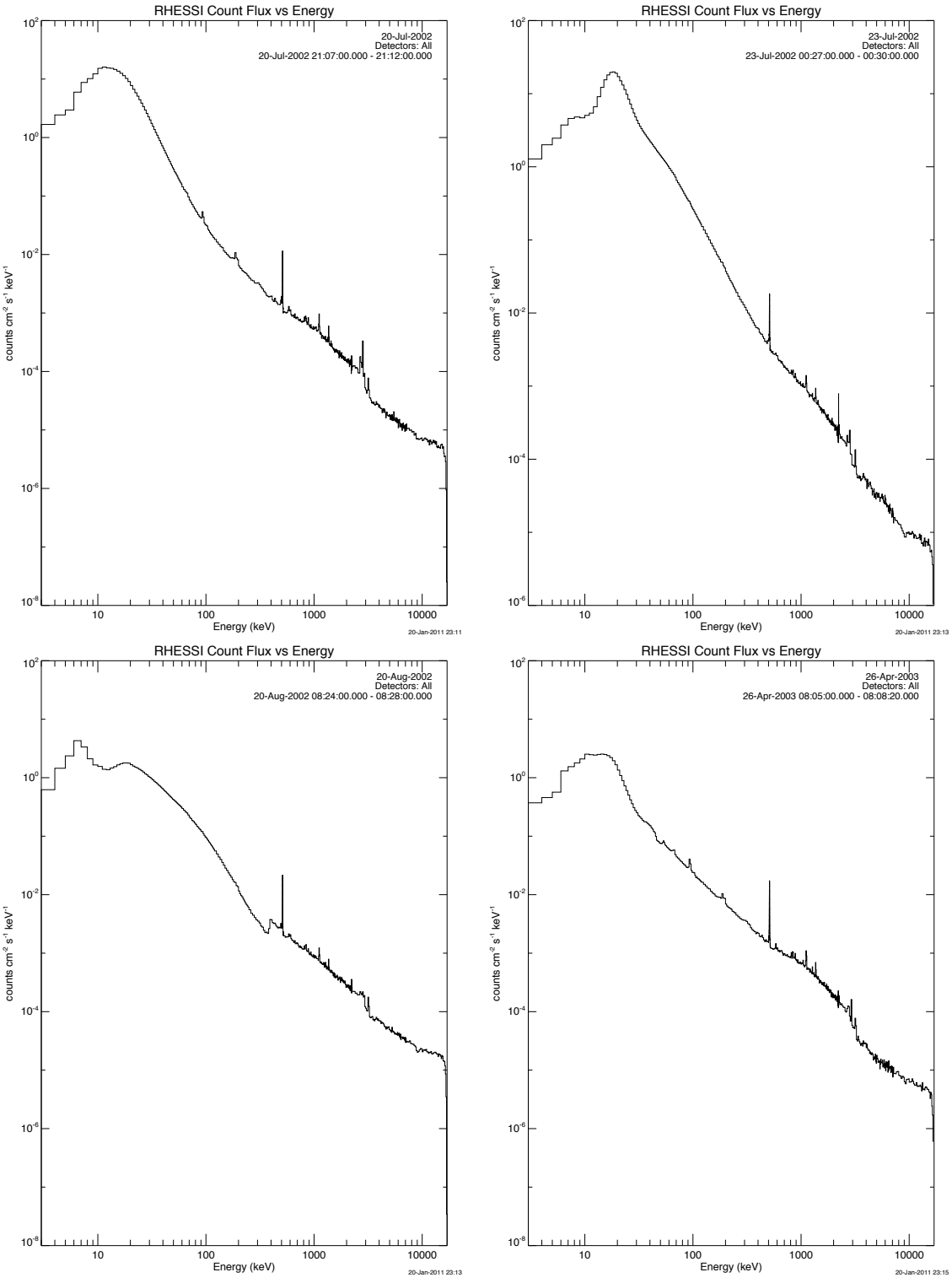

Figure B.1 *Continued.*

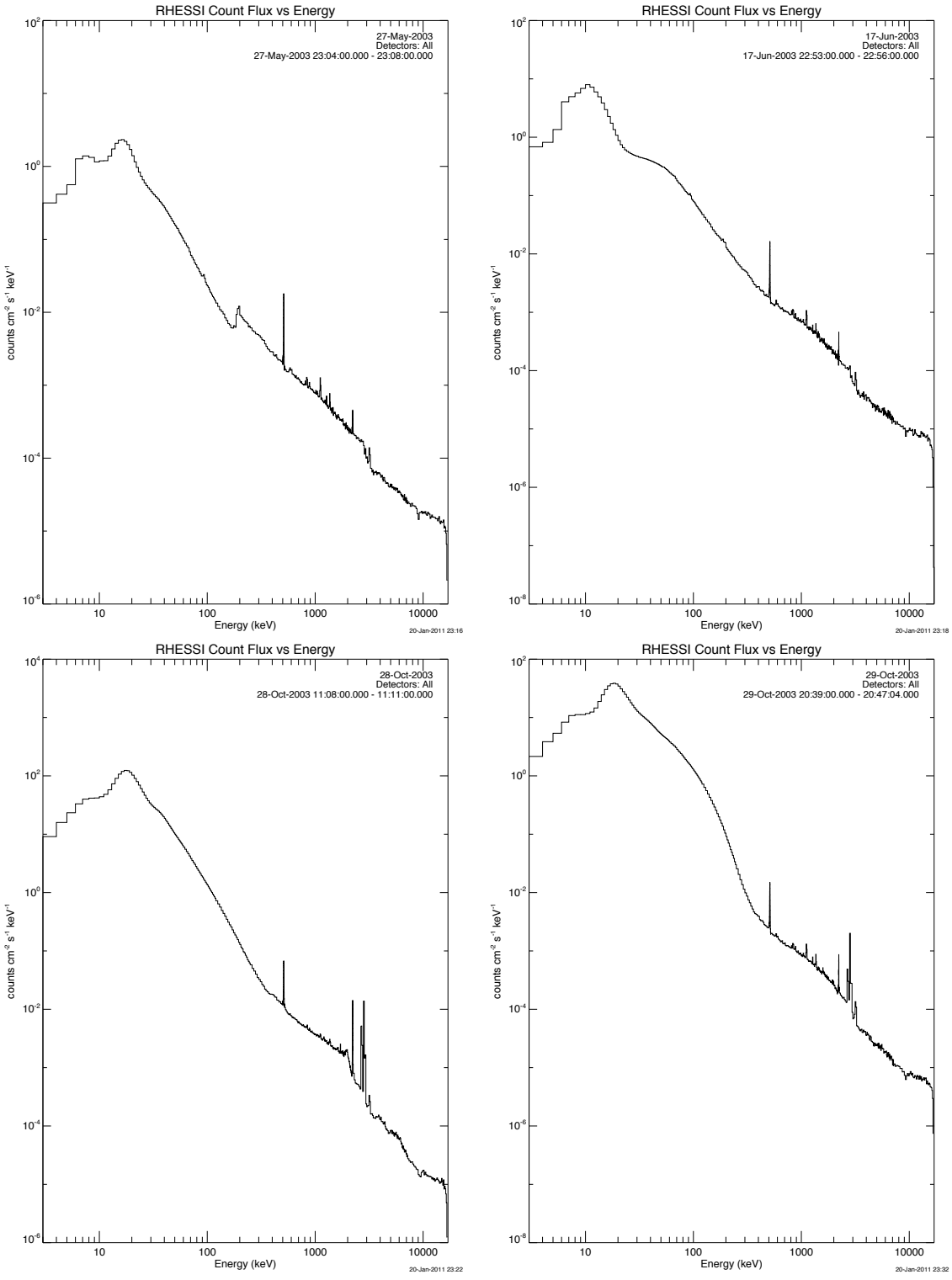

Figure B.1 *Continued.*

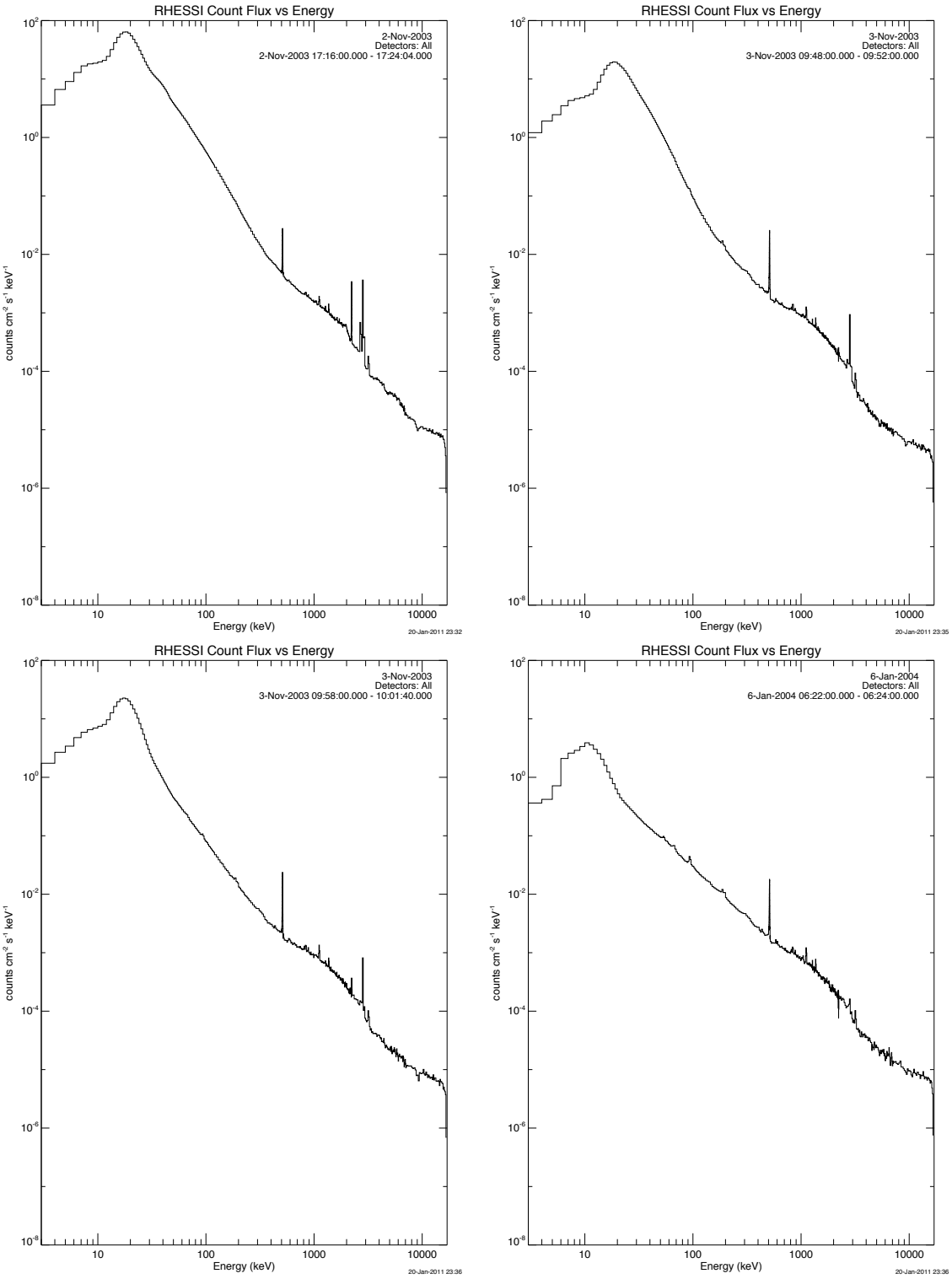

Figure B.1 *Continued.*

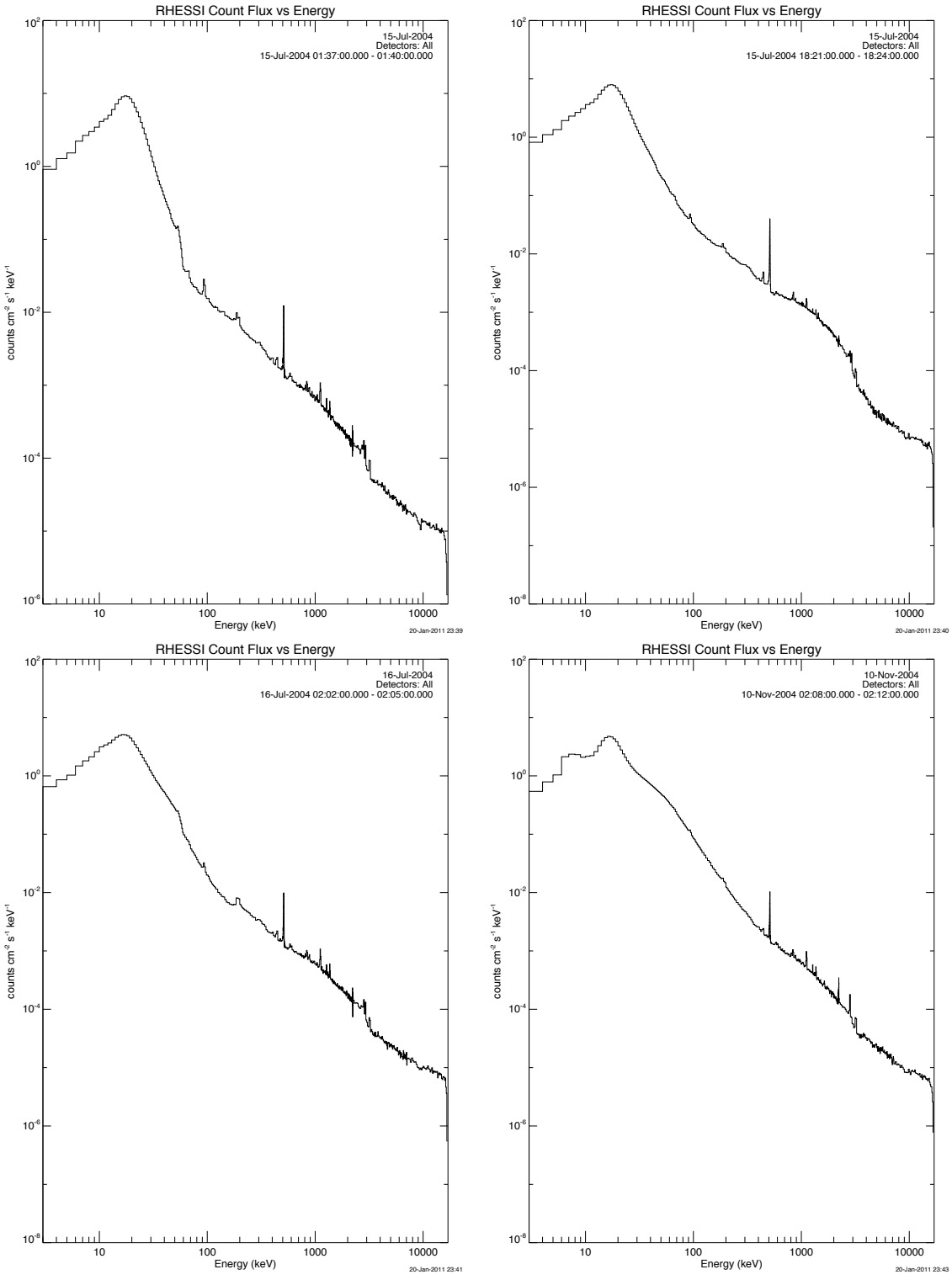

Figure B.1 *Continued.*

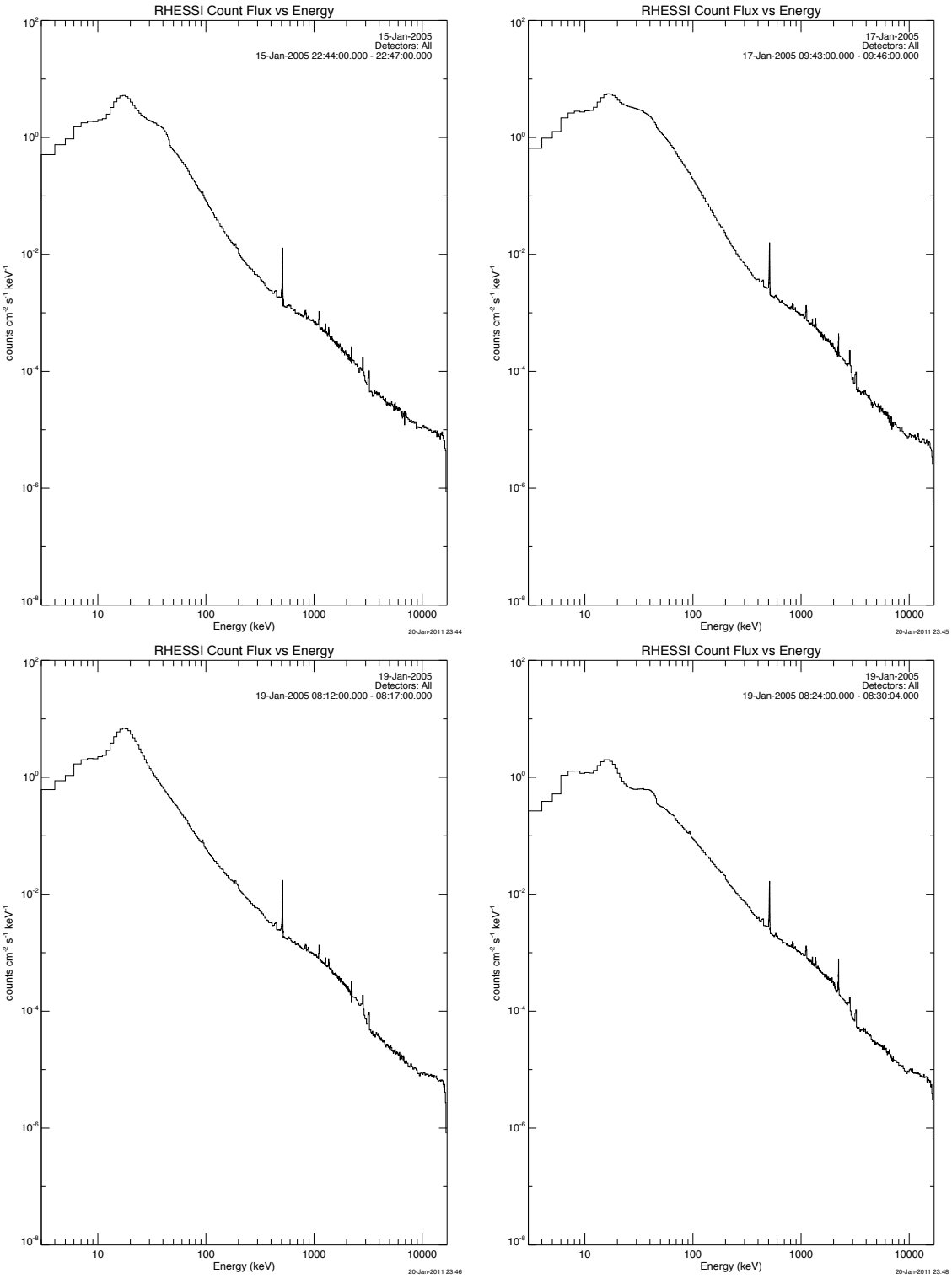

Figure B.1 *Continued.*

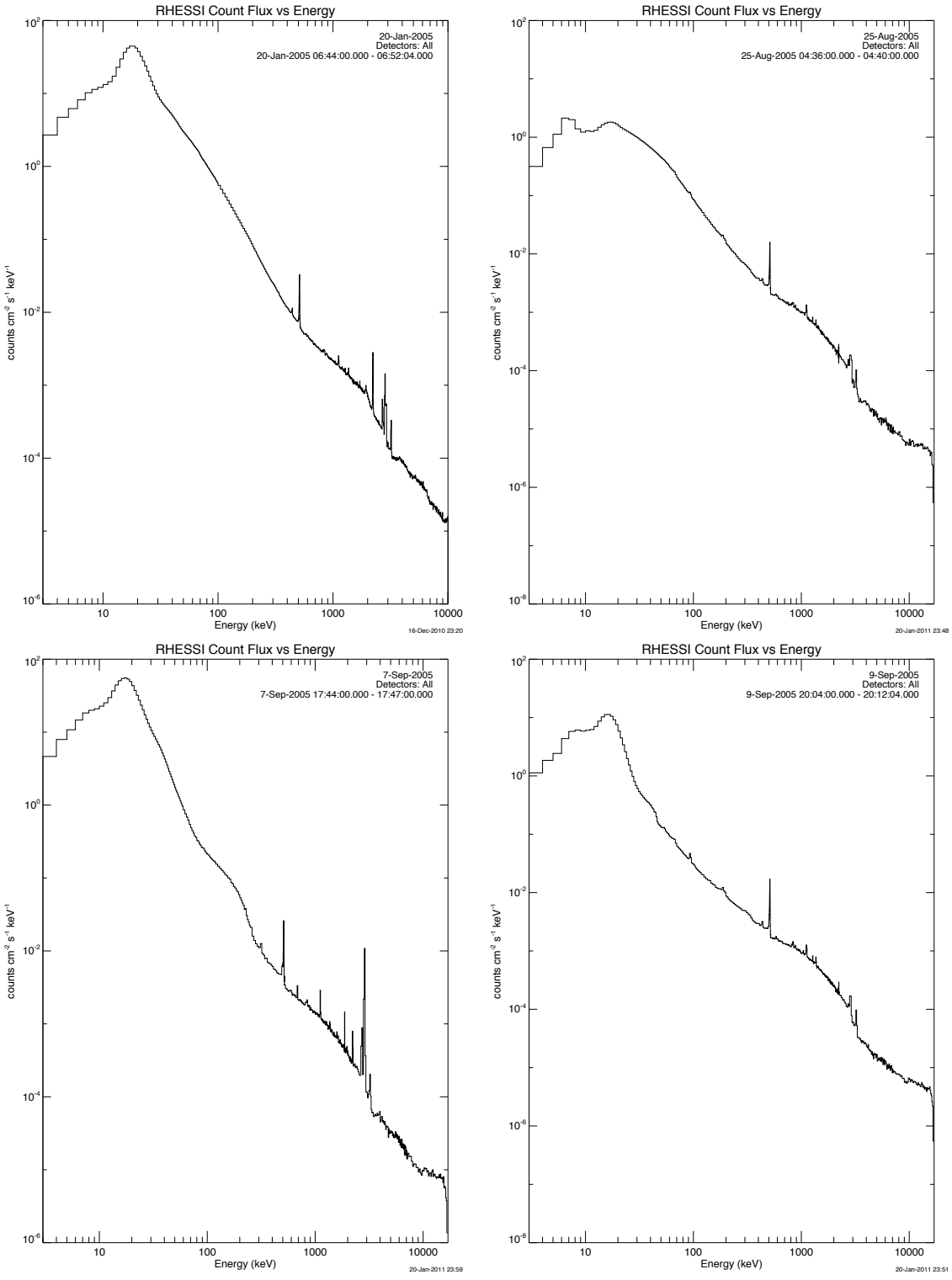

Figure B.1 *Continued.*

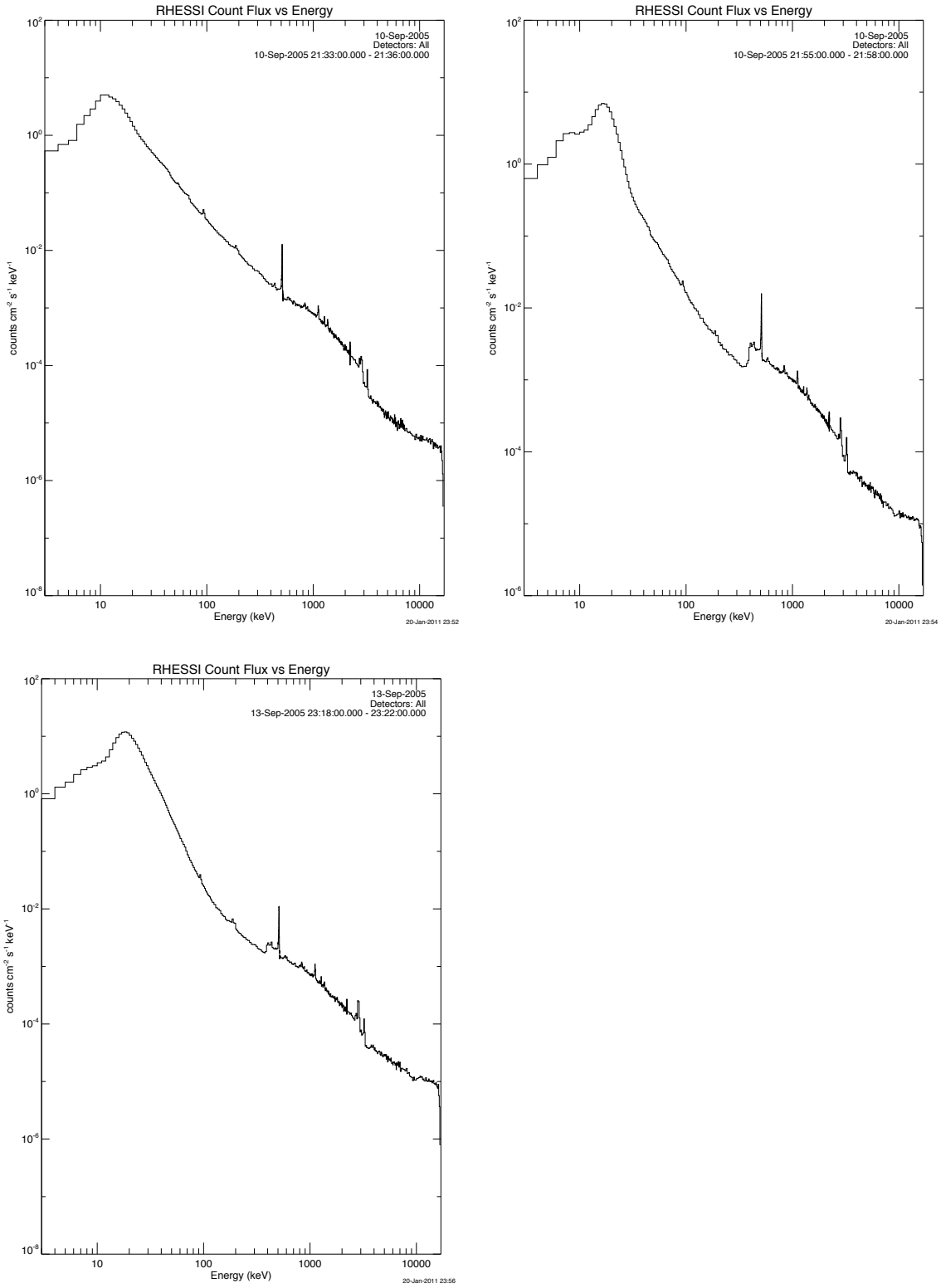

Figure B.1 *Continued.*

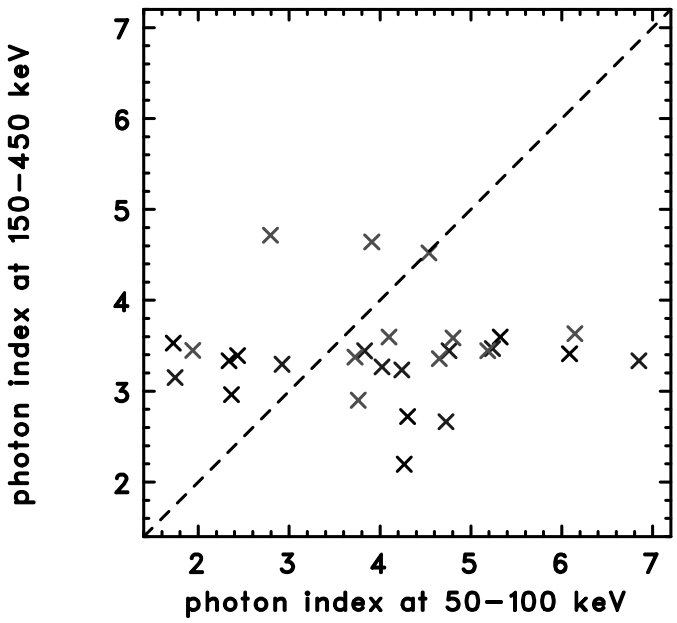

Figure B.2 Correlation of the photon indices derived at 50-100 keV and 150 450 keV. The 50-100 keV indices are obtained by the flux ratio of 50-70 keV and 70-100 keV, and the 150-450 keV indices are obtained by the flux ratio of 150-250 keV and 250-450 keV. Colored points indicate those for which a detailed image was obtained in the 150-450 keV band, as same as Fig. 4.1.

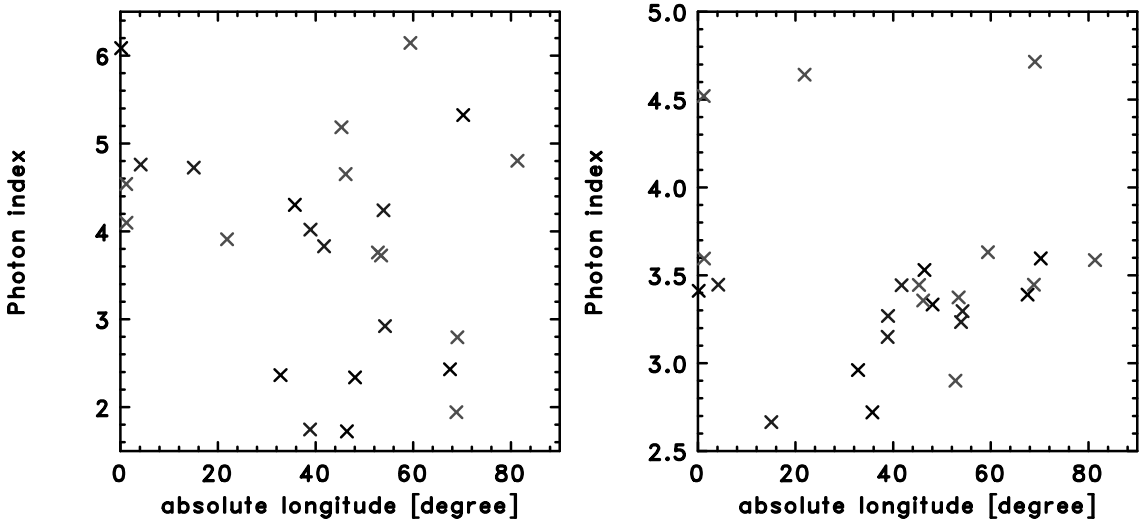

Figure B.3 Correlation of the location and spectral indices. The photon indices are derived by 50-100 keV (left) and 150-450 keV (right). Colored points indicate those for which a detailed image was obtained in the 150-450 keV band, as same as Fig. 4.1.

Bibliography

[1] M. J. Aschwanden, H. Hudson, T. Kosugi, and R. A. Schwartz, "Electron Time-of-Flight Measurements during the Masuda Flare, 1992 January 13," *ApJ*, vol. 464, pp. 985–+, 1996.

[2] M. J. Aschwanden, T. D. Tarbell, R. W. Nightingale, C. J. Schrijver, A. Title, C. C. Kankelborg, P. Martens, and H. P. Warren, "Time Variability of the "Quiet" Sun Observed with TRACE. II. Physical Parameters, Temperature Evolution, and Energetics of Extreme-Ultraviolet Nanoflares," *ApJ*, vol. 535, pp. 1047–1065, 2000.

[3] M. J. Aschwanden, *Physics of the Solar Corona. An Introduction with Problems and Solutions (2nd edition)*, M. J. Aschwanden, Ed. Springer, 2005.

[4] M. Battaglia and A. O. Benz, "Relations between concurrent hard X-ray sources in solar flares," *A&A*, vol. 456, pp. 751–760, 2006.

[5] ——, "Exploring the connection between coronal and footpoint sources in a thin-thick target solar flare model," *A&A*, vol. 466, pp. 713–716, 2007.

[6] ——, "Observational evidence for return currents in solar flare loops," *A&A*, vol. 487, pp. 337–344, 2008.

[7] W. Bencivelli, E. Bertolucci, U. Bottigli, A. D. Guerra, A. Messineo, W. R. Nelson, P. Randaccio, V. Rosso, P. Russo, and A. Stefanini, "Evaluation of elemental and compound semiconductors for X-ray digital radiography," *Nucl. Instr. Meth.*, vol. A 310, pp. 210–214, 2007.

[8] A. O. Benz and S. Krucker, "Energy Distribution of Microevents in the Quiet Solar Corona," *ApJ*, vol. 568, pp. 413–421, 2002.

[9] A. O. Benz, "Flare Observations," *Living Reviews in Solar Physics*, vol. 5, pp. 1–+, Feb. 2008.

[10] R. D. Blandford and J. P. Ostriker, "Particle acceleration by astrophysical shocks," *ApJ*, vol. 221, pp. L29–L32, 1978.

[11] J. C. Brown, "The Deduction of Energy Spectra of Non-Thermal Electrons in Flares from the Observed Dynamic Spectra of Hard X-Ray Bursts," *Sol. Phys.*, vol. 18, pp. 489–502, 1971.

[12] J. C. Brown, R. Turkmani, E. P. Kontar, A. L. MacKinnon, and L. Vlahos, "Local re-acceleration and a modified thick target model of solar flare electrons," *A&A*, vol. 508, pp. 993–1000, 2009.

[13] H. Carmichael, "A Process for Flares," *NASA Special Publication*, vol. 50, pp. 451–+, 1964.

[14] R. C. Carrington, "Description of a Singular Appearance seen in the Sun on September 1, 1859," *MNRAS*, vol. 20, pp. 13–15, 1859.

[15] S. Christe, I. G. Hannah, S. Krucker, J. McTiernan, and R. P. Lin, "RHESSI Microflare Statistics. I. Flare-Finding and Frequency Distributions," *ApJ*, vol. 677, pp. 1385–1394, 2008.

[16] N. B. Crosby, M. J. Aschwanden, and B. R. Dennis, "Frequency distributions and correlations of solar X-ray flare parameters," *Sol. Phys.*, vol. 143, pp. 275–299, 1993.

[17] J. Delaboudinière, G. E. Artzner, J. Brunaud, A. H. Gabriel, J. F. Hochedez, F. Millier, X. Y. Song, B. Au, K. P. Dere, R. A. Howard, R. Kreplin, D. J. Michels, J. D. Moses, J. M. Defise, C. Jamar, P. Rochus, J. P. Chauvineau, J. P. Marioge, R. C. Catura, J. R. Lemen, L. Shing, R. A. Stern, J. B. Gurman, W. M.

Neupert, A. Maucherat, F. Clette, P. Cugnon, and E. L. van Dessel, "EIT: Extreme-Ultraviolet Imaging Telescope for the SOHO Mission," *Sol. Phys.*, vol. 162, pp. 291–312, 1995.

[18] B. R. Dennis and R. L. Pernak, "Hard X-Ray Flare Source Sizes Measured with the Ramaty High Energy Solar Spectroscopic Imager," *ApJ*, vol. 698, pp. 2131–2143, 2009.

[19] V. Domingo, B. Fleck, and A. I. Poland, "The SOHO Mission: an Overview," *Sol. Phys.*, vol. 162, pp. 1–37, 1995.

[20] J. F. Drake, M. Swisdak, H. Che, and M. A. Shay, "Electron acceleration from contracting magnetic islands during reconnection," *Nature*, vol. 443, pp. 553–556, 2006.

[21] H. Dreicer, "Electron and Ion Runaway in a Fully Ionized Gas. I," *Physical Review*, vol. 115, pp. 238–249, 1959.

[22] A. G. Emslie, "The collisional interaction of a beam of charged particles with a hydrogen target of arbitrary ionization level," *ApJ*, vol. 224, pp. 241–246, 1978.

[23] A. G. Emslie, E. P. Kontar, S. Krucker, and R. P. Lin, "RHESSI Hard X-Ray Imaging Spectroscopy of the Large Gamma-Ray Flare of 2002 July 23," *ApJ*, vol. 595, pp. L107–L110, Oct. 2003.

[24] A. G. Emslie, J. A. Miller, and J. C. Brown, "An Explanation for the Different Locations of Electron and Ion Acceleration in Solar Flares," *ApJ*, vol. 602, pp. L69–L72, Feb. 2004.

[25] E. Fermi, "On the Origin of the Cosmic Radiation," *Physical Review*, vol. 75, pp. 1169–1174, 1949.

[26] L. Fletcher and H. S. Hudson, "Impulsive Phase Flare Energy Transport by Large-Scale Alfvén Waves and the Electron Acceleration Problem," *ApJ*, vol. 675, pp. 1645–1655, 2008.

[27] P. C. Grigis and A. O. Benz, "The spectral evolution of impulsive solar X-ray flares," *A&A*, vol. 426, pp. 1093–1101, 2004.

[28] B. N. Handy, L. W. Acton, C. C. Kankelborg, C. J. Wolfson, D. J. Akin, M. E. Bruner, R. Caravalho, R. C. Catura, R. Chevalier, D. W. Duncan, C. G. Edwards, C. N. Feinstein, S. L. Freeland, F. M. Friedlaender, C. H. Hoffmann, N. E. Hurlburt, B. K. Jurcevich, N. L. Katz, G. A. Kelly, J. R. Lemen, M. Levay, R. W. Lindgren, D. P. Mathur, S. B. Meyer, S. J. Morrison, M. D. Morrison, R. W. Nightingale, T. P. Pope, R. A. Rehse, C. J. Schrijver, R. A. Shine, L. Shing, K. T. Strong, T. D. Tarbell, A. M. Title, D. D. Torgerson, L. Golub, J. A. Bookbinder, D. Caldwell, P. N. Cheimets, W. N. Davis, E. E. Deluca, R. A. McMullen, H. P. Warren, D. Amato, R. Fisher, H. Maldonado, and C. Parkinson, "The transition region and coronal explorer," *Sol. Phys.*, vol. 187, pp. 229–260, 1999.

[29] I. G. Hannah, S. Christe, S. Krucker, G. J. Hurford, H. S. Hudson, and R. P. Lin, "RHESSI Microflare Statistics. II. X-Ray Imaging, Spectroscopy, and Energy Distributions," *ApJ*, vol. 677, pp. 704–718, 2008.

[30] F. A. Harrison, F. E. Christensen, W. Craig, C. Hailey, W. Baumgartner, C. M. H. Chen, J. Chonko, W. R. Cook, J. Koglin, K. Madsen, M. Pivavoroff, S. Boggs, and D. Smith, "Development of the HEFT and NuSTAR focusing telescopes," *ExA*, vol. 20, pp. 131–137, 2005.

[31] T. Hirayama, "Theoretical Model of Flares and Prominences. I: Evaporating Flare Model," *Sol. Phys.*, vol. 34, pp. 323–338, 1974.

[32] R. Hodgson, "On a curious Appearance seen in the Sun," *MNRAS*, vol. 20, pp. 15–16, 1859.

[33] G. D. Holman, "Acceleration of runaway electrons and Joule heating in solar flares," *ApJ*, vol. 293, pp. 584–594, 1985.

[34] H. S. Hudson, R. C. Canfield, and S. R. Kane, "Indirect estimation of energy

deposition by non-thermal electrons in solar flares," *Sol. Phys.*, vol. 60, pp. 137–142, Nov. 1978.

[35] H. S. Hudson, "Solar flares, microflares, nanoflares, and coronal heating," *Sol. Phys.*, vol. 133, pp. 357–369, 1991.

[36] G. J. Hurford, E. J. Schmahl, R. A. Schwartz, A. J. Conway, M. J. Aschwanden, A. Csillaghy, B. R. Dennis, C. Johns-Krull, S. Krucker, R. P. Lin, J. McTiernan, T. R. Metcalf, J. Sato, and D. M. Smith, "The RHESSI Imaging Concept," *Sol. Phys.*, vol. 210, pp. 61–86, 2002.

[37] G. J. Hurford, R. A. Schwartz, S. Krucker, R. P. Lin, D. M. Smith, and N. Vilmer, "First Gamma-Ray Images of a Solar Flare," *ApJ*, vol. 595, pp. L77–L80, Oct. 2003.

[38] G. J. Hurford, S. Krucker, R. P. Lin, R. A. Schwartz, G. H. Share, and D. M. Smith, "Gamma-Ray Imaging of the 2003 October/November Solar Flares," *ApJ*, vol. 644, pp. L93–L96, Jun. 2006.

[39] S. Ishikawa, H. Aono, S. Watanabe, S. Takeda, K. Nakazawa, and T. Takahashi, "Performance measurements of Al/CdTe/Pt pixel diode detectors," in *Hard X-Ray and Gamma-Ray Detector Physics IX*, ser. Proc. SPIE, R. B. James, A. Burger, and L. A. Franks, Eds., vol. 6706, 2007, p. 67060M.

[40] S. Ishikawa, S. Watanabe, T. Fukuyama, G. Sato, M. Kokubun, H. Odaka, S. Saito, T. Takahashi, K. Nakazawa, and T. Tanaka, "Development of Double-Sided CdTe Strip Detectors for γ-Ray Imaging and Spectroscopy," *Japanese Journal of Applied Physics*, vol. 49, no. 11, p. 116702, 2010.

[41] S. Ishikawa, S. Krucker, T. Takahashi, and R. P. Lin, "RHESSI Imaging Survey of γ-ray Bremsstrahlung Emission in Solar Flares," *ApJ*, vol. 728, p. 22, 2011.

[42] S. Ishikawa, S. Saito, H. Tajima, T. Tanaka, S. Watanabe, H. Odaka, T. Fukuyama, M. Kokubun, T. Takahashi, Y. Terada, S. Krucker, S. Christe, S. McBride, and L. Glesener, "Fine-pitch semiconductor detector for the foxsi

mission," *Nuclear Science, IEEE Transactions on*, vol. 58, no. 4, pp. 2039 –2046, 2011.

[43] S. Ishikawa, S. Krucker, T. Takahashi, and R. P. Lin, "On the Relation of Above-the-loop and Footpoint Hard X-Ray Sources in Solar Flares," *ApJ*, vol. 737, p. 48, 2011.

[44] S. R. Kane, "Impulsive /flash/ phase of solar flares - Hard X-ray, microwave, EUV and optical observations," in *Coronal Disturbances*, ser. IAU Symposium, G. A. Newkirk, Ed., vol. 57, 1974, pp. 105–141.

[45] H. W. Koch and J. W. Motz, "Bremsstrahlung Cross-Section Formulas and Related Data," *Reviews of Modern Physics*, vol. 31, pp. 920–955, 1959.

[46] J. E. Koglin, H. An, K. L. Blaedel, N. F. Brejnholt, F. E. Christensen, W. W. Craig, T. A. Decker, C. J. Hailey, L. C. Hale, F. A. Harrison, C. P. Jensen, K. K. Madsen, K. Mori, M. J. Pivovaroff, G. Tajiri, and W. W. Zhang, "NuSTAR hard x-ray optics design and performance," in *Optics for EUV, X-Ray, and Gamma-Ray Astronomy IV*, ser. Proc. SPIE, S. L. O'Dell and G. Pareschi, Eds., vol. 7437, 2009, p. 74370C.

[47] M. Kokubun, K. Nakazawa, T. Enoto, Y. Fukazawa, K. Gilmore, J. Kataoka, M. Kawaharada, P. Laurent, F. Lebrun, O. Limousin, K. Makishima, T. Mizuno, K. Mori, T. Nakamori, M. Ohno, M. Ohta, G. Sato, H. Tajima, H. Takahashi, T. Takahashi, T. Tanaka, Y. Terada, H. Uchiyama, Y. Uchiyama, S. Watanabe, Y. Yatsu, , and K. Yamaoka, "Hard X-ray Imager (HXI) for the ASTRO-H Mission," in *Space Telescopes and Instrumentation 2010: Ultraviolet to Gamma Ray*, ser. Proc. SPIE, M. Arnaud, S. S. Murray, and T. Takahashi, Eds., vol. 7732, 2010, p. 773215.

[48] R. A. Kopp and G. W. Pneuman, "Magnetic reconnection in the corona and the loop prominence phenomenon," *Sol. Phys.*, vol. 50, pp. 85–98, 1976.

[49] T. Kosugi, S. Masuda, K. Makishima, M. Inda, T. Murakami, T. Dotani,

Y. Ogawara, T. Sakao, K. Kai, and H. Nakajima, "The hard X-ray telescope (HXT) for the Solar-A mission," *Sol. Phys.*, vol. 136, pp. 17–36, 1991.

[50] T. Kosugi, T. Sakao, S. Masuda, K. Makishima, M. Inda, T. Murakami, Y. Ogawara, K. Yaji, and K. Matsushita, "The Hard X-ray Telescope (HXT) onboard YOHKOH - Its performance and some initial results," *PASJ*, vol. 44, pp. L45–L49, 1992.

[51] T. Kosugi, K. Matsuzaki, T. Sakao, T. Shimizu, Y. Sone, S. Tachikawa, T. Hashimoto, K. Minesugi, A. Ohnishi, T. Yamada, S. Tsuneta, H. Hara, K. Ichimoto, Y. Suematsu, M. Shimojo, T. Watanabe, S. Shimada, J. M. Davis, L. D. Hill, J. K. Owens, A. M. Title, J. L. Culhane, L. K. Harra, G. A. Doschek, and L. Golub, "The Hinode (Solar-B) Mission: An Overview," *Sol. Phys.*, vol. 243, pp. 3–17, 2007.

[52] J. Kotoku, K. Makishima, Y. Matsumoto, M. Kohama, Y. Terada, and T. Tamagawa, "Effects of Compton Scattering on the Gamma-Ray Spectra of Solar Flares," *PASJ*, vol. 59, pp. 1161–, 2007.

[53] K. Koyama, K. Hamaguchi, S. Ueno, N. Kobayashi, and E. D. Feigelson, "Discovery of Hard X-Rays from a Cluster of Protostars," *PASJ*, vol. 48, pp. L87–L92, 1996.

[54] G. F. Krymskii, "A regular mechanism for the acceleration of charged particles on the front of a shock wave," *Akademiia Nauk SSSR Doklady*, vol. 234, pp. 1306–1308, 1977.

[55] S. Krucker, A. O. Benz, T. S. Bastian, and L. W. Acton, "X-Ray Network Flares of the Quiet Sun," *ApJ*, vol. 488, pp. 499–505, 1997.

[56] S. Krucker and A. O. Benz, "X-Ray Network Flares of the Quiet Sun," *ApJ*, vol. 501, pp. L213–L216, 1998.

[57] S. Krucker and R. P. Lin, "Relative Timing and Spectra of Solar Flare Hard X-ray Sources," *Sol. Phys.*, vol. 210, pp. 229–243, 2002.

[58] S. Krucker, G. J. Hurford, and R. P. Lin, "Hard X-Ray Source Motions in the 2002 July 23 Gamma-Ray Flare," *ApJ*, vol. 595, pp. L103–L106, 2003.

[59] S. Krucker and R. P. Lin, "Hard X-Ray Emissions from Partially Occulted Solar Flares," *ApJ*, vol. 673, pp. 1181–1187, 2008.

[60] S. Krucker, G. J. Hurford, A. L. MacKinnon, A. Y. Shih, and R. P. Lin, "Coronal γ-Ray Bremsstrahlung from Solar Flare-accelerated Electrons," *ApJ*, vol. 678, pp. L63–L66, May 2008.

[61] S. Krucker, M. Battaglia, P. J. Cargill, L. Fletcher, H. S. Hudson, A. L. MacKinnon, S. Masuda, L. Sui, M. Tomczak, A. L. Veronig, L. Vlahos, and S. M. White, "Hard X-ray emission from the solar corona," *A&A Rev.*, vol. 16, pp. 155–208, 2008.

[62] S. Krucker, S. Christe, L. Glesener, S. McBride, P. Turin, D. Glaser, P. Saint-Hilaire, G. Delory, R. P. Lin, M. Gubarev, B. Ramsey, Y. Terada, S. Ishikawa, M. Kokubun, S. Saito, T. Takahashi, S. Watanabe, K. Nakazawa, H. Tajima, S. Masuda, T. Minoshima, and M. Shimojo, "The Focusing Optics X-ray Solar Imager (FOXSI)," in *Optics for EUV, X-Ray, and Gamma-Ray Astronomy IV*, ser. Proc. SPIE, S. L. O'Dell and G. Pareschi, Eds., vol. 7437, 2009, p. 743705.

[63] S. Krucker, H. S. Hudson, L. Glesener, S. M. White, S. Masuda, J.-P. Wuelser, and R. P. Lin, "Measurements of the Coronal Acceleration Region of a Solar Flare," *ApJ*, vol. 714, pp. 1108–1119, 2010.

[64] S. Krucker, S. Christe, L. Glesener, S. Ishikawa, S. McBride, D. Glaser, P. Turin, R. P. Lin, M. Gubarev, B. Ramsey, S. Saito, Y. Tanaka, T. Takahashi, S. Watanabe, T. Tanaka, H. Tajima, and S. Masuda, "The Focusing Optics X-ray Solar Imager (FOXSI)," in *Optics for EUV, X-Ray, and Gamma-Ray Astronomy IV*, ser. Proc. SPIE, S. L. O'Dell and G. Pareschi, Eds., vol. 8147, 2011, p. 814705.

[65] H. Kunieda, H. Awaki, A. Furuzawa, Y. Haba, R. Iizuka, K. Ishibashi, M. Ishida, M. Itoh, T. Kosaka, Y. Maeda, H. Matsumoto, T. Miyazawa, H. Mori,

Y. Namba, Y. Ogasaka, K. Ogi, T. Okajima, Y. Suzuki, K. Tamura, Y. Tawara, K. Uesugi, K. Yamashita, and S. Yamauchi, "Hard X-ray Telescope to be onboard ASTRO-H," in *Space Telescopes and Instrumentation 2010: Ultraviolet to Gamma Ray*, ser. Proc. SPIE, M. Arnaud, S. S. Murray, and T. Takahashi, Eds., vol. 7732, 2010, p. 773214.

[66] J. Leach and V. Petrosian, "Impulsive phase of solar flares. I - Characteristics of high energy electrons," *ApJ*, vol. 251, pp. 781–791, 1981.

[67] O. Limousin, "New trends in CdTe and CdZnTe detectors for X- and gamma-ray applications," *Nucl. Inst. Meth.*, vol. A 504, pp. 24–37, 2003.

[68] R. P. Lin, "Non-relativistic Solar Electrons," *Space Sci. Rev.*, vol. 16, pp. 189–256, Jun. 1974.

[69] R. P. Lin, B. R. Dennis, G. J. Hurford, D. M. Smith, A. Zehnder, P. R. Harvey, D. W. Curtis, D. Pankow, P. Turin, M. Bester, A. Csillaghy, M. Lewis, N. Madden, H. F. van Beek, M. Appleby, T. Raudorf, J. McTiernan, R. Ramaty, E. Schmahl, R. Schwartz, S. Krucker, R. Abiad, T. Quinn, P. Berg, M. Hashii, R. Sterling, R. Jackson, R. Pratt, R. D. Campbell, D. Malone, D. Landis, C. P. Barrington-Leigh, S. Slassi-Sennou, C. Cork, D. Clark, D. Amato, L. Orwig, R. Boyle, I. S. Banks, K. Shirey, A. K. Tolbert, D. Zarro, F. Snow, K. Thomsen, R. Henneck, A. McHedlishvili, P. Ming, M. Fivian, J. Jordan, R. Wanner, J. Crubb, J. Preble, M. Matranga, A. Benz, H. Hudson, R. C. Canfield, G. D. Holman, C. Crannell, T. Kosugi, A. G. Emslie, N. Vilmer, J. C. Brown, C. Johns-Krull, M. Aschwanden, T. Metcalf, and A. Conway, "The Reuven Ramaty High-Energy Solar Spectroscopic Imager (RHESSI)," *Sol. Phys.*, vol. 210, pp. 3–32, 2002.

[70] J. C. Lund, J. M. Vanscyoc III, R. B. James, D. S. McGregor, and R. W. Olsen, "Large volume room temperature gamma-ray spectrometers from $Cd_xZn_{1-x}Te$," *Nucl. Instr. and Meth.*, vol. A 380, pp. 256–261, 1996.

[71] S. Masuda, T. Kosugi, H. Hara, S. Tsuneta, and Y. Ogawara, "A loop-top hard X-ray source in a compact solar flare as evidence for magnetic reconnection," *Nature*, vol. 371, pp. 495–497, 1994.

[72] S. Masuda, T. Kosugi, H. Hara, T. Sakao, K. Shibata, and S. Tsuneta, "Hard X-Ray Sources and the Primary Energy-Release Site in Solar Flares," *PASJ*, vol. 47, pp. 677–689, 1995.

[73] S. Masuda, J. Sato, T. Kosugi, and T. Sakao, "Spectral Characteristics of Above-the-Looptop Hard X-Ray Source," *Advances in Space Research*, vol. 26, pp. 493–496, 2000.

[74] C. Matsumoto, T. Takahashi, K. Takizawa, R. Ohno, T. Ozaki, and K. Mori, "Performance of a New Schottky CdTe Detector for Hard X-ray Spectroscopy," *IEEE Trans. Nucl. Sci.*, vol. 45, pp. 428–432, 1998.

[75] Y. Matsumoto, K. Makishima, J. Kotoku, M. Yoshimori, K. Suga, T. Kosugi, S. Masuda, and K. Morimoto, "A Statistical Study of Gamma-Ray Emitting Solar Flares Observed with Yohkoh," *PASJ*, vol. 57, pp. 211–220, 2005.

[76] D. L. McKenzie, D. W. Datlowe, and L. E. Peterson, "Spectral Development of a Solar X-Ray Burst Observed on OSO-7," *Sol. Phys.*, vol. 28, pp. 175–185, 1973.

[77] D. E. McKenzie and H. S. Hudson, "X-Ray Observations of Motions and Structure above a Solar Flare Arcade," *ApJ*, vol. 519, pp. L93–L96, 1999.

[78] T. R. Metcalf and D. Alexander, "Coronal Trapping of Energetic Flare Particles:Yohkoh/HXT Observations," *ApJ*, vol. 522, pp. 1108–1116, 1999.

[79] A. Meuris, O. Limousin, F. Lugiez, O. Gevin, F. Pinsard, I. L. Mer, E. Delagnes, M. C. Vassal, F. Soufflet, and R. Bocage, "Caliste 64, an Innovative CdTe Hard X-Ray Micro-Camera," *IEEE Trans. Nucl. Sci.*, vol. 55, pp. 778–784, 2008.

[80] J. A. Miller, "Stochastic Particle Acceleration in Solar Flares," in *High Energy Solar Physics Workshop - Anticipating Hess!*, ser. Astronomical Society of the

Pacific Conference Series, R. Ramaty & N. Mandzhavidze, Ed., vol. 206, 2000, pp. 145–+.

[81] N. Mitani, "Hard x-ray imaging and spectroscopic analysis of solar flares by the *RHESSI* satellite (*in Japanese*)," Master's thesis, the University of Tokyo, Tokyo, 2005.

[82] H. Nakajima, M. Nishio, S. Enome, K. Shibasaki, T. Takano, Y. Hanaoka, C. Torii, H. Sekiguchi, T. Bushimata, S. Kawashima, N. Shinohara, Y. Irimajiri, H. Koshiishi, T. Kosugi, Y. Shiomi, M. Sawa, and K. Kai, "The Nobeyama radioheliograph." *IEEE Proceedings*, vol. 82, pp. 705–713, 1994.

[83] K. Nakazawa, K. Oonuki, T. Tanaka, Y. Kobayashi, K. Tamura, T. Mitani, G. Sato, S. Watanabe, T. Takahashi, R. Ohno, A. Kitajima, Y. Kuroda, and M. Onishi, "Improvement of the CdTe Diode Detectors using a Guard-ring Electrode," *IEEE Trans. Nucl. Sci.*, vol. 51, pp. 1881–1885, 2004.

[84] W. M. Neupert, "Comparison of Solar X-Ray Line Emission with Microwave Emission during Flares," *ApJ*, vol. 153, pp. L59+, 1968.

[85] M. Ohyama and K. Shibata, "Preflare Heating and Mass Motion in a Solar Flare Associated with Hot Plasma Ejection: 1993 November 11 C9.7 Flare," *PASJ*, vol. 49, pp. 249–261, 1997.

[86] R. A. Osten, S. Drake, J. Tueller, J. Cummings, M. Perri, A. Moretti, and S. Covino, "Nonthermal Hard X-Ray Emission and Iron Kα Emission from a Superflare on II Pegasi," *ApJ*, vol. 654, pp. 1052–1067, 2007.

[87] E. N. Parker, "The Solar-Flare Phenomenon and the Theory of Reconnection and Annihiliation of Magnetic Fields." *ApJS*, vol. 8, pp. 177–+, 1963.

[88] ——, "Nanoflares and the solar X-ray corona," *ApJ*, vol. 330, pp. 474–479, 1988.

[89] H. E. Petschek, "Magnetic Field Annihilation," *NASA Special Publication*, vol. 50, pp. 425–+, 1964.

[90] B. D. Ramsey, C. D. A. J. A. Apple, C. M. Benson, K. L. Dietz, R. F. Elsner, D. E. Engelhaupt, K. K. Ghosh, J. J. Kolodziejczak, S. L. O'Dell, C. O. Speegle, D. A. Swartz, and M. C. Weisskopf, "First Images from HERO, a Hard X-Ray Focusing Telescope," *ApJ*, vol. 568, pp. 432–435, 2002.

[91] P. Saint-Hilaire, S. Krucker, and R. P. Lin, "A Statistical Survey of Hard X-ray Spectral Characteristics of Solar Flares with Two Footpoints," *Sol. Phys.*, vol. 250, pp. 53–73, Jul. 2008.

[92] T. Sakao, T. Kosugi, S. Masuda, K. Yaji, M. Inda-Koide, and K. Makishima, "Characteristics of hard X-ray double sources in impulsive solar flares," *Advances in Space Research*, vol. 17, pp. 67–, 1996.

[93] J. Sato, T. Kosugi, and K. Makishima, "Improvement of YOHKOH Hard X-Ray Imaging," *PASJ*, vol. 51, pp. 127–150, 1999.

[94] P. H. Scherrer, R. S. Bogart, R. I. Bush, J. T. Hoeksema, A. G. Kosovichev, J. Schou, W. Rosenberg, L. Springer, T. D. Tarbell, A. Title, C. J. Wolfson, I. Zayer, and MDI Engineering Team, "The Solar Oscillations Investigation - Michelson Doppler Imager," *Sol. Phys.*, vol. 162, pp. 129–188, Dec. 1995.

[95] P. J. Sellin, P. J. Woods, D. Branford, T. Davinson, N. J. Davis, D. G. Ireland, K. Livingston, R. D. Page, A. C. Shotter, S. Hofmann, R. A. Hunt, A. N. James, M. A. C. Hotchkis, M. A. Freer, and S. L. Thomas, "A double-sided silicon strip detector system for proton radioactivity studies," *Nucl. Inst. Meth.*, vol. A 311, pp. 217–223, 1992.

[96] K. Shibata and S. Tanuma, "Plasmoid-induced-reconnection and fractal reconnection," *Earth, Planets, and Space*, vol. 53, pp. 473–482, 2001.

[97] A. Y. Shih, R. P. Lin, and D. M. Smith, "RHESSI Observations of the Proportional Acceleration of Relativistic >0.3 MeV Electrons and >30 MeV Protons in Solar Flares," *ApJ*, vol. 698, pp. L152–L157, Jun. 2009.

[98] T. Shimizu, "Energetics and Occurrence Rate of Active-Region Transient Brightenings and Implications for the Heating of the Active-Region Corona," *PASJ*, vol. 47, pp. 251–263, 1995.

[99] D. Shiota, H. Isobe, P. F. Chen, T. T. Yamamoto, T. Sakajiri, and K. Shibata, "Self-Consistent Magnetohydrodynamic Modeling of a Coronal Mass Ejection, Coronal Dimming, and a Giant Cusp-shaped Arcade Formation," *ApJ*, vol. 634, pp. 663–678, 2005.

[100] H. Shiraki, M. Funaki, Y. Ando, S. Kominami, K. Amemiya, and R. Ohno, "Improvement of the productivity in the growth of CdTe single crystal by THM for the new PET system," in *Nuclear Science Symposium Conference Record*, vol. 3, 2007, pp. 1783–1787.

[101] K. P. Singh, "Techniques in X-ray astronomy 2. Imaging detectors," *Resonance*, vol. 10, pp. 15–23, 2005.

[102] D. M. Smith, R. P. Lin, P. Turin, D. W. Curtis, J. H. Primbsch, R. D. Campbell, R. Abiad, P. Schroeder, C. P. Cork, E. L. Hull, D. A. Landis, N. W. Madden, D. Malone, R. H. Pehl, T. Raudorf, P. Sangsingkeow, R. Boyle, I. S. Banks, K. Shirey, and R. Schwartz, "The RHESSI Spectrometer," *Sol. Phys.*, vol. 210, pp. 33–60, 2002.

[103] A. Stefanescu, G. Kanbach, A. Słowikowska, J. Greiner, S. McBreen, and G. Sala, "Very fast optical flaring from a possible new Galactic magnetar," *Nature*, vol. 455, pp. 503–505, 2008.

[104] P. A. Sturrock, "Model of the High-Energy Phase of Solar Flares," *Nature*, vol. 211, pp. 695–697, 1966.

[105] P. A. Sweet, "The Neutral Point Theory of Solar Flares," in *Electromagnetic Phenomena in Cosmical Physics*, ser. IAU Symposium, B. Lehnert, Ed., vol. 6, 1958, pp. 123–+.

[106] H. Tajima, T. Kamae, S. Uno, T. Nakamoto, Y. Fukazawa, T. Mitani, T. Takahashi, K. Nakazawa, Y. Okada, and M. Nomachi, "Low Noise Double-Sided Silicon Strip Detector for Multiple-Compton Gamma-ray Telescope," in *X-Ray and Gamma-Ray Telescopes and Instruments for Astronomy*, ser. Proc. SPIE, J. E. Truemper and H. D. Tananbaum, Eds., vol. 4851, 2003, pp. 875–884.

[107] H. Tajima, G. Madejski, T. Mitani, T. Tanaka, H. Nakamura, K. Nakazawa, T. Takahashi, Y. Fukazawa, T. Kamae, M. Kokubun, D. Marlow, M. Nomachi, and E. do Couto e Silva, "Gamma-ray polarimetry with Compton Telescope," in *UV and Gamma-Ray Space Telescope Systems*, ser. Proc. SPIE, G. Hasinger and M. J. L. Turner, Eds., vol. 5488, 2004, pp. 561–571.

[108] T. Takahashi and S. Watanabe, "Recent progress in CdTe and CdZnTe detectors," *IEEE Trans. Nucl. Sci.*, vol. 48, pp. 950–959, 2001.

[109] T. Takahashi, K. Mitsuda, R. Kelley, F. Aharonian, F. Akimotod, S. Allen, N. Anabuki, L. Angelini, K. Arnaud, H. Awaki, A. Bamba, N. Bando, M. Bautz, R. Blandford, K. Boyc, G. Brown, M. Chernyakova, P. Coppi, E. Costantini, J. Cottam, J. Crow, J. de Plaa, C. de Vries, J. den Herder, M. DiPirro, C. Done, T. Dotani, K. Ebisawa, T. Enoto, Y. Ezoe, A. Fabian, R. Fujimoto, Y. Fukazawa, S. Funk, A. Furuzawa, M. Galeazzi, P. Gandhi, K. Gendreau, K. Gilmore, Y. Haba, K. Hamaguchi, I. Hatsukade, K. Hayashida, J. Hiraga, K. Hirose, A. Hornschemeier, J. Hughes, U. Hwang, R. Iizuka, K. Ishibashi, M. Ishida, K. Ishimura, Y. Ishisaki, N. Isobe, M. Ito, N. Iwata, J. Kaastra, T. Kallman, T. Kamae, H. Katagiri, J. Kataoka, S. Katsuda, M. Kawaharada, N. Kawai, S. Kawasaki, D. Khangaluyan, C. Kilbourne, K. Kinugasa, S. Kitamoto, T. Kitayama, T. Kohmura, M. Kokubun, T. Kosaka, T. Kotani, K. Koyama, A. Kubota, H. Kunieda, P. Laurent, F. Lebrun, O. Limousin, M. Loewenstein, K. Long, G. Madejski, Y. Maeda, K. Makishima, M. Markevitch, H. Matsumoto, K. Matsushita, D. McCammon, J. Miller, S. Mineshige, K. Minesugi, T. Miyazawa, T. Mizuno, K. Mori, H. Mori, K. Mukai, H. Murakami, T. Murakami, R. Mushotzky, Y. Nakagawa, T. Nakagawa, H. Nakajima,

T. Nakamori, K. Nakazawa, Y. Namba, M. Nomachi, S. O. Dell, H. Ogawa, M. Ogawa, K. Ogi, T. Ohashi, M. Ohno, M. Ohta, T. Okajima, N. Ota, M. Ozaki, F. Paerels, S. Paltani, A. Parmer, R. Petre, M. Pohl, S. Porter, B. Ramsey, C. Reynolds, S. Sakai, R. Sambruna, G. Sato, Y. Sato, P. Serlemitsos, M. Shida, T. Shimada, K. Shinozaki, P. Shirron, R. Smith, G. Sneiderman, Y. Soong, L. Stawarz, H. Sugita, A. Szymkowiak, H. Tajima, H. Takahashi, Y. Takei, T. Tamagawa, T. Tamura, K. Tamura, T. Tanaka, Y. Tanaka, Y. Tanaka, M. Tashiro, Y. Tawara, Y. Terada, Y. Terashima, F. Tombesi, H. Tomida, M. Tozuka, Y. Tsuboi, M. Tsujimoto, H. Tsunemi, T. Tsuru, H. Uchida, Y. Uchiyama, H. Uchiyama, Y. Ueda, S. Uno, M. Urry, S. Watanabe, N. White, T. Yamada, H. Yamaguchi, K. Yamaoka, N. Yamasaki, M. Yamauchi, S. Yamauchi, Y. Yatsu, D. Yonetoku, and A. Yoshida, "The ASTRO-H Mission," in *Space Telescopes and Instrumentation 2010: Ultraviolet to Gamma Ray*, ser. Proc. SPIE, M. Arnaud, S. S. Murray, and T. Takahashi, Eds., vol. 7732, 2010, p. 77320Z.

[110] S. Takeda, S. Watanabe, T. Tanaka, K. Nakazawa, T. Takahashi, Y. Fukazawa, H. Yasuda, H. Tajima, Y. Kuroda, M. Onishi, and K. Genba, "Development of double-sided silicon strip detectors (DSSD) for a Compton telescope," *Nucl. Inst. Meth.*, vol. A 579, pp. 859–865, 2007.

[111] R. Turkmani and J. Brown, "Electrons re-acceleration at the footpoints of Solar Flares," *ArXiv e-prints*, 2010.

[112] H. Toyama, A. Nishihira, M. Yamazato, A. Higa, T. Maehara, R. Ohno, and M. Toguchi, "Formation of Alminuium Schottly Contact on Plasma-Treated Cadmium Telluride Surface," *J. J. Appl. Phys.*, vol. 43, pp. 6371–6375, 2004.

[113] H. Toyama, M. Yamazato, A. Higa, T. Maehara, R.Ohno, and M. Toguchi, "Effect of He Plasma Treatment on the Rectification Properties of Al/CdTe Schottky Contacts," *J. J. Appl. Phys.*, vol. 44, pp. 6742–6746, 2005.

[114] S. Tsuneta, T. Takahashi, L. W. Acton, M. E. Bruner, K. L. Harvey, and

Y. Ogawara, "Global restructuring of the coronal magnetic fields observed with the YOHKOH Soft X-ray Telescope," *PASJ*, vol. 44, pp. L211–L214, 1992.

[115] S. Tsuneta and T. Naito, "Fermi Acceleration at the Fast Shock in a Solar Flare and the Impulsive Loop-Top Hard X-Ray Source," *ApJ*, vol. 495, pp. L67+, 1998.

[116] M. Ugai and T. Tsuda, "Magnetic field-line reconnexion by localized enhancement of resistivity. I - Evolution in a compressible MHD fluid," *Journal of Plasma Physics*, vol. 17, pp. 337–356, 1977.

[117] A. M. Veronig, J. C. Brown, B. R. Dennis, R. A. Schwartz, L. Sui, and A. K. Tolbert, "Physics of the Neupert Effect: Estimates of the Effects of Source Energy, Mass Transport, and Geometry Using RHESSI and GOES Data," *ApJ*, vol. 621, pp. 482–497, 2005.

[118] N. Vilmer, S. R. Kane, and G. Trottet, "Impulsive and gradual hard X-ray sources in a solar flare," *A&A*, vol. 108, pp. 306–313, 1982.

[119] S. Watanabe, S. Ishikawa, S. Takeda, H. Odaka, T. Tanaka, T. Takahashi, K. Nakazawa, M. Yamazato, A. Higa, and S. Kaneku, "New CdTe Pixel Gamma-Ray Detector with Pixelated Al Schottky Anodes," *J. J. Appl. Phys.*, vol. 46, pp. 6043–6045, 2007.

[120] S. Watanabe, S. Tanekda, S. Ishikawa, H. Odaka, M. Ushio, T. Tanaka, K. Nakazawa, T. Takahashi, H. Tajima, Y. Fukazawa, Y. Kuroda, and M. Onishi, "Development of Semiconductor Imaging Detectors for a Si/CdTe Compton Camera," *Nucl. Inst. Meth.*, vol. A 579, pp. 871–877, 2007.

[121] S. Watanabe, S. Ishikawa, H. Aono, S. Takeda, H. Odaka, M. Kokubun, T. Takahashi, K. Nakazawa, H. Tajima, M. Onishi, and Y. Kuroda, "High Energy Resolution Hard X-Ray and Gamma-Ray Imagers Using CdTe Diode Devices," *IEEE Trans. Nucl. Sci.*, vol. 56, pp. 777–782, 2009.

[122] A. Warmuth, G. D. Holman, B. R. Dennis, G. Mann, H. Aurass, and R. O. Milligan, "Rapid Changes of Electron Acceleration Characteristics at the End of the Impulsive Phase of an X-class Solar Flare," *ApJ*, vol. 699, pp. 917–922, 2009.

[123] G. L. Withbroe and R. W. Noyes, "Mass and energy flow in the solar chromosphere and corona," *ARA&A*, vol. 15, pp. 363–387, 1977.

[124] Y. H. Yang, C. Z. Cheng, S. Krucker, R. P. Lin, and W. H. Ip, "A Statistical Study of Hard X-Ray Footpoint Motions in Large Solar Flares," *ApJ*, vol. 693, pp. 132–139, 2009.

[125] T. Yokoyama and K. Shibata, "A Two-dimensional Magnetohydrodynamic Simulation of Chromospheric Evaporation in a Solar Flare Based on a Magnetic Reconnection Model," *ApJ*, vol. 494, pp. L113–L116, 1998.

[126] T. Yokoyama, K. Akita, T. Morimoto, K. Inoue, and J. Newmark, "Clear Evidence of Reconnection Inflow of a Solar Flare," *ApJ*, vol. 546, pp. L69–L72, 2001.

Acknowledgements

I would like to appreciate my advisor, Prof. Tadayuki Takahashi, for his supervision and giving me a chance to work for attractive frontier semiconductor detectors and exciting observation missions.

I really thank Dr. Säm Krucker, Principal Investigator of the *FOXSI* mission and specialist of *RHESSI* HXR analysis of solar flares. I wrote most of the thesis through many discussions during my visit to Dr. Krucker at Space Science Laboratory, University of California, Berkeley. I believe this thesis could not be completed without the presence and kindness of Dr. Krucker. I also want to thank Dr. Steven Christe and Ms. Lindsay Glesener, co-Principal Investigators of *FOXSI*, for their comments, including great contribution in correcting English grammatically.

In groups of solar science in Japan, I thank Dr. Satoshi Masuda, Dr. Takeshi Minoshima, Dr. Masumi Shimojo and many other researchers in National Astronautical Observatory Japan and Institute of Astronautical Science, Japan Aerospace Exploration Agency, for their discussions and comments. On the research on detectors, I appreciate Prof. Hiroyasu Tajima, Dr. Shin Watanabe and members of Takahashi-group, including former members, involved in the development of detectors. My work on detectors is strongly based on their effort in the past days.

My research was supported by the Grant-in-Aid for JSPS fellows from the Japan Society for the Promotion of Science, and the Global Center of Excellence Program "the Physical Sciences Frontier", Ministry of Education, Culture, Sports, Science and Technology, Japan.